NAVAL POSTGRADUATE SCHOOL

MONTEREY, CALIFORNIA

THESIS

AN ANALYSIS OF THE BEAUFORT SEA THERMOHALINE STRUCTURE AND VARIABILITY, AND ITS EFFECTS ON ACOUSTIC PROPAGATION

by

Annalise N. Pearson

June 2016

Thesis Advisor:	John A. Colosi
Second Reader:	John E. Joseph

THIS PAGE INTENTIONALLY LEFT BLANK

REPORT DOCUMENTATION PAGE			*Form Approved OMB No. 0704–0188*

1. AGENCY USE ONLY *(Leave blank)*	**2. REPORT DATE** June 2016	**3. REPORT TYPE AND DATES COVERED** Master's thesis

4. TITLE AND SUBTITLE AN ANALYSIS OF THE BEAUFORT SEA THERMOHALINE STRUCTURE AND VARIABILITY, AND ITS EFFECTS ON ACOUSTIC PROPAGATION	**5. FUNDING NUMBERS**
6. AUTHOR(S) Annalise N. Pearson	
7. PERFORMING ORGANIZATION NAME(S) AND ADDRESS(ES) Naval Postgraduate School Monterey, CA 93943-5000	**8. PERFORMING ORGANIZATION REPORT NUMBER**
9. SPONSORING /MONITORING AGENCY NAME(S) AND ADDRESS(ES) N/A	**10. SPONSORING / MONITORING AGENCY REPORT NUMBER**

11. SUPPLEMENTARY NOTES The views expressed in this thesis are those of the author and do not reflect the official policy or position of the Department of Defense or the U.S. Government. IRB Protocol number ____N/A____.

12a. DISTRIBUTION / AVAILABILITY STATEMENT Approved for public release; distribution is unlimited	**12b. DISTRIBUTION CODE**

13. ABSTRACT (maximum 200 words)

This thesis provides an analysis of spatial and temporal thermohaline variations of the Canada Basin in the Western Arctic and examines how these variations affect sound speed fields and acoustic propagation. In recent decades, changes in the Arctic water column have been underway as a result of climate change including reduced sea ice and changes in transports between the Pacific and Atlantic oceans. These changes were studied and analyzed using observational data collected from the Canada Basin Acoustic Propagation Experiment (CANAPE) conducted in the summer of 2015.

The thermohaline sound speed structure was examined by computing isopycnal displacements, which allowed separation of internal waves and eddies from intrusive thermohaline structure or spice. Temporal structure of these processes was estimated using spectral analysis, and vertical structure was examined by computing the rms variation of the various processes as a function of depth. Observations were compared to climatology. Acoustic propagation simulations using a ray-based model termed Bellhop were used to estimate the acoustic sensitivity to the observed ocean structure. It was found that internal waves were weak compared to the Garret Munk spectrum and that spice is surprisingly strong in the ocean structure with dominance in the upper 100m.

The acoustic analysis revealed that a greater variability in transmission loss in the CTD CANAPE data was evident compared to climatology and previous observations, particularly at greater frequencies and range. The presence of a sub-surface sound speed duct existed with an axis at ~120m and accommodated an environment with increased travel distance for acoustic energy and lower transmission loss for depths between 100–200m.

14. SUBJECT TERMS polar oceanography, Beaufort Sea, thermohaline sound speed structure, climate change, Arctic sea ice extent, acoustic propagation, Arctic acoustics	**15. NUMBER OF PAGES** 121
	16. PRICE CODE

17. SECURITY CLASSIFICATION OF REPORT	**18. SECURITY CLASSIFICATION OF THIS PAGE**	**19. SECURITY CLASSIFICATION OF ABSTRACT**	**20. LIMITATION OF ABSTRACT**
Unclassified	Unclassified	Unclassified	UU

NSN 7540–01-280-5500

Standard Form 298 (Rev. 2–89)
Prescribed by ANSI Std. 239–18

THIS PAGE INTENTIONALLY LEFT BLANK

Approved for public release; distribution is unlimited

AN ANALYSIS OF THE BEAUFORT SEA THERMOHALINE STRUCTURE AND VARIABILITY, AND ITS EFFECTS ON ACOUSTIC PROPAGATION

Annalise N. Pearson
Lieutenant Commander, Royal Australian Navy
B.S., Australian Defence Force Academy

Submitted in partial fulfillment of the
requirements for the degree of

MASTER OF SCIENCE IN PHYSICAL OCEANOGRAPHY

from the

NAVAL POSTGRADUATE SCHOOL
June 2016

Approved by: John A. Colosi
Thesis Advisor

John E. Joseph
Second Reader

Peter Chu
Chair, Department of Oceanography

THIS PAGE INTENTIONALLY LEFT BLANK

ABSTRACT

This thesis provides an analysis of spatial and temporal thermohaline variations of the Canada Basin in the Western Arctic and examines how these variations affect sound speed fields and acoustic propagation. In recent decades, changes in the Arctic water column have been underway as a result of climate change including reduced sea ice and changes in transports between the Pacific and Atlantic oceans. These changes were studied and analyzed using observational data collected from the Canada Basin Acoustic Propagation Experiment (CANAPE) conducted in the summer of 2015.

The thermohaline sound speed structure was examined by computing isopycnal displacements, which allowed separation of internal waves and eddies from intrusive thermohaline structure or spice. Temporal structure of these processes was estimated using spectral analysis, and vertical structure was examined by computing the rms variation of the various processes as a function of depth. Observations were compared to climatology. Acoustic propagation simulations using a ray-based model termed Bellhop were used to estimate the acoustic sensitivity to the observed ocean structure. It was found that internal waves were weak compared to the Garret Munk spectrum and that spice is surprisingly strong in the ocean structure with dominance in the upper 100m.

The acoustic analysis revealed that a greater variability in transmission loss in the CTD CANAPE data was evident compared to climatology and previous observations, particularly at greater frequencies and range. The presence of a sub-surface sound speed duct existed with an axis at ~120m and accommodated an environment with increased travel distance for acoustic energy and lower transmission loss for depths between 100–200m.

THIS PAGE INTENTIONALLY LEFT BLANK

TABLE OF CONTENTS

LIST OF FIGURES

LIST OF TABLES

THIS PAGE INTENTIONALLY LEFT BLANK

LIST OF ACRONYMS AND ABBREVIATIONS

ACIA	Arctic Climate Impacts Assessment
ACOUS	Arctic climate observation using underwater sound
ADCP	Acoustic Doppler Current Profiles
CANAPE	Canada Basin Acoustic Propagation Experiment
CCC	Committee on Climate Change
CMIP5	Coupled Model Intercomparison Project Phase 5 models
CTD	Conductivity, Temperature, Depth
DMSP	Defense Meteorological Satellite Program
DRA	Data Release Area
DVLA	Distributed Vertical Vine Array
GIS	Geospatial Information Systems
GMSLR	Global Mean Sea Level Rise
Hz	Hertz – equivalent to cycles per second
IBCAO	International Bathymetric Chart of the Arctic Ocean
ICEX	Ice Exercise
IPCC	Intergovernmental Panel on Climate Change
ITP	Ice Tethered Profile
IW	Internal Wave
kHz	Kilo-Hertz
ONR	Office of Naval Research
MIZ	Marginal Ice Zone
NECI	National Centers for Environmental Information
NESTA	National Earth Science Teachers Association
NOAA	National Oceanic and Atmospheric Administration
NODC	National Oceanographic Data Center
NSIDC	National Snow and Ice Data Center
PE	Parabolic Equation
PSD	Power Spectral Density
PSS	Practical Salinity Scale-1978
PSW	Pacific Summer Water

PWW	Pacific Winter Water
RCP	Representative Concentration Pathways
rWML	remnant of Winter Mixed Layer
SBE	Sea-Bird Electronics
SCICEX	Science Ice Exercise
SM	Serial interface, internal battery, non-volatile Memory (Sea-Bird SBE 37- SM MicroCAT)
SML	Surface Mixed Layer
SMP	Summary for Policymakers
SMP	Serial interface, internal battery, non-volatile Memory, and integral Pump (Sea-Bird SBE 37-SMP MicroCAT)
SSMIS	Special Sensor Microwave Imager and Sounder
SUBFOR	Submarine Force
TAP	Transarctic Acoustic Propagation experiment
UCAR	University Cooperation for Atmospheric Research
UIUC	University of Illinois at Urbana-Champaign
WHOI	Woods Hole Oceanographic Institution
WI	Wavenumber Integration
WKB	Wentzel-Kramers-Brillouin depth scaling relation
WOA	World Ocean Atlas
WOD	World Ocean Database

ACKNOWLEDGMENTS

This thesis would not have been possible without the encouragement, guidance, support and patience of my advisor, John Colosi. I also have great admiration for John Joseph, who was a valuable second reader and provided much advice while answering numerous questions every day. I am indebted to Lieutenant Commander Dominic DiMaggio; without his knowledge, guidance, unwavering help and friendship, I would not have pulled through with my sanity intact. I am very grateful to Chris Miller for helping with MATLAB code as well as IT support. Many times, he helped with areas that I was stuck on. I would like to thank Tetyana Margolina for being a wonderful office co-habitor. She graciously shared her office and provided kind words and help frequently. I would like to acknowledge Peter Worcester and Matthew Dzieciuch from Scripps Institute of Oceanography for sharing their data and work. I also would like to thank our Oceanography Program Officer Commander Paula Travis for providing guidance and time in her busy schedule to help with unblocking the dreaded writer's block. Michele D'Ambrosio in the Thesis Processing Office kept my thesis consistent and my format squared-away. I wish to thank the professors and staff at the NPS Departments of Oceanography and Meteorology for their tireless commitment to imparting knowledge and expertise on the students who pass through NPS. Last but not least, I thank my work colleagues and friends. Without their friendship and support, I do not think I would have finished.

THIS PAGE INTENTIONALLY LEFT BLANK

I. INTRODUCTION

A. THE CHANGING ARCTIC AND THE RAMIFICATIONS FOR OCEAN ACOUSTICS

Polar regions are home to large areas of ocean covered by ice, making them significantly different from the rest of the world. Ice cover has an acoustic importance; it acts as a boundary and can change the properties of the water column. Of most importance are the effects of ice on the exposure to the atmosphere and the change in underlying water masses from the Pacific and Atlantic oceans. This surface boundary shields the ocean from the effects of wind, reducing sea state, turbulence, and mixing. Calmer waters can result in less scattering, causing sound transmissions to be more stable and possibly travel further distances due to the nature of the water column. The Arctic water column near the first few layers is predominately fresh cold over warm salty water, resulting in an upward refracting environment.

Additionally, the canopy of the sea ice is not strictly flat and its variability in roughness and thickness can affect the absorption values of sound energy that interact with the surface. Therefore, depending on the surface properties, sound energy will experience variable attenuation, and scattering. This boundary further acts to insulate the ocean from solar radiation forcing due to the albedo contrast from ice to snow. This is of concern due to the fact that if solar radiation absorption increases in the surface layer with decreasing albedo, it results in changes in the fresher colder water due to more ice melting. Hence, this affects the thermohaline structure, which in turn impacts acoustic propagation because of the inherent nature of sound in the ocean.

B. OCEANOGRAPHY: CANADA BASIN AND THE ARCTIC OCEAN

This report investigates the recent changes due to warming in the acoustic properties of the Canada Basin. This sub-section will address the oceanography of the area as well as water column properties.

The Canada Basin is of significant importance to the Arctic and global climate change. It is the largest of four sub-basins in the Arctic with the greatest loss of first-year

and multi-year ice than the other three sub-basins (McLaughlin et al. 2011). A possible explanation is the reducing of sea ice thickness in north Alaska by the heat entering from the Pacific. This thinner ice is driven by the Beaufort Gyre, facilitating the transport of warmer Pacific water to deeper waters off of the Alaskan shelf. This transport contributes to the positive ice-albedo feedback loop by reducing the ice cover offshore and exposing the darker ocean, which has a higher capacity for solar radiating absorption (Walsh et al. 2013). In relation to the comparable sea ice loss in the Canada Basin to the other three sub-basins, the environmental changes are significant, which provides a suitable basis for a study into the variability of the Arctic Ocean water column.

The Canada Basin (Figure 1) is a sub-basin of the Amerasian basin and lies north of Northern America and extends 700 miles from the Beaufort Shelf to the Alpha Cordillera. The Alpha Cordillera (Ridge) separates the Canada basin and the Makarov basin. The other two sub-basins, Nansen Basin and the Amundsen Basin form The Eurasian Basin, and are separated by Gakkel Ridge. The Eurasian Basin and the Amerasian basin are divided by the Lomonosov Ridge. (*Encyclopedia Britannica* 2016, McLaughlin et al. 2013, Geoglogy.com 2016)

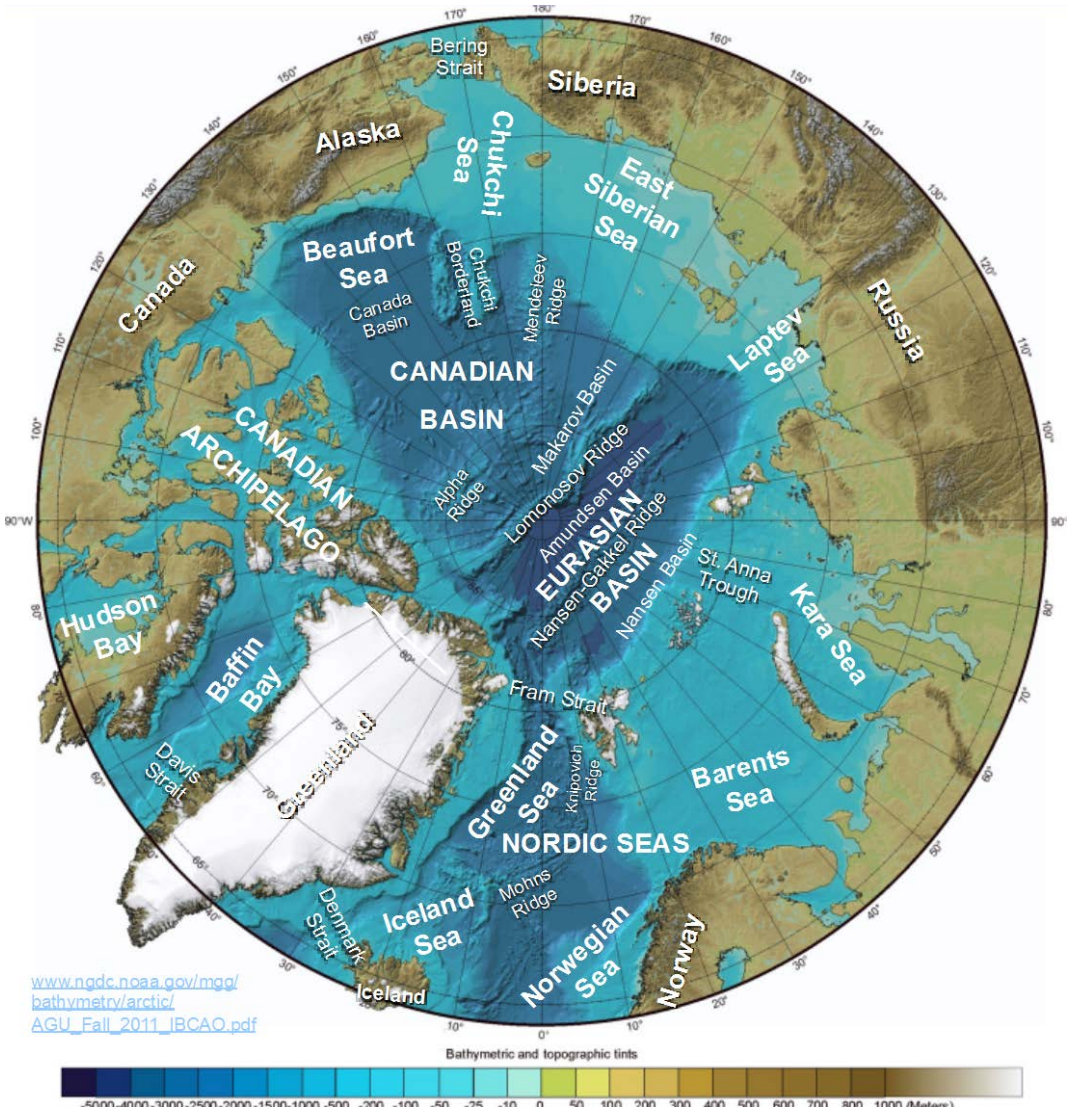

International Bathymetric Chart of the Arctic Ocean annotated with the names of seafloor features

Figure 1. Arctic Ocean Seafloor Features Map. Adapted from IBCAO (2012).

Other characteristics that establish the Canada Basin as a unique basin are the circulation and halocline. The Beaufort High drives the circulation clockwise, and the halocline is strongly stratified with higher nutrient levels than the other three sub-basins (McLaughlin 2013).

In high latitudes, the halocline is defined as a vertical salinity gradient where fresh water from either river runoff or melting sea ice lies over more saline waters. The recent

water mass structure of the Canada Basin (Figure 2) is composed of the Surface Mixed Layer (SML), the remnant of Winter Mixed Layer (rWML), the Pacific Summer Water (PSW), the Pacific Winter Water (PWW), the Atlantic water layer, the Summer Halocline, the Winter Halocline, and Lower Halocline (Jackson et al. 2010). During the summer in recent observations, the SML lies from ~10-20m and is highly stratified (S~26.5) from freshwater input due to sea ice melt, precipitation and evaporation, and river run off chiefly from the largest northward flowing river in the region, the Mackenzie River (McLaughlin 2013). A near surface temperature maximum (NSTM) is present at ~25-35m, due to solar radiation penetrating through thin sea ice (Jackson et al. 2010). The NSTM lies within the summer halocline, a halocline feature formed in summer, which separates the SML to the NSTM once enough sea ice melt has accumulated (Jackson et al., 2013). Below the NSTM there are remnants of the previous winter mixed layer. Here the base is where the winter halocline is found. The next layers originate from the Pacific Ocean through the shallow Bering Strait (~50m), transporting summer Bering Sea Water and Alaskan Coastal Water. In summer the Pacific water is warmed and homogenized over the Chukchi Shelf, resulting in the PSW, and creates a temperature maximum at 50–100m (Talley et al. 2011) with a salinity of $28<S<32$ psu (McLaughlin 2013). The PWW, originated similar to the PSW, but formed by ice formation over the Chukchi Shelf during the winter (Pisareva et al. 2015), and creates a temperature minimum further below at a depth near 150m (Talley et al. 2011) with a salinity of $32<S<33.5$ (McLaughlin 2013). Below this, temperature increases with depth reaching a maximum around 400m defining the lower limit of the Atlantic water, with the top delineating the lower halocline. This warm saline Atlantic water enters the Canada Basin through the Fram Strait and sinks due to it being denser in nature. Below this layer, bottom water exits, this being Canadian Basin Deep Water.

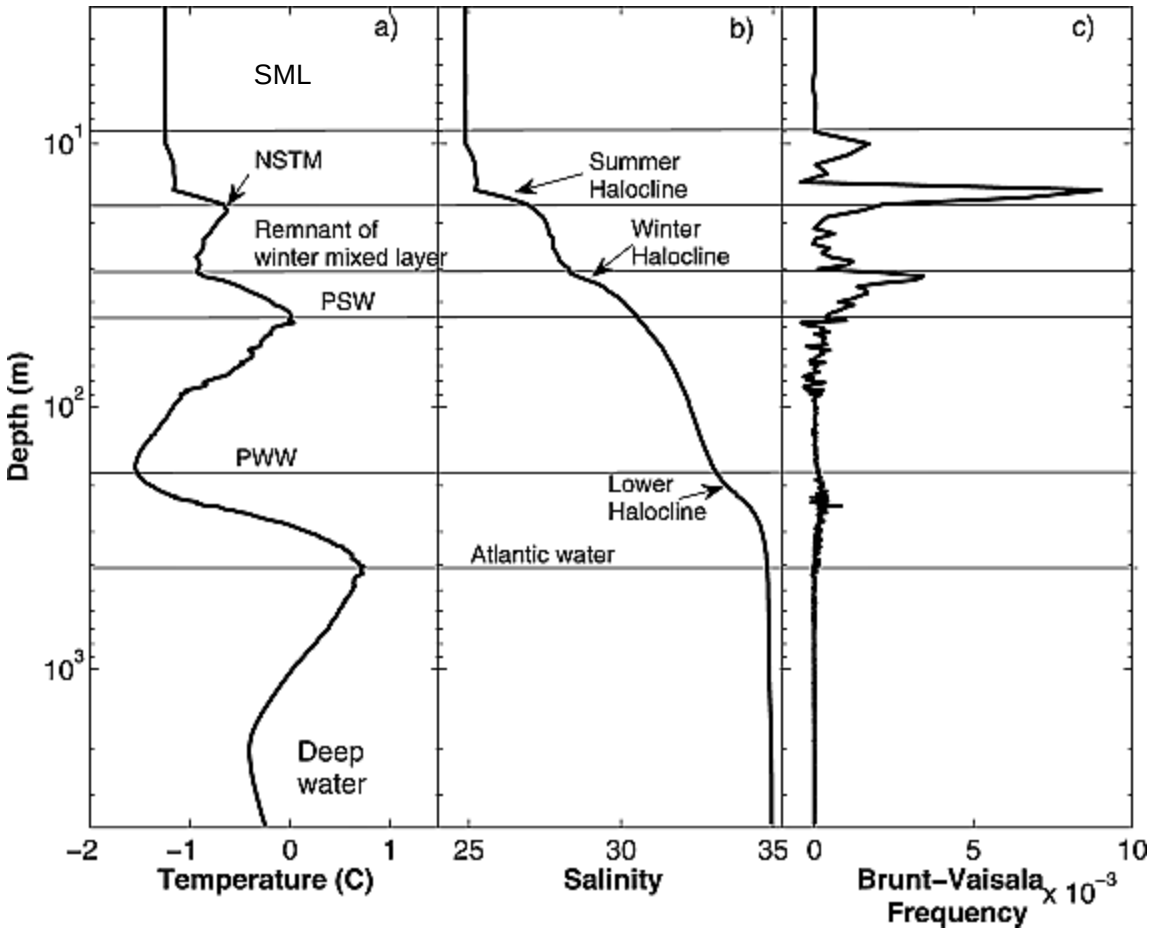

Note the depth axis is log scale. Profiles are from a station located at 75°N, 150°W, occupied on 29 August 2006

Figure 2. Water Mass Structure of the Canada Basin as Characterized by (a) Temperature, (b) Salinity, and (c) Brunt-Vaisala Frequency Profiles. Source: Jackson et al. (2010).

The temperature minimum associated with the PWW is a very interesting feature in terms of acoustic propagation. In the Marginal Ice Zone (MIZ) study conducted by ONR in 2014, navigational signals with a center frequency of 900Hz were transmitted with ranges greatly exceeding expectations, often in excess of 300km (Worcester et al. 2015). A conceivable explanation is that the signals were trapped in the duct and did not suffer losses associated with scattering form the ice.

Another significant feature present in the Artic due to its unique environment is a double-diffusion staircase near the thermohaline due to the presence of cold, fresh water over the warm, salty water in the Atlantic Layer. In the central Canada Basin at about 200–300m the double-diffusive staircase can be found, however it is absent at the basin periphery (Timmermans et al. 2008). It is suggested by Worcester et al. (2015) that due to higher internal wave energy these double-diffusive structures could advect up and down, affecting acoustic propagation.

It is important to understand the water masses in the Arctic with respect to acoustic propagation; however, a further contributor to the unique acoustic behavior in polar regions is sea ice. “The propagation of underwater acoustic signals in polar regions is dominated by an upward refracting sound speed environment” (Alexander et al. 2013) and the highly variable ice canopy. The age of sea ice impacts greatly on the characteristics of the ice canopy, specifically ice thickness and roughness. First year ice has a smoother thinner under-ice profile, whereas multi-year ice is thicker and more rugged (Wadhams et al. 2012). Ridging also affects the thickness of ice. This is a mechanical method formed by the shearing and compression of ice floes (Alexander et al. 2013). Ridging occurs more often in multi-year ice due to its age than first year ice, with the keel being split into a number of independent solid, smooth blocks of large size, subjecting multi-year ice to an irregular ridge profile (Alexander et al. 2013). Multi-year ice now comprises only 30% of the ice in the Arctic Ocean (NSDIC 2015) (Figure 3), resulting in dominance of first-year ice, hence reducing pressure ridging. As a result, the ice keels are decreasing in size, concluding in a reduction in transmission loss. Moreover, Worcester et al., 2014 suggests that due to the reducing ice thickness in the Arctic, signals with frequencies above the range of very low frequency (<20Hz) can now be employed for long-range propagation, including in the deployment of ocean tomography.

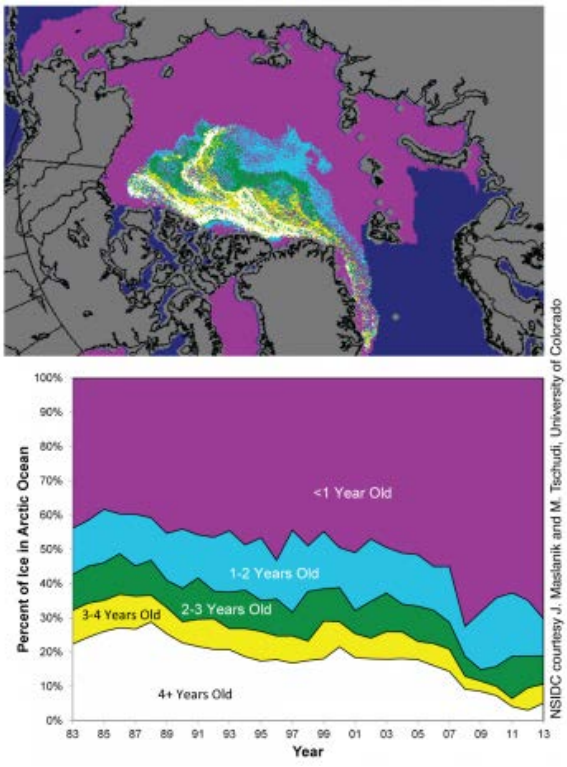

The map at top shows the ages of ice in the Arctic at the end of March 2013; the bottom graph shows how the percentage of ice in each age group has changed from 1983 to 2013.

Figure 3. Arctic Sea Ice Age at the End of March 2013.
Source: NSIDC (2015).

Previous experiments in acoustic propagation in the Arctic including the Transarctic Acoustic Propagation (TAP) experiment (Mikhalevsky et al., 1999), and the Arctic climate observation using underwater sound (ACOUS) experiment (Gavrilov et al. 2006) demonstrated, using low-frequency acoustic transmission, that basin-scale warming is present in the Atlantic layer of the Arctic Ocean (Mikhalevsky et al., 1999) and (Gavrilov et al. 2006).

Another noteworthy feature of the Arctic is the Arctic acoustic channel, which is a half sound channel located at the surface due to the upper refracting characteristics of the Arctic Ocean. As the ice cover is thinning, but still reducing wind turbulence and disturbance, the Arctic acoustic channel should be preserved (Worcester et al. 2014).

C. CURRENT STATE OF SEA ICE IN THE ARCTIC

As previously mentioned, ice is an important component affecting acoustic propagation both from its rough surface and from its shielding effect in air/sea interaction. We therefore review some relevant studies. Recent studies, such as that conducted by National Snow and Ice Data Center (NSIDC) (Figure 4), have shown the sea ice in the Arctic Ocean is declining by 13.4% per decade (NSIDC 2015), with NSIDC claiming that the nine lowest September ice extents have occurred in the last nine years of satellite records.

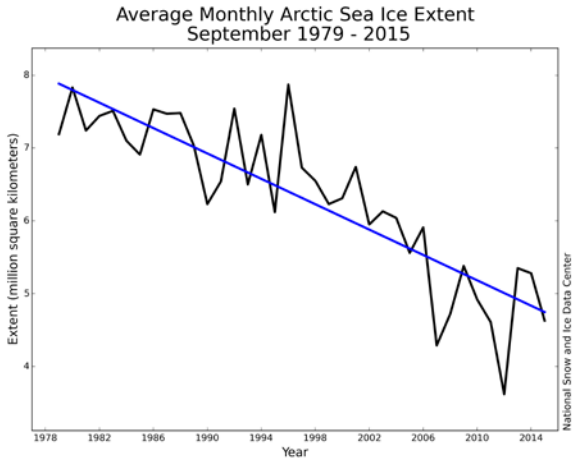

Figure 4. Monthly September Ice Extent for 1979 to 2015 Shows a Decline of 13.4% per Decade Relative to the 1981 to 2010 Average. Source: NSIDC (2015).

It has been predicted through many sources, that the sea ice will continue to decline and may see a nearly sea ice-free summer in this century. There is debate through several models and techniques on the exact year this will occur; nonetheless it is clear that it is a growing concern. The possible existence of an ice-free summer suggests a more seasonal sea ice region, which is very similar to the Antarctic sea ice season.

Stroeve et al. (2012) demonstrates the observed decline of the September sea ice extent over the past seven decades in Figure 5 (red solid line), with predicted continual decline up to the 21st century modeled by 20 World Climate Research Programme

Coupled Model Intercomparison Project Phase 5 (CMIP5) models. Furthermore, it is found that sea ice is thinning, since "at the end of summer 2011, only 25% of the ice was more than two years old, compared to 50–60% during the 1980s" (Stroeve et al. 2012). The sea ice retreat to date is ahead of the projected climate model trends.

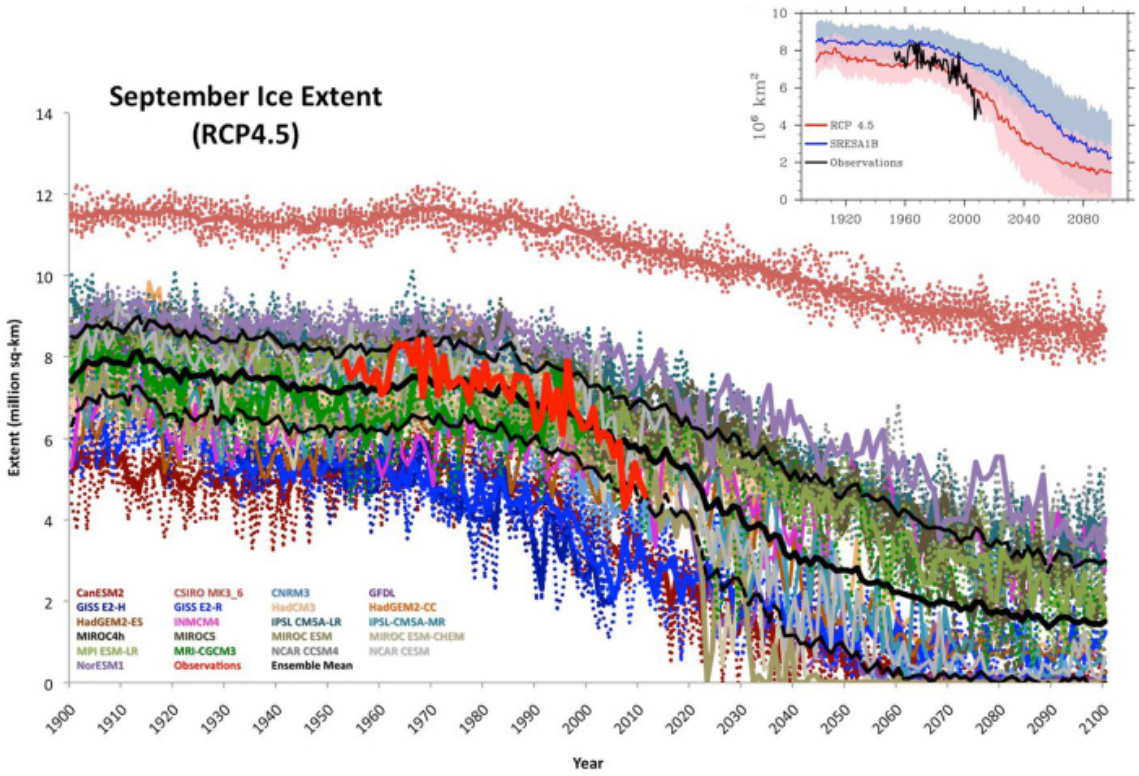

All 56 individual ensemble members from 20 CMIP5 models are included as dotted colored lines, with their individual model ensemble means in solid color lines. Observed data is represented by a solid red line. The multi-model ensemble mean is based on 38 ensemble members from 17 CMIP5 models (shown in black), with +/ 1 standard deviation shown as dotted black lines. Inset is based on the multi-model ensemble mean from CMIP5 and CMIP3, +/ 1 standard deviation.

Figure 5. Time-series of Modeled and Observed September Sea Ice Extent from 1900 to 2100. Source: Stroeve et al. (2012).

The predictions of a nearly ice-free summer in the Arctic range from the next few decades to late this century. The variability in the predictions depends on a number of different scenarios, techniques, resolution and parameters. The best estimate by Massonnet et al. (2012) for an ice-free summer is the interval of 2041–2060 for a high climate forcing scenario, including a number of sea ice metrics. Whereas, Overland et al.

(2013) suggests that there are three approaches to assessing an ice free summer. These include: “(1) extrapolation of sea ice volume data, (2) assuming several more rapid loss events such as 2007 and 2012, and (3) climate model projections.” The estimates are respectively 2020 or earlier, 2030 ±10years, and 2040 or later. Maslowski et al. (2012) adds to this debate and stipulates that there is still further advancement required for climate modeling to provide accurate estimates as “a system-level understanding of the critical Arctic processes and feedbacks is still lacking.” Nonetheless these predictions indicate that over the next few decades there will be a reduced sea ice extent in the Arctic, and to understand the impacts on global climate we must understand the current extent.

The maximum sea ice extent for 2016 was reached on March 24 (Figure 6a) at 14.52 million square kilometers, second to the lowest seasonal maximum in satellite record in March 2015 (NSICD 2016). The minimum sea ice extent for 2015 was set on September 11 (Figure 6b) at 4.41 million square kilometers, the fourth lowest in satellite record. This extent was 1.01 million square kilometers above the record low monthly average for September, which occurred in 2012 (NSICD 2015). Those events that have the lowest sea ice extent are generally associated with extreme weather events such as El Nino for example 2007 and 2012. A strong El Nino was present in 2015/2016 (NOAA 2016), which could contribute to the second lowest maximum sea ice extent in satellite record. Future extreme weather events could bring rise to further falls in sea ice decline ensuing an earlier onset of sea-ice free summers.

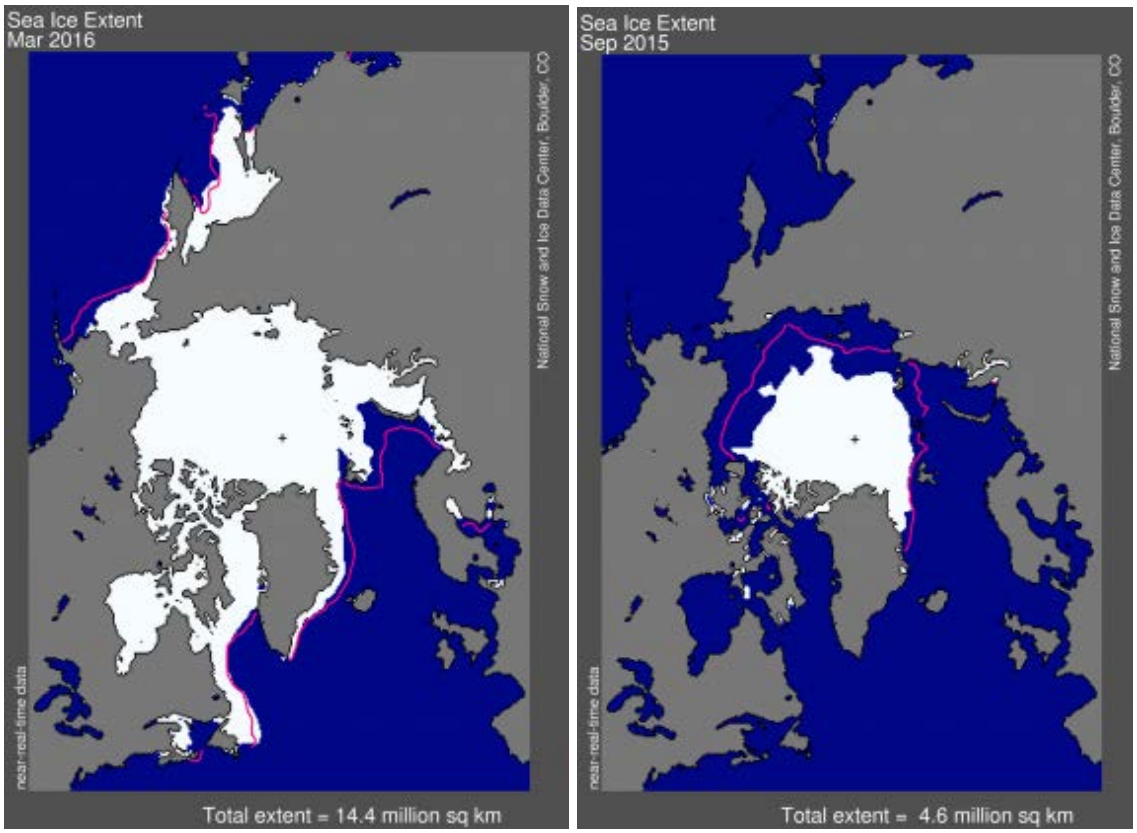

Left image a) March 2016 and right image b) September 2015. The magenta line shows the 1981 to 2010 median extent for that month. The black cross indicates the geographic North Pole.

Figure 6. Arctic Sea Ice Extent for March 2016 and September 2015. Source: NSIDC (2016).

Sea ice extent is a good indicator of the loss of sea ice, however volume is a more accurate indicator. Sea ice extent and thickness are the two parameters that determine volume. Thickness also provides an indication of the age of sea ice, such that the thinner the ice, the younger the ice. Observational data collected from the Special Sensor Microwave Imager and Sounder (SSMIS) on the Defense Meteorological Satellite Program (DMSP) F-17 satellite (UIUC 2016), is analyzed using the passive microwave brightness temperatures and then interpreted into graphics (Figure 7 a-d). The sea ice concentration for the month of August 1979 – 2015 (Figure 7 a-d) illustrates the decline in sea ice concentration, magenta representing 100%, red 60%, yellow 40% and blue 0%. It is of note that sea ice concentration below 30% is not shown.

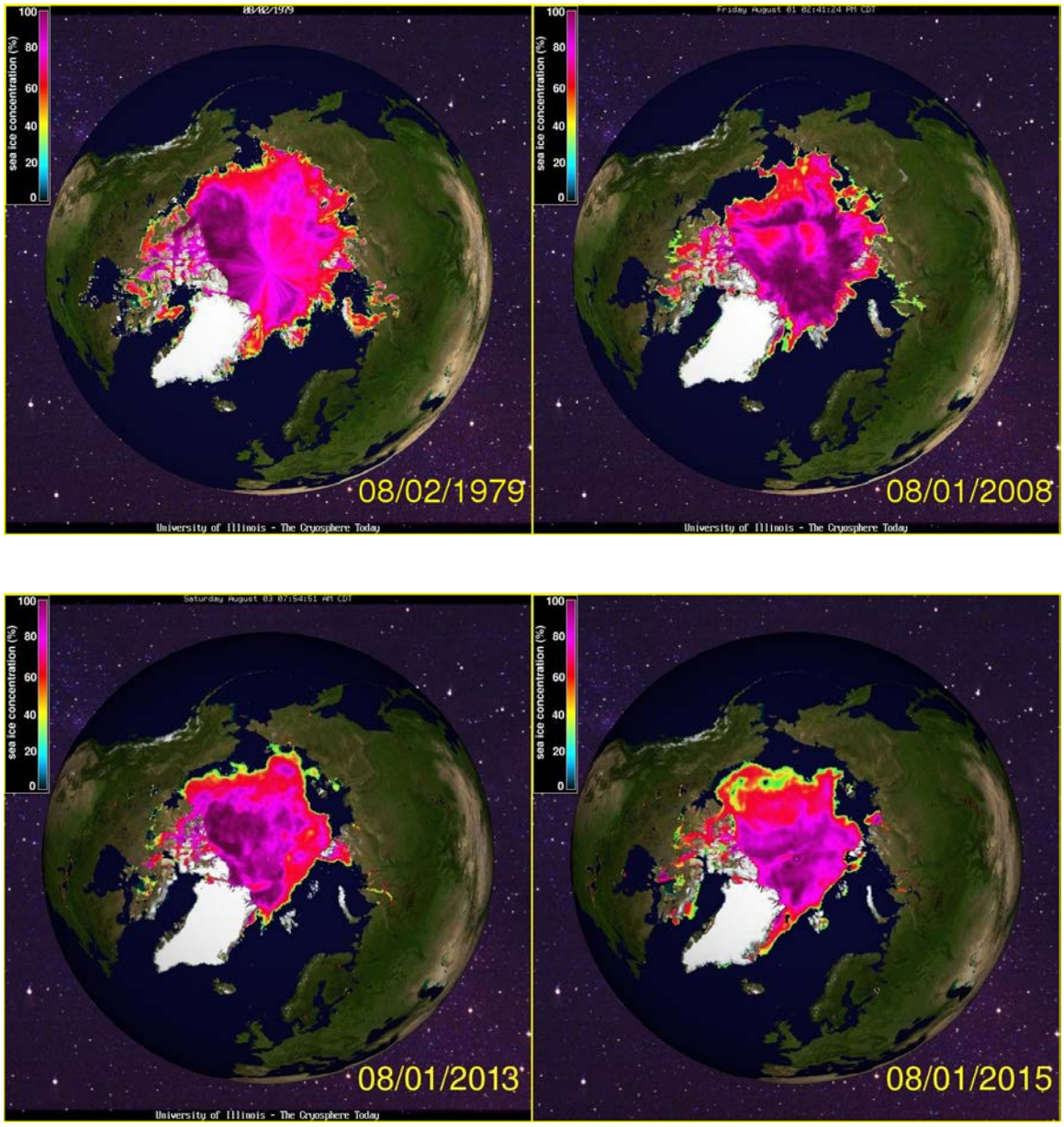

Top left a) is the sea ice concentration for the month of August for the beginning of the Cryosphere database. Top right b) is the sea ice concentration for the month of August for the year of the beginning of ITP data analyzed in this report. Bottom left c) is the sea ice concentration for the month of August for the end range of ITP data. Bottom right d) is the sea ice concentration for the month of August for the CTD analyzed in this report.

Figure 7. Northern Hemisphere Sea Ice concentration. Source: UIUC 2016.

NSIDC map of ice age for the summer of 2015 (Figure 8), revealed from the September minimum sea ice extent, that there was a 31% depletion of the multiyear ice cover, compared to only 12% in 2013 and 38% in 2012 (NSIDC 2015). From these

statistics, it can be construed that there is an increasing amount of first year sea ice, which is in agreement and similar to that observed in 2013: “last autumn’s record low and this winter’s record ice growth indicate a more pronounced seasonal cycle in Arctic sea ice and the increasing dominance of first-year ice in the Arctic” (NSIDC 2013). Moreover, Antarctica’s sea ice cover is seasonal and predominately first year ice (Turner and Pendlebury 2004). With further ice reduction and thinning ice expected in the Arctic from modeled predictions, conducting comparisons with the Antarctic Ocean, can provide some indication on how the Arctic Ocean properties may present in the future.

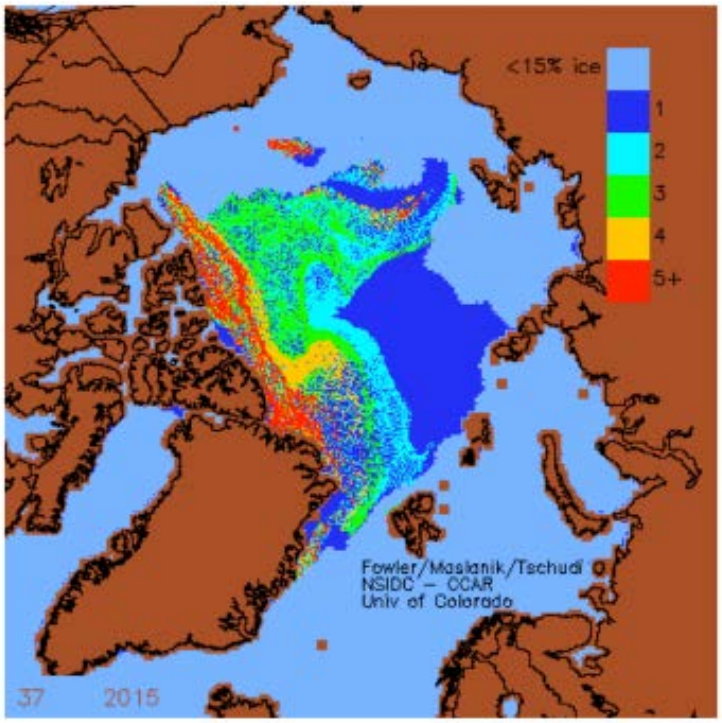

The map shows Arctic sea ice age, in years.

Figure 8. Arctic Sea Ice Age, September 7 to 13, 2015.
Source: NSIDC (2016).

The extent to which sea ice is thinning in the Arctic, and the exact timing of a near-free sea ice summer, is significant in respect to the degree they affect acoustic propagation. Thinning ice impacts the behavioral properties of sound energy in the ocean by increasing the sea state, which in turn increases mixing, and turbulence. This increased

mixing can deepen the mixed layer possibly lowering the cutoff frequency in the surface duct. Furthermore, nearly-free sea ice summers provide the opportunity for greater sea states that may affect scattering. Free sea ice oceans in the Artic provide for greater solar absorption, due to the ice-albedo feedback (Figure 9). A darker ocean absorbs more solar radiation than sea ice warming the ocean further and melting additional sea ice. This process has a positive feedback. Again, this warming of the ocean has a direct impact on the acoustic behavior of the water column by changing the thermohaline structure.

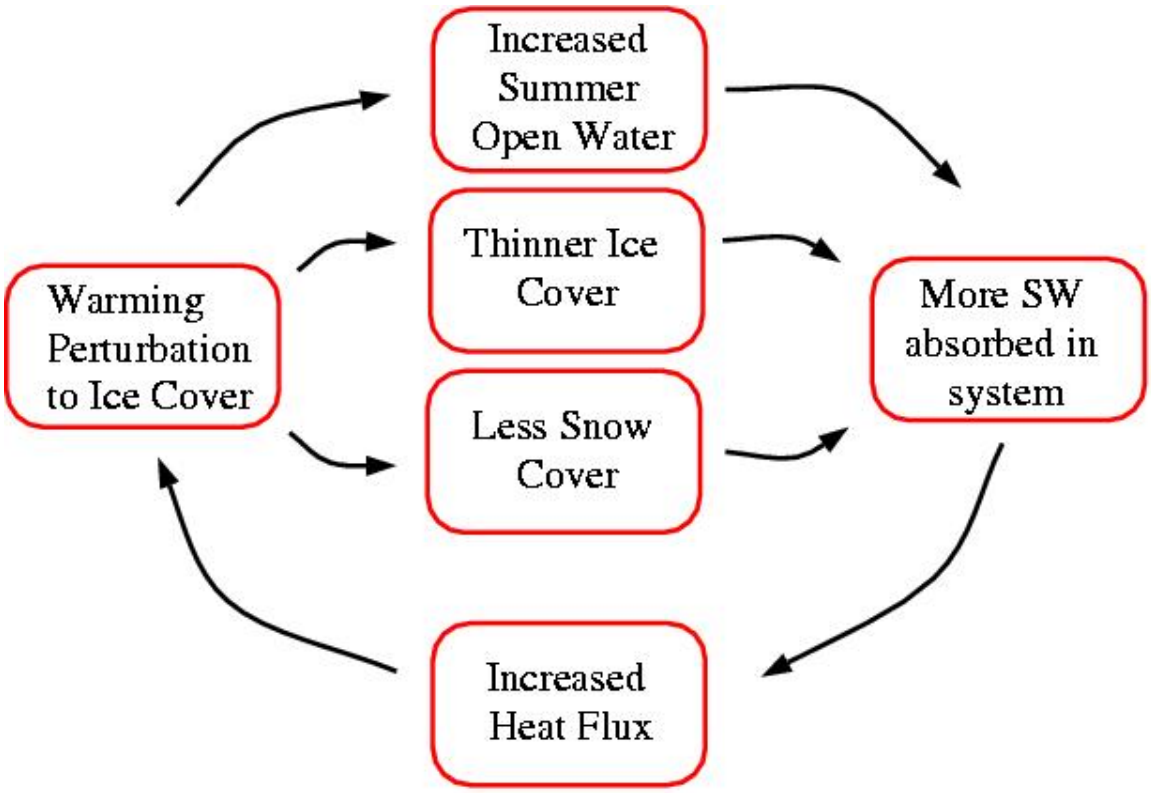

Figure 9. The Sea Ice/Albedo Feedback Mechanism. Source: Holland (2016).

D. NAVY RELEVANCE: THE IMPORTANCE OF UNDERSTANDING ACOUSTIC PROPAGATION AND HOW IT CAN AFFECT NAVAL OPERATIONS

Observations of large changes in the Arctic Ocean water column have been reported during the last 15 years (Rudels et al. 2004). These changes including the absence of mixing in both vertical and horizontal layers in the water column; warming or cooling of mixed layers; and the absence of low salinity surface water impacting heat transport (Rudels et al. 2004) which can alter the sound-speed profile. Variations in heat transport however, cannot just alter the sound-speed profile but physically reduce the ice formation. Variability in sea ice coverage including seasonality and type of sea ice not only affect the temperature of the water columns, particularly at the surface but also change the roughness, thickness and absorption of sound energy that interact with the surface. Depending on the surface properties, sound energy will experience variable attenuation and scattering. The variability in the Arctic Ocean water column will be the main focus of this study including the investigation into the impacts on acoustic propagation.

Due to reduction in sea ice in recent decades, the Arctic Ocean has become more accessible leaving large sections of the Arctic Ocean ice-free opening up shipping routes. These more accessible shipping routes have increased the volume of shipping (commercial or otherwise) in the Arctic Ocean, with further predicted increases (Eger 2011), being of interest to many nations. These changes will impact national security and naval operations in the area. Of note will be the contribution of increased shipping to the background ambient noise level.

The Arctic is not only more accessible to intercontinental transport, but also has led to the exposure of vast quantities of natural resources such as oil, gas and minerals to be extractable (Hansen et al. 2016). This accessibility creates expansion for the maritime industry in transport offshoring, servicing, emergency response, surveillance, maritime equipment, new build and retrofitting vessels (Hansen et al., 2016). The required infrastructure in the Arctic and surrounding Northern Hemisphere countries have not yet been fully established to support increased shipping in the area, and therefore, the

necessary actions need to be taken before such activities can occur. A number of these required action and activities such as research and safety, security, and the protection of national interests and sovereignty will attract the military to the Arctic.

In 2007, the U.S. government began implementing Arctic focused policies. In the policy, A Cooperative Strategy for 21st Century Seapower, the U.S. government acknowledged that "climate change is gradually opening up the waters of the Arctic, not only to new resource development, but also to new shipping routes" (Department of the Navy and U.S. Coast Guard 2007). Policy development over the years established further guidance through the U.S. Navy Strategic Objectives for the Arctic (May 2010), National Strategy for the Arctic Region (Apr 2013), U.S. Coast Guard Arctic Strategy (May 2013), Department of Defense Arctic Strategy (Nov 2013), Implementation Plan for the National Strategy for the Arctic Region (Jan 21014) and U.S. Navy Arctic Roadmap 2014–2030 (Feb 2014) revised from 2009. The two recent documents proclaim the Arctic as a new maritime frontier.

The Implementation Plan for the National Strategy for the Arctic Region was published in January 2014, and its purpose was to follow the three-line effort:

- advance United States security interests
- pursue responsible Arctic Region stewardship
- strengthen international cooperation

In addition, all lines of effort must employ a multi-disciplinary approach to research, and address emerging challenges and opportunities in the Arctic environment, both on a national and international level as well as in a military, social and scientific domain.

Southern hemisphere nations should take interest in the developments occurring in the Arctic especially those nations that are involved in the Antarctic Treaty. The policies adapted for the Arctic especially those concerning resources and international cooperation could apply to Antarctica, as there becomes more of a drive to exploit natural resources. The Antarctic Treaty could possibly be revised to include natural resource extraction. Furthermore, allied nations such as Australia and New Zealand to the United

States of America should be involved in Arctic operations and policies to provide support when needed. Activities in the Northern Hemisphere influence those that occur in the Southern Hemisphere. Polar research is a revived science that would benefit greatly from a collective approach.

More activity in the Arctic will require adaptation of vessels to endure the extreme weather and conditions. The atmosphere is more extreme, more harsh, and rapid in its changes. The ocean compared to the atmosphere is less volatile with changes being more consistent and gradual. In addition, vessels above the surface deal with extreme temperatures below -2C° incurring constant freezing conditions with sea spray, ice and snow. These vessels require equipment and procedures to mitigate below freezing temperatures. Vessels underwater such as submarines can adhere to better conditions under the ice encountering less hazardous currents and temperatures no less than -2C°. It could be beneficial to the military to have submarines operating in the Arctic in support of military operations and governance over surface vessels. The expected acoustic profile of the Arctic Ocean is very important entity if this concept is adopted.

Submarines have operated in the Arctic Ocean since the 1930s. In 1931 a decommissioned submarine, *O-12* and renamed the *Nautilus*, made several short runs under the Arctic sea ice, demonstrating that submarines could feasibly operate in and under sea ice (WHOI 2007). In 1947 *USS Boarfish* conducted the first official under-ice dives in the Arctic near the Chukchi Sea (SUBFOR 2016). Most under ice-dives up until 1958 were mainly conducted in ice-floes, when *USS Nautilus*, the first nuclear submarine reached the North Pole as well as conducted the first transpolar crossing (WHOI 2007). The same year USS Skate pushed through the ice at the North Pole. Other notable events for other nations were in 1962 the Soviets arrived on the *Leninski Komsomolets*, and in 1971 the British made the crossing on the *Dreadnought* (WHOI 2007).

In more recent history, a program called SCICEX (Science Ice Exercise) began in 1993. The program in collaboration between the U.S. Navy and the marine research community was “designed to use nuclear-powered submarines to map and sample the ice canopy; the physical, chemical, and biological water properties; the seafloor topography; and the shallow subsurface of the Arctic Ocean” (Edwards 2004).

The data collected from the submarines to support scientific research included:

- Conductivity, temperature, depth (CTD) profiles taken by expendable probes;
- CTD and other sensor data taken from hull- mounted systems;
- Bathymetry recorded by installed fathometers;
- Ice profile data from upward-looking sonar;
- Water samples for salinity calibration from water samples; and
- Navigation from the submarine's inertial navigation system (SCICEX Science Advisory Committee, 2010).

The U.S. Navy's submarine force is dedicated to contribute to the scientific research as well as maintain global presence. As stated in the SCICEX Science Advisory Committee, 2010 in the SCICEX Phase II Science Plan "the Navy believes its submarines must retain a global ocean operational capability and the Submarine Force is committed to sustaining Arctic training and readiness through recurring Arctic deployment." The plan is built around five sampling corridors within an agreed upon SCICEX Data Release Area (DRA) (SCICEX Science Advisory Committee, 2010). See yellow outline in the Figure 10. The article goes on further to claim that the essential data that helped scientist recognize global climate was changing were gathered during the SCICEX Phase I between 1993 and 1999 (SCICEX Science Advisory Committee 2010).

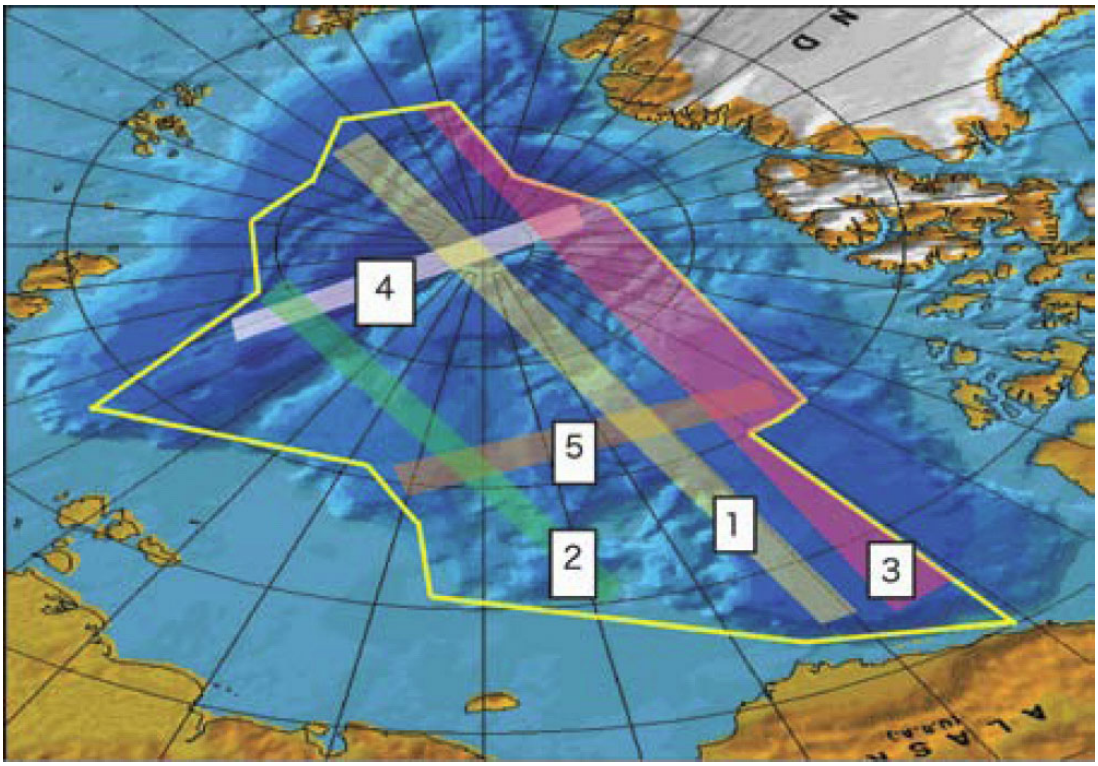

The science plan is built around five recommended sampling corridors within the SCICEX Data Release Area. The areas provide reference for planning tracks and for priorities of scientific data collection. The SCICEX Phase II Science Plan (SCICEX Science Advisory Committee, 2010) explains in further detail of each corridor.

Figure 10. SCICEX Data Release Area. Source: SCICEX Science Advisory Committee (2010).

The SCICEX program in conjunction with Ice Exercise (ICEX) is held biennial involving other agencies and surface components. SCICEX is still continuing to this day and will be expected to continue into the future. It is necessary to understand the changing Arctic Ocean properties not only for scientific research but also for safe and productive submarine operations.

Understanding the spatial and temporal variations in the Arctic on sound speed will improve the knowledge of the current and predicted acoustic propagation properties of the Arctic Ocean. This will better equip the military and other government organizations with the knowledge on the difference between expected background noise, and the generated signal therefore providing greater assistance in maritime operations, particularly underwater operations and anti/submarine warfare.

THIS PAGE INTENTIONALLY LEFT BLANK

II. OCEAN ACOUSTIC VARIABILITY

A. ACOUSTIC BASICS

Sound in the ocean compared to other waves such as electromagnetic (EM) radiation, is a useful tool for remote sensing, communications, and navigation. This is owing to the fact that the ocean is transparent to low frequency sound and opaque to EM radiation.

Sound speed (c(z)) in the ocean is a function of temperature, salinity and pressure (function of depth), and can be defined by the simple equation:

$c(z) = 1449.2 + 4.6T - 0.055T2 + 0.00029T3 + (1.34 - 0.001T)(S - 35) + 0.016z)$, *(1)*

where temperature (T) is in degrees centigrade, salinity (S) is in parts per thousand and depth (z) is in meters (Medwin 1975). More accurate sound speed equations are given by Del Grosso (1974), but this example suffices to show the basic dependencies. Sound speed is seen to increase with increases in all dependent variables, but temperature is the strongest.

B. ACOUSTIC VARIABILITY

Ocean acoustic fields are determined by the ocean sound speed structure, which invariably includes small-scale random fluctuations in sound speed (δc). Some ocean processes that are known to affect acoustic propagation are mixing, internal waves, eddies and fronts, spicy thermohaline structure, and the effects of interactions with the rough seabed and sea surface. In addition, the specific environments of the ocean will affect sound propagation, and some examples include mid-latitude deep ocean, mixed layer, shallow water and continental shelf, and polar regions. A typical Canada Basin profile is discussed in the Chapter I.

1. Ray Theory

A simple starting place to understand sound propagation in the ocean is ray theory. Ray theory is a useful technique to understand the physics of scattering sound in relation to ocean acoustic propagation due to its strong geometric basis (Colosi 2016). In

this theory, the wave field of acoustic energy, *p(r,t)* behaves locally like a plane wave and propagates perpendicular to the wave front. We write the acoustic pressure in the form

$$p(\boldsymbol{r}, t) = A(\boldsymbol{r}, t)e^{i\Theta(\boldsymbol{r},t)}, \quad (2)$$

where $A(\boldsymbol{r}, t)$is the amplitude and $\Theta(\boldsymbol{r}, t)$ is the phase. The phase is assumed to vary much more rapidly than the amplitude.

For ray theory, it is of particular interest, that only refraction is accounted for and not diffraction. Here the ray path can be written in the form of either, θ_g, which is the grazing angle or the ray angle at the sound channel axis for upper and lower turning depth z^+ and z^-. Assuming the phase function Θ(r,t) is locally in the form of a plane wave we can write

$$\boldsymbol{k} = \nabla\Theta, \quad (3)$$

$$\omega = -\frac{\partial\Theta}{\partial t}. \quad (4)$$

where ω and **k** are related by the plane wave dispersion relation, ω=(**k, r**). Manipulating Equation (3) and (4) gives the following equation

$$\frac{\partial \boldsymbol{k}}{\partial t} = -\left(\frac{\partial\omega}{\partial \boldsymbol{k}} \cdot \nabla\right)\boldsymbol{k} - \frac{\partial\omega}{\partial \boldsymbol{r}}, \quad (5)$$

where the group velocity is identified as $c_g = \frac{\partial w}{\partial \boldsymbol{k}}$ and the total derivative is given by $\frac{d}{dt} = \frac{\partial}{\partial t} + c_g \cdot \nabla$ in the direction of the wave. For wave energy following along ray paths the Hamiltonian-like equations (Lighthill, 1978) are applicable

$$\frac{d\boldsymbol{r}}{dt} = \frac{\partial\omega}{\partial \boldsymbol{k}} = c_g, \quad (6)$$

$$\frac{d\boldsymbol{k}}{dt} = -\frac{\partial\omega}{\partial \boldsymbol{r}}. \quad (7)$$

where the Hamiltonian function is given by the wave dispersion relation.

Equation (6) says that the acoustic energy travel along the ray at the group velocity, and Equation (7) says that the direction of the ray changes due to spatial variations in the dispersion relation often termed refraction (Colosi 2016). As a result from Hamiltonian method, the dispersion relation, ω is constant and therefore, $\frac{d\omega}{d\boldsymbol{t}} = 0$. Hamiltonian mechanics can be used to explain acoustic propagation with c(x,y,z) in terms of ray chaos and the exponential sensitivity to initial conditions (Colosi 2016).

In ray amplitude and stability, the exponential sensitivities to initial conditions and perturbations in sound speed waves caused from such phenomena as internal waves is called ray chaos (Colosi 2016). It will not be discussed in depth in this thesis, but it is important to understand initial conditions can significantly impact acoustic propagation. The divergence or convergence of nearby waves can possibly increase eigenrays allowing chaotic rays to be detected at range.

In this thesis, we will examine acoustics in a simpler 2-D plane where x is the independent variable, and we want to predict the acoustic field at a point (x, z). This then gives 3 equations (independent of acoustic frequency (since $k_z \propto \omega$)) for ray direction, $k_z(z(x))$, ray path, $z(x)$, and travel time, $T(x)$, becoming,

$$\frac{1}{\omega}\frac{dy}{dx} = -\frac{1}{(c^{-2}-k_z^2/\omega^2)^{\frac{1}{2}}}\frac{1}{c^3}c, \tag{8}$$

$$\frac{dz}{dx} = \frac{k_z}{\omega}\frac{1}{(c^{-2}-k_z^2/\omega^2)^{\frac{1}{2}}} = tan\,\theta, \tag{9}$$

$$\frac{dT}{dx} = \frac{1}{c^2(c^{-2}-k_z^2/\omega^2)^{\frac{1}{2}}}. \tag{10}$$

Here a frequency independent quantity called the vertical ray slowness is defined as $p_z = \frac{k_z}{\omega} = \frac{\sin\theta}{c}$ where p_z does not depend on ω. A new Hamiltonian function, H, is also defined with conjugate or phase space variables (p_z, z) and is given as

$$\frac{dz}{dx} = \frac{\partial H}{\partial p_z}, \frac{dp_z}{dx} = \frac{-\partial H}{\partial z}, \tag{11}$$

where $H = -\frac{k_x}{\omega} = -(c^{-2} - p_z^2)^{\frac{1}{2}} = -\frac{\cos\theta}{c}$.

The third equation is then

$$\frac{dT}{dx} = L = p_z\frac{dz}{dx} - H = \frac{1}{c^2(c^{-2}-p_z^2)^{\frac{1}{2}}} = \frac{sec\,\theta}{c}, \tag{12}$$

where L is the Lagrangian function. Equation (12) states that the ray path moves at the local sound speed where $\frac{dT}{ds} = \frac{1}{c}$ and the infinitesimal arc length is $s = (dx^2 + dz^2)^{\frac{1}{2}}$.

In short, the Hamiltonian equations are a pair of coupled, non-linear equations because $c(x, z)$is a non-linear function. Also, the travel time equation is simply an auxiliary equation, $\Theta \propto \omega T$ (Colosi 2016).

The above theory gives the wave phase as a function of position and time and a separate equation is used to compute the ray amplitude giving the acoustic pressure as

$$p(\boldsymbol{r},t) = \sum_j a_j(\boldsymbol{r},t)e^{-i\omega(T_j(\boldsymbol{r})-t)}. \quad (13)$$

Here, the sum is over all rays (eigenrays) that pass through the position **r**.

There are a number of methods to analyze acoustic propagation as well as represent them in graphical plots. For this thesis the pressure field will be inferred by transmission loss (TL). TL for a single frequency at a point source with pressure referenced at r=1m for a spherical wave, $p_0(r) = e^{ik_s r}/(4\pi r)$ where $k_s = \omega/c_s$. TL can written as

$$TL = -20log_{10}\left(\frac{|p(r,z;\omega)|}{|p_0(r=1;\,\omega)|}\right). \quad (14)$$

2. Ocean Sound Speed Variability

An important source of sound speed variability in the oceans is internal waves. Internal waves are gravity waves that ride upon the density stratification of the ocean and are much like surface gravity waves that ride on the density contrast of the air/sea interface. Internal waves induce sound speed changes by vertically advecting density surfaces. In a vertically stratified ocean, the sound speed is therefore $c(z + \zeta(r,t))$ where $\zeta(r,t)$ is the internal wave vertical displacement. Taylor expanding the sound speed perturbation is given by

$$\delta c(r,t) = \left(\frac{dc(z)}{dz}\right)_p \zeta(r,t), \quad (15)$$

where the vertical gradient is the total gradient minus the adiabatic gradient, due to the adiabatic nature of displacements (Colosi 2016).

Three main factors concerning internal wave-induced sound-speed fluctuations are that they are (1) inhomogeneous in depth with larger fluctuations in the main thermocline and small ones at depth, (2) anisotropic in the vertical/horizontal plane with horizontal and vertical correlation length of roughly 10km and 0.1km, respectively and (3) intrinsically waves having their own space/time dependence imposed through the dispersion relation (Colosi 2016).

Internal waves (super-inertial variability) fit into four broad categories: Inertial waves, internal tides, internal solitary waves and broadband stochastic random waves. Inertial waves are evident near the local inertial frequency *f* in horizontal current spectra and are mainly wind driven. Internal tides are observed near continental shelves and rough topography. For latitudes above 30 degrees, only semi-diurnal tides exist and at even higher latitudes greater than 75degress they are largely absent. This is due to the cut-off in the M2 tidal component. Furthermore, in deep water internal tides can be more deterministic due to their relation to astronomical tides. Internal solitary waves are nonlinear internal waves that are largely generated on continental shells and sills from bottom interacting tidal flows.

Kinematically, internal wave frequencies are found to be between the Coriolis frequency f and the Brunt-Vaisala frequency N. The Brunt-Vaisala (or buoyancy) frequency N(z) is the frequency with which a vertically displaced fluid element would be expected to oscillate (Garrett and Munk 1979). It is an indicator for the local gravitational stability of the stratification (Colosi 2016).

Eddies (or sub-inertial variability) exist on time scales larger than internal waves. Eddy time scales are weeks to months and therefore due to the short duration of the CANAPE pilot study, detailed statistical properties of eddies cannot be addressed. Figure 21 (Chapter III) shows indications of two significant eddies, one at the beginning and one at the end of the experiment.

Another process that generates small-scale random sound-speed fluctuations is spice. Spice is associated with intrusive thermohaline fine structure, which exists due to mixing of water masses with differing temperature and salinity. Along surfaces of constant density, temperature and salinity can vary in a compensating way. This compensated variability is termed spice: High spice is classified as hot and salty water, and low spice, is classified as cold and fresh water. Ocean fronts, shallow water, and the surface mixed layer are consider regions of strong spice. Sound-speed anomalies are produced by density compensating temperature, and salinity anomalies because sound speed increase with both temperature and salinity (Colosi 2016).

Because spice has no density signature it is dynamically insignificant, that is to say there is no intrinsic dynamical time dependence to the spice. We see time changes in spice because the spatial structure of the spice is advected by ocean currents including internal waves and eddies.

In this thesis, spice and internal wave analysis will be done hand in hand. To note, one difference spice has compared to internal waves is that it has no essential intrinsic time evolution, (i.e., zero frequency) and thus temporal behavior is dictated by advection (Colosi 2016).

3. Effects of Sound Speed Fluctuations on Acoustic Fields

Now we address how the sound speed fluctuations, like those caused by internal waves or spice, lead to acoustic variability. Initially sound-speed fluctuations or heterogeneities in the water column will cause a planar wavefront to become weakly distorted. Because rays propagate perpendicular to the wavefront, focusing and defocusing regions form (Figure 11). This causes amplitude and phase variability along the wave front.

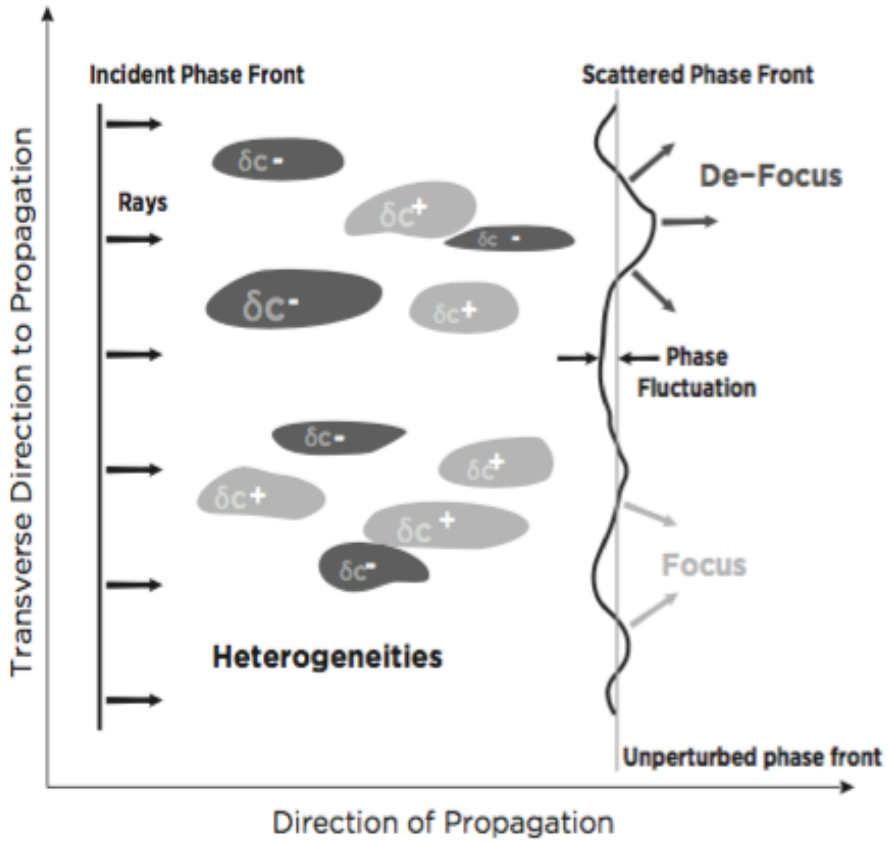

Using the Born and Rytov theory, phase fluctuations appear to first order and give rise to focusing and de-focusing; e.g., intensity variability. Focusing can be understood in terms of the bending of the phase front. The physical picture is of multiple weak forward scattering.

Figure 11. Plane Wave Passing through a Region of Weakly Variable Sound Speed Showing Areas of Focusing and Defocusing. Source: Colosi (2016).

As the sound travels further and further into the fluctuating ocean, the front experiences stronger distortions. In particular, focusing regions will lead to a folding or triplication of the wave front (Figure 12) (Colosi 2016). A triplication occurs when opposite sides of a focusing region cross one another or fold over, forming three segments of the wave front instead of only one (Colosi 2016). Locally increased intensity can form at the two permanent focusing regions (caustics), demonstrated in the right panel in Figure 12 at the edges of the triplication. Interference can play a role in this regime causing fluctuations to be large. Triplication then leads to many microrays as

triplications occur over and over again. As range increases the microrays become more randomized and their strong interference leads to saturation, which is a manifestation of the central limit theorem.

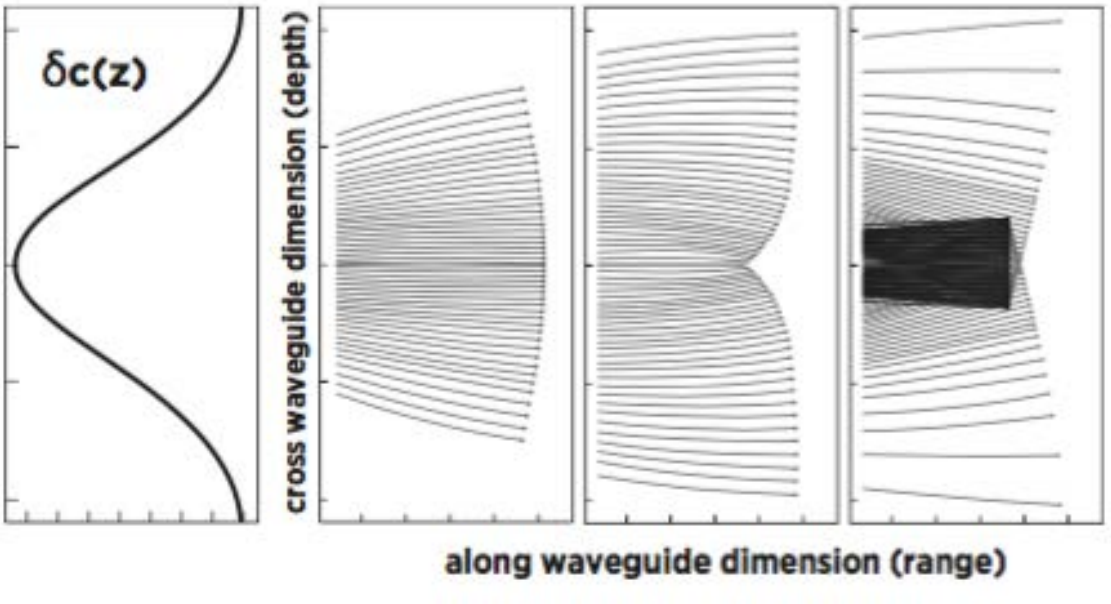

From left to right are shown three stages of wave front folding caused by the low sound speed zone depicted at far left. Lines mark distinct ray paths, and circles at the ends of the rays show the location of the wave front. In the first frame, the initial circular arc of the wave front is straightened out nearly into a plane wave by the refraction effects of the low speed zone. By the second frame the low speed zone produces a significant distortion of the front with a focusing zone near the low speed axis. By frame three, rays on either side of the focusing zone have crossed over one another and created a triplication.

Figure 12. Folding and Triplication of the Wave Front Due to Strong Fluctuations. Source: Colosi (2016)

Micro-ray interference leads to scintillation described by the unsaturated, partially saturated, and fully saturated wave propagation regimes (Figure 13). To quantify the variability in these regimes the scintillation index (SI) and the log-intensity are used. SI is the normalized intensity variance given by

$$SI = \frac{<I^2> - <I>^2}{<I>^2}, \qquad (16)$$

and the log-intensity ($\iota = \ln I$) variance is

$$\sigma_\iota^2 = <\iota^2> - <\iota>^2. \qquad (17)$$

The scintillation index is sensitive to high intensity fluctuations, while the log-intensity variance is sensitive to fading due to the logarithmic distortion of low intensities (Colosi 2016).

Two parameters important in acoustic regimes are the strength parameter Φ, and the diffraction parameter Λ (Flatte et al. 1979; Esswein and Flatte 198; Flatte 1983). These parameters are functions of ray geometry, acoustic frequency and medium parameters. Medium parameters such as the internal wave spectra will be examined in the internal wave and spice section in Chapter IV. We will not address computing Lambda Phi parameters for our arctic acoustic conditions.

The strength parameter Φ is specifically related to root mean square (RMS) travel time fluctuation, since $\tau = \frac{\Phi}{\omega}$ s and is the RMS phase in the geometric acoustic limit (Colosi 2016). It "is expressed as an integral along the unperturbed ray of the depth dependent fractional sound speed variance times the correlation length of sound-speed fluctuations along the direction of the ray" (Colosi 2016). To note, the curvature of the ray must be taken into account to correct for large grazing angle rays when using the assumption in the correlation length, L_p, that the ray is locally a straight line (Colosi 2016). Definition of Λ is the average acoustical length divided by the ocean correlation length of the internal waves.

Two limiting cases concerning these two parameters in the three propagation regimes become,

$$\textit{Geometric Acoustics}\left((\Lambda \ll 1) \quad \langle\phi^2\rangle = \Phi^2, \langle\chi^2\rangle = C\Lambda\Phi^2\right), \tag{18}$$

$$\textit{Large Diffraction}\left((\Lambda \gg 1) \quad \langle\phi^2\rangle = \frac{\Phi^2}{2}, \langle\chi^2\rangle = \frac{\Phi^2}{2}\right) \tag{19}$$

For geometrical acoustics, the log-amplitude variance is much less than the phase variance whereas, in diffraction acoustics, diffraction reduces the phase variance, working against strong focusing.

The behavior of these parameters, diffraction parameter, Λ, and the strength parameter, Φ, can delineate the different propagation regimes (Figure 13). There is no scale on the x-axis as background profiles of the ocean, ray paths, source/receiver

locations, and frequency can change the ranges at when the regimes happen (Colosi 2016). At high frequency, SI saturates to 1, which is expected from strong microray interference (Colosi 2016). The approaches to saturation can be from above or below SI=1, subject to the phase and amplitude statistics of the interferers and the signal bandwidth.

The approach from above comes from the partially saturated regime. Here this regime, due to strong focusing in the partially saturated zone is considered a small wavelength or high frequency regime, where diffraction is small, thus $\Lambda \ll 1$. In the approach to saturation from below 1, this regime is considered to have high diffraction due to the lack of strong focusing, thus $\Lambda \gg 1$. For the unsaturated regime, for small SI both the geometric (small wavelength) and diffraction (large wavelength) regimes are found (Colosi 2016). The characteristics are set out in Table 1. Additionally, diffraction depends on acoustic frequency and the spectrum of internal waves.

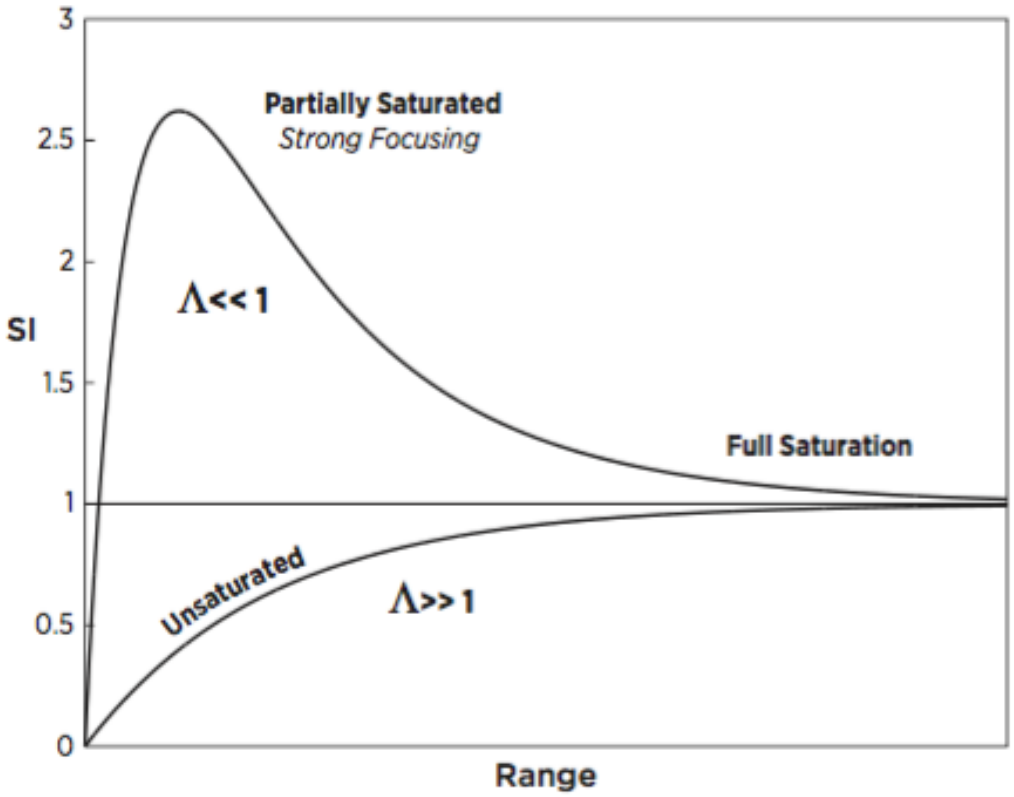

Figure 13. Statistical Characteristics of the Signal Intensity.
Source: Colosi (2016).

The characteristics of each regime are set out in Table 1.

Table 1. Characteristic of Fluctuation Regimes

	Unsaturated	Partially Saturated (Strong Focusing)	Fully Saturated
Microrays	No microrays	Many correlated microrays	Large number of uncorrelated microrays
SI	0<SI<0.3	0.3 < SI < 2	SI ~ 1
RMS Intensity	1-3 dB	3-10 dB	~ 5.6 dB
PDF of Intensity	PDF of log I is normal distribution	PDF of I unknown	PDF of I is exponential (similar to noise)
Coherence	Coherence is high (maximum possible gain)	Moderate Coherence	Low Coherence

THIS PAGE INTENTIONALLY LEFT BLANK

III. DATA DESCRIPTION

A. DESCRIPTION OF THE OBSERVATIONAL DATA SETS, SPATIAL AND TEMPORAL

1. Canada Basin Acoustic Propagation Experiment

A recent short pilot study in the Canada Basin was conducted from 23 July to 21 August of 2015 as part of the Canada Basin Acoustic Propagation Experiment (CANAPE). CANAPE is an experiment in collaboration with Scripps Institution of Oceanography, the Naval Postgraduate School (NPS), and the Office of Naval Research (ONR). The aim of the experiment was to study the "effects of changing Arctic conditions on low-frequency, deep-water propagation and on the low-frequency ambient noise field" (Worcester et al. 2014).

The pilot experiment consisted of observations in both the temporal and spatial domain. This data was recorded by a single Distributed Vertical Line Array (DVLA) mooring, and the icebreaker research vessel R/V Sikuliaq.

In addition to the DVLA data, 11 shipboard Conductivity, Temperature and Depth (CTD) profiles were cast from 26 July to 18 Aug 2015. The CTDs were taken between latitude 71 21.44 N and 73 38.91N and longitude 147 17.77W and 157 26.67W, with depths ranging from 99 to 3835m. More detailed CTD information is in Table 2. The DVLA was located at 73 10.67N, 154 06.06W (Figure 14) in a water depth of 3853m.

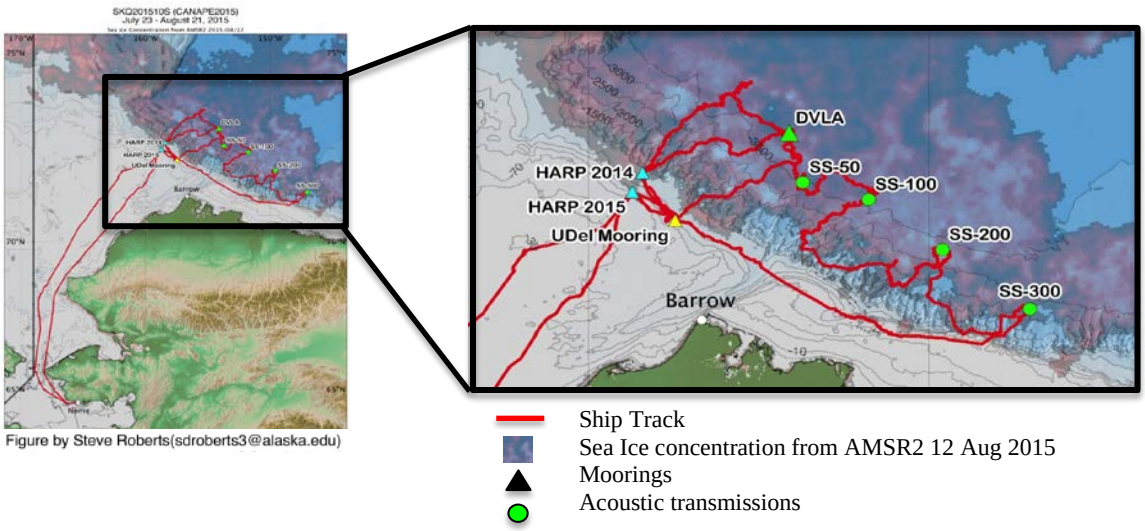

Icebreaking research vessel R/V Sikuliaq was used for the pilot CANAPE voyage to deploy DVLA and CTD equipment as well as record data.

Figure 14. Map Showing DVLA Position. Source: Worcester (2015b).

Table 2. CTD and DVLA Information

CTD Number	Date - 2015	Latitude	Longitude	Distance from DVLA (km)	Depth
DVLA	30 Jul -16 Aug	73 10.67N	154 06.06W		3853
1	Jul 26	72 20.18 N	157 26.67 W	144.78	162
2	Jul 27	73 27.01 N	156 06.18 W	71.00	3721
3	Aug 03	73 38.65 N	155 13.10 W	62.96	3850
4	Aug 06	72 38.91 N	153 48.56 W	59.56	3325
5	Aug 06	72 28.71 N	152 14.16 W	98.69	3485
6	Aug 10	72 03.51 N	149 49.35 W	188.51	3270
7	Aug 12	71 21.44 N	147 17.77 W	306.23	530
8	Aug 12	71 21.40 N	147 18.73 W	305.88	2355
9	Aug 17	73 11.41 N	154 05.77 W	1.35	3835
10	Aug 18	72 21.53 N	157 22.86 W	141.51	190
11	Aug 18	72 36.48 N	158 40.85 W	162.89	99

Three CTDs (1, 10, and 11, shown in black on Figure 15) were excluded from the analysis, as they were located on the Canadian shelf. The DVLA comprised of 60 hydrophones modules, 24 temperature and conductivity sensors (Sea-Bird SBE 37-SMP/SM MicroCATs), and 2 Acoustic Doppler Current Profiles (Teledyne RDI 75-kHz and 150-kHz ADCPs). The temperature, salinity and pressure sensors on the DVLA spanned a depth between 85–650 m and the ADCPs were placed at 600m, one orientated to look upwards and the other orientated to look downwards. The ADCPs were deployed to measure horizontal currents. Table 3 shows the placement of the instruments on the DVLA.

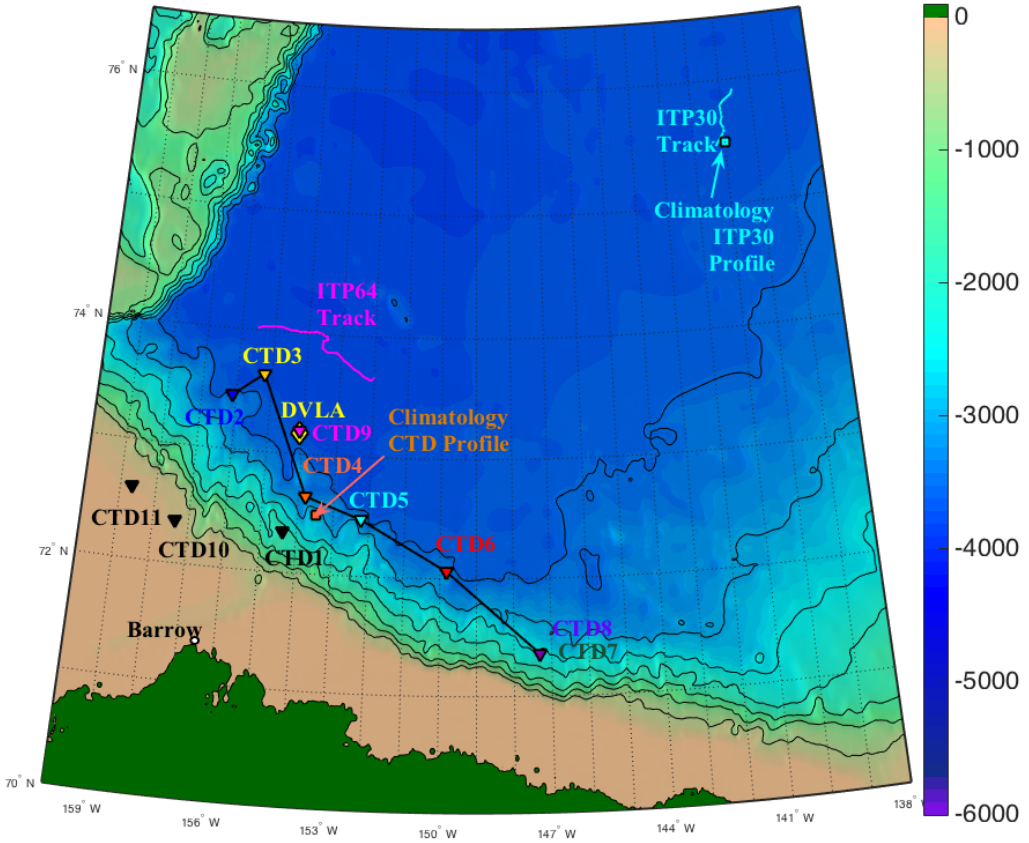

Markers in black represent CTDs excluded from analysis

Figure 15. DVLA and CTD Positions

Table 3. DLVA Instrument Placement with Approximate Depth. Source: DiMaggio et al. (2016).

Depth (m)	Instrument
82	SBE37-SMP
102	SBE37-SMP
111	SBE37-SMP
120	SBE37-SMP
129	SBE37-SMP
138	SBE37-SMP
147	SBE37-SMP
156	SBE37-SMP
165	SBE37-SMP
175	SBE37-SMP
183	SBE37-SMP
192	SBE37-SMP
210	SBE37-SMP
228	SBE37-SMP
247	SBE37-SMP
265	SBE37-SMP
292	SBE37-SMP
320	SBE37-SMP
347	SBE37-SMP
381	SBE37-SM
418	SBE37-SM
452	SBE37-SM
489	SBE37-SM
525	SBE37-SM
628	ADCP (75 kHz) upward looking
641	ADCP (150 kHz) downward looking

The primary instruments are Seabird Electronics models SBE37-SM and SBE37-SMP (pumped) MicroCATs. The SBE instruments sampled the ocean at 30 sec intervals. The 75 kHz ADCP was deployed in the up looking direction and the 150 kHz ADCP was deployed in the down looking direction.

The CANAPE Pilot Study data set was selected for this thesis due to its high quality and its temporal and vertical resolution. The shipboard CTD data will be used in this study to quantify full water column and horizontal variability (Figure 16 and 17). The DVLA data will be used to investigate the temporal and vertical structure of internal waves, eddies, internal tides, random internal waves and spicy thermohaline structure

(Figure 20). To understand the variability from both data sets the mean of temperature, salinity, sound speed, potential density, potential sound speed gradient and buoyancy frequency was computed and displayed Figure 16. The three profiles near the DVLA were superimposed on in the first 85m of the profiles as the DVLA data commenced at the lower depth. Further discussion on this variability is mentioned in the next subsection. Buoyancy Frequency (N(z)) was introduced in Chapter I.

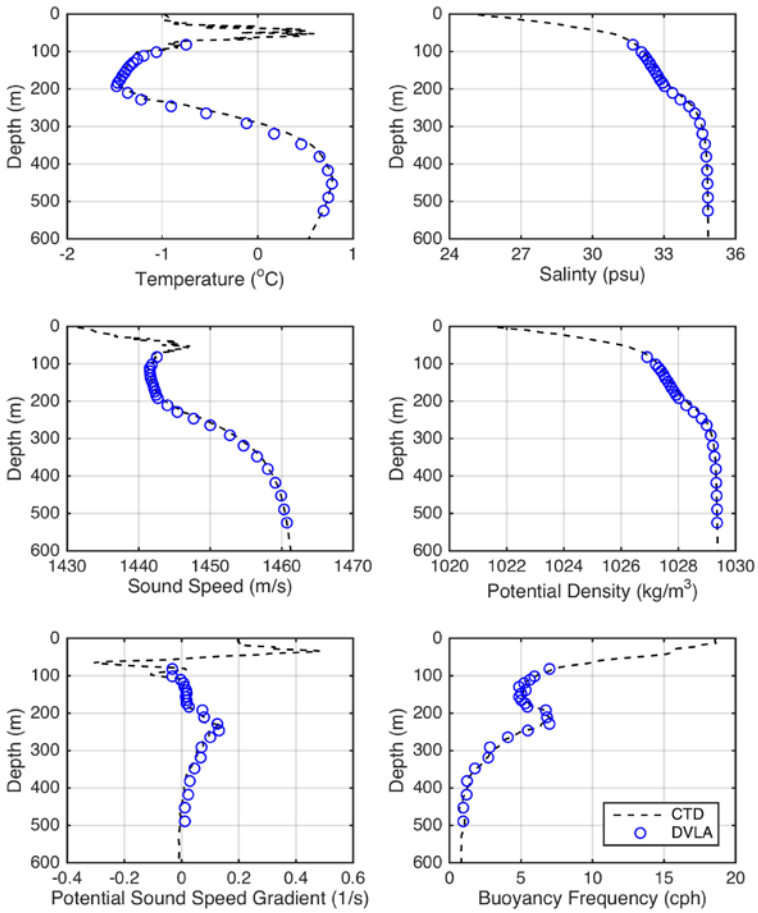

Mean profiles of temperature, salinity, sound speed, potential density, potential sound speed gradient and buoyancy frequency. Values derived from the DVLA are show with circles. Average profiles derived from 3 CTD casts made in the vicinity of the DVLA are shown with dashed lines.

Figure 16. Mean Profiles of Buoyancy Frequency and Potential Sound Speed Gradient for CANAPE data. Source: DiMaggio et al. (2016).

a. CANAPE CTD Observations

The CANAPE CTD data was used for the vertical spatial analysis, particularly in the upper 100m as the DVLA mooring data started at 85m. The vertical measurements of temperature, salinity, pressure, conductivity and sound speed were measured every 1m from the surface to the sea floor and recorded every meter.

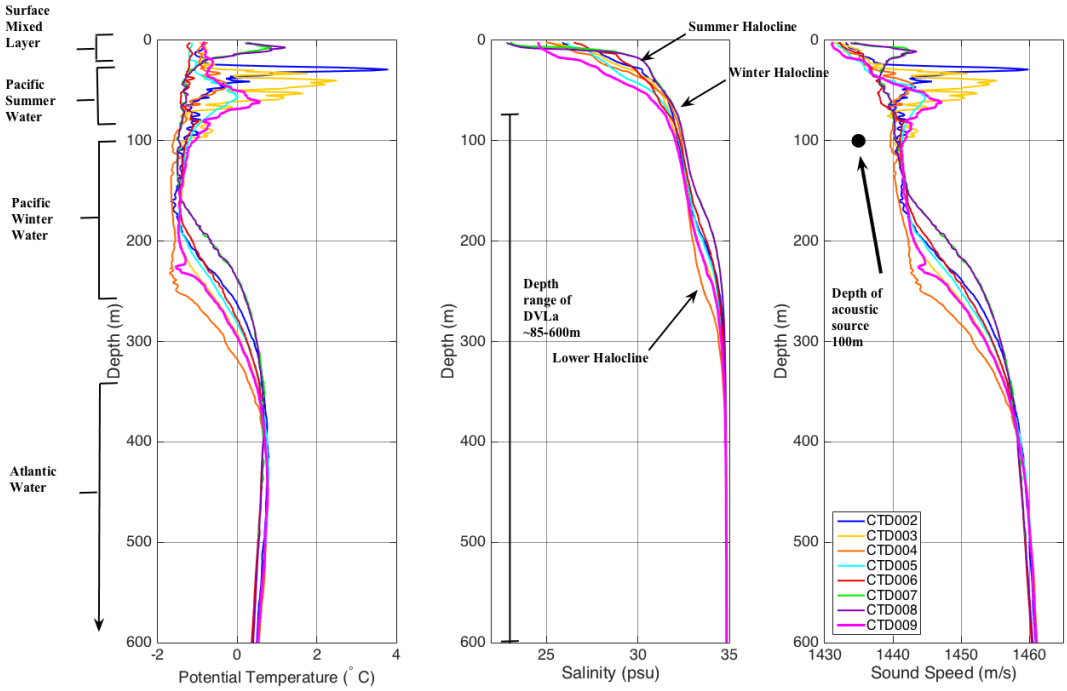

Figure 17. CANAPE CTD Potential Temperature, Salinity and Sound Speed Profiles with Over Laying Water Masses.
Source: DiMaggio et al. (2016).

The upper 600m will be the main focus for the remainder of this thesis, shown in Figure 16–-20, displaying the four upper distinct water masses and the variability in these depths. The surface layer in the upper 40m is defined by a temperature of approximately -1°C, and a salinity less than 30 psu. The NSTM exists below this layer representing the upper limit of the PSW characterized by the mean CTD temperatures between 0 to 1°C, and salinities between 30 and 32 psu. In this study the NSTM is lower than the typical depth of the NSTM mentioned in Chapter I. CTD002 and CTD003 show temperatures

above this range. They are further north, however they are closer to the Bering Strait where the warm Pacific Water enters the Arctic Ocean. Below the PSW layer between 100 and 200m, lies the cooler PWW layer with temperatures less than -1°C and salinities between 32 and 33 psu. The Atlantic Water layer is separated from the Pacific origin waters by a lower halocline. Predominately the Atlantic Water layer is warmer than the Pacific waters with temperatures greater than 0°C, however due to its salty origins this layer is denser with a high salinity value of 34.8psu.

This upper 600m water structure is highly stratified and corresponds with changes in the sound speed structure, which is significant to acoustic propagation, as discussed in Chapter II. At the NSTM a reciprocal maximum of sound speed at 50m was observed, corresponding to the upper boundary of the PSW. The upper boundary of the PWW (100m-120m) delineated a minimum temperature, which was associated with a minimum in sound speed. Sound speed then gradually increases below the PWW. In the CANAPE study the acoustic source was placed at a depth of 100m. The placement was a requirement for the equipment to be readily accessible so as to switch off for approaching marine mammals. This will be of considerable acoustic interest as the sound speed minimum was directly below this depth, and in association with the upper refracting acoustic conditions, due to increasing sound speed below the PWW; signals could travel greater distances with lower transmission loss.

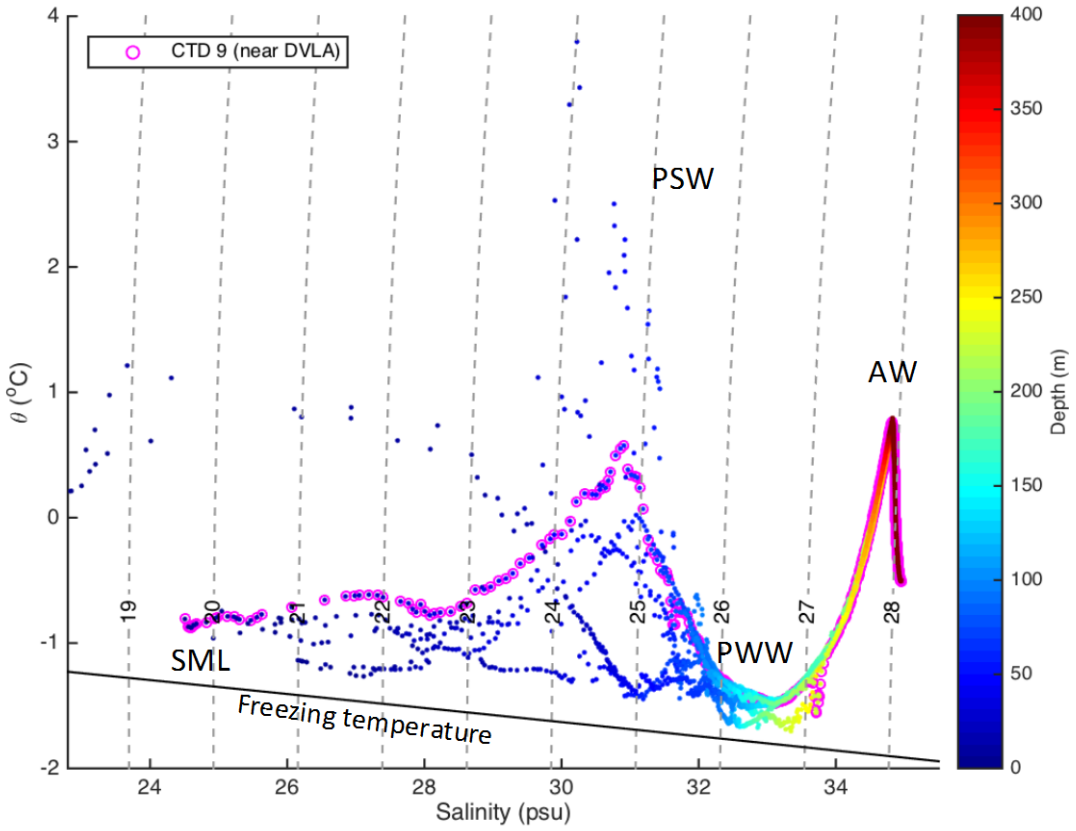

The color of each data point corresponds to a depth observation. The dashed lines are contours of constant potential density measured in kg/m^3 with freezing temperature as a function of salinity represented by a solid line. The highlighted points in magenta represent the observations by CTD9 near the DVLA mooring. Names of water masses are determined by known salinity and potential temperature characteristics.

Figure 18. Potential Temperature and Salinity Plotted on an Isopycnal Field for CANAPE CTD Data. Source: DiMaggio et al. (2016).

Figures 18 and 19 show the variability in temperature, salinity and sound speed. The largest variance seen in temperature is in the upper 100m at 4°C^2 near the NSTM, which correspond to the maximum variance of sound speed. For salinity, the largest variance at 2 psu^2 is closer to the surface and is possibly due to the by-product of the changing is sea ice (melting/freezing). For all three parameters, there is another zone of relatively high variance at depths between 200–300m corresponding to the lower regions of the PSW and the upper region of the PWW. This region also accommodates the minimum temperature and the lower halocline.

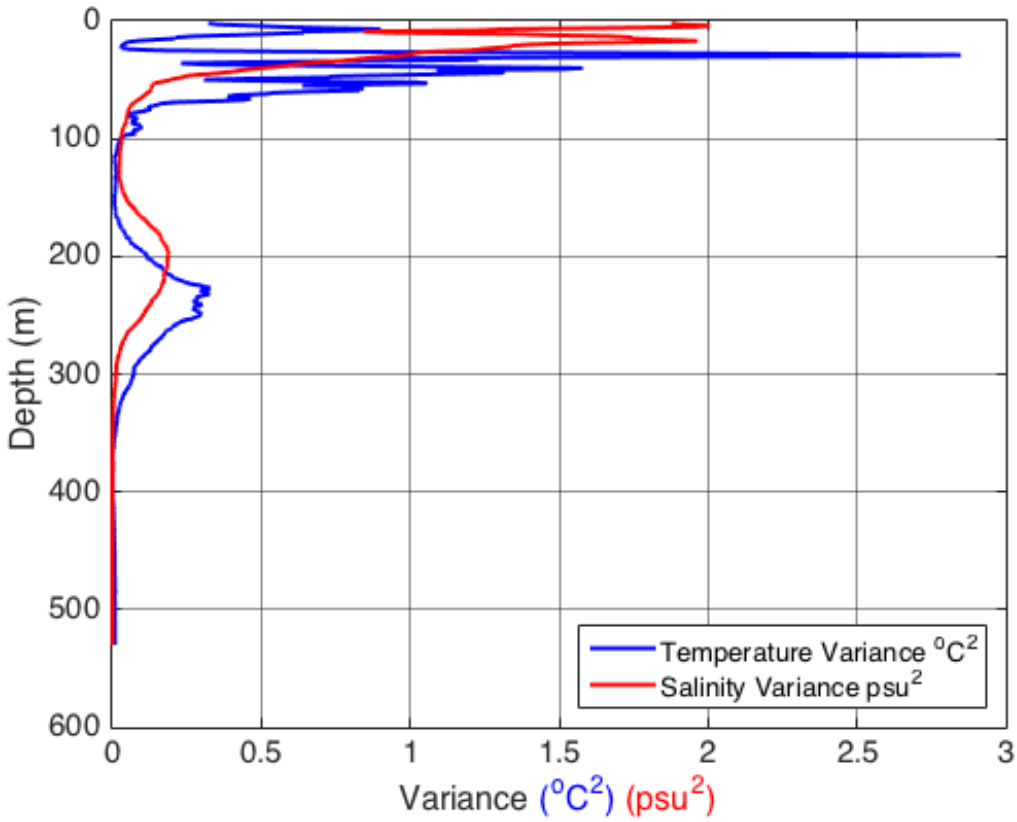

Figure 19. Variance of Temperature (blue) and Variance of Salinity (red) versus Depth for CANAPE CTD Data Set.

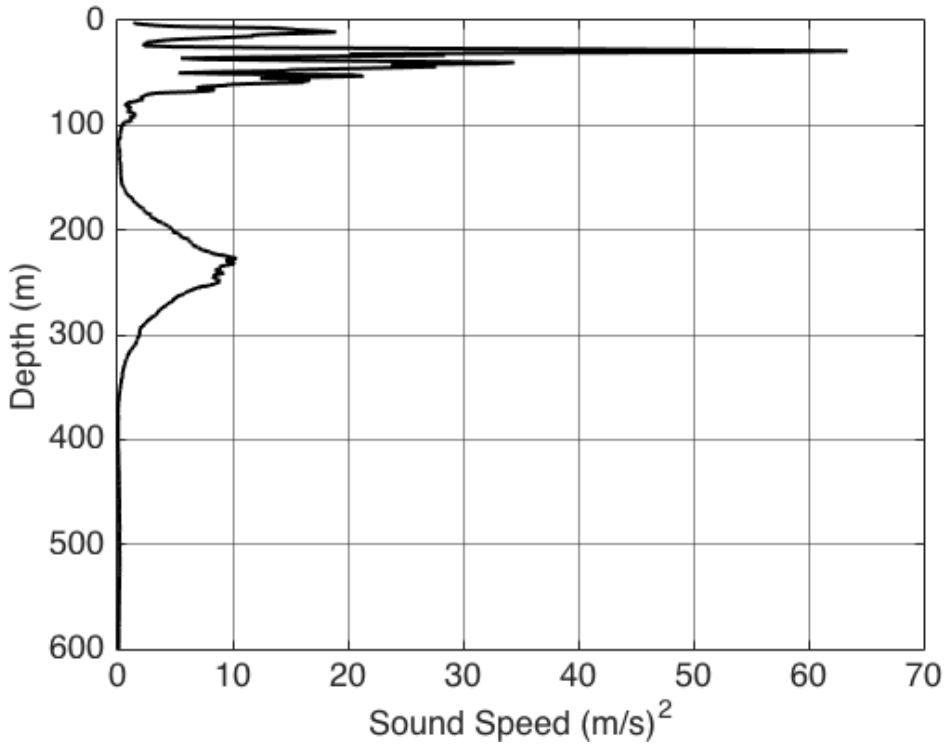

Figure 20. Variance of Sound Speed versus Depth for CANAPE CTD data set.

b. CANAPE Moored Observations

The DVLA mooring data set was utilized for the temporal analysis due to the continual deployment of the mooring with a sampling of temperature, salinity and pressure were measured every 30 seconds.

The depth-time series and temporal structure of temperature and potential density are shown in Figure 21 from the DVLA data set. Overlaid in black are lines of constant potential density demonstrating the dormant environment of the Beaufort Sea. An unexplained pull down event occurred between yeardays 212 and 215, and therefore the data after the yearday 216 (04 August) is only analyzed in this thesis. Depth-time series of computed potential density provided indication of turbulent properties, for example any variability due to internal waves or eddies. A noteworthy feature is present at the end of the series in the upper 250m, which could be accounted for by the presence of a highly stratified event such as an eddy with both temperature and potential density raised in this range. Displaying observations along isopycnals can provide clear analysis for variations

in sound speed structure due to the density compensating nature of temperature and salinity in relation to sound speed (Dzieciuch et al. 2004). Further discussions on the analysis of sound speed variations are in Chapter VI.

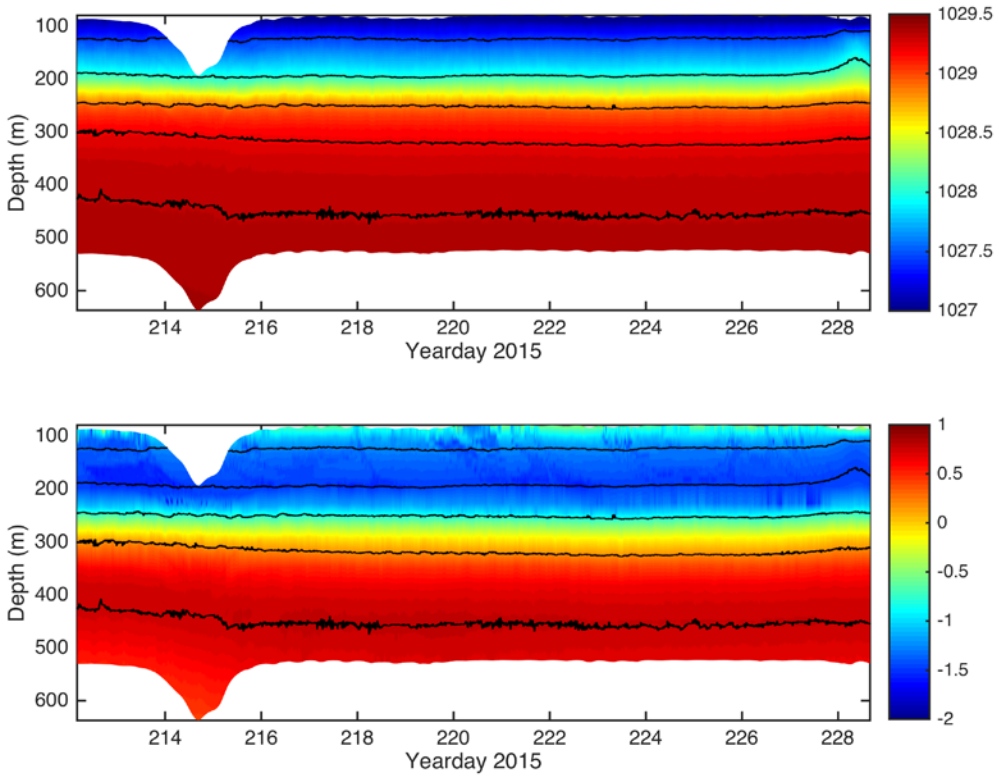

Top graph represents depth-time series of potential density in kg/m^3 and bottom represents depth-time series of temperature in degrees Celsius measured at the DVLA mooring. Lines of constant potential density (isopycnals) are overlaid in black.

Figure 21. Depth-Time Series of Potential Density in kg/m^3 and Temperature in Degrees Celsius. Source: DiMaggio et al. (2016).

2. Ice Tethered Profile (ITP)

To analyze the current Arctic water column characteristics and the recent changes, a data set was created from Ice Tethered Profiles from the past decade. The ITP data was collected and made available by the Ice-Tethered Profiler Program (Toole et al. 2011; Krishfield et al., 2008) based at the Woods Hole Oceanographic Institution (http://www.whoi.edu/itp).

The ITP system consists of three components: a surface instrument package that sits atop an ice floe, a weighted, wire-rope tether of arbitrary length (up to 800 m) suspended from the surface package, and an instrumented underwater unit that travels up and down the wire tether

Each ITP is expected to return 1600 or more high-vertical-resolution profiles of upper Arctic Ocean temperature and salinity in near real time spanning all seasons over a three-year lifetime. The raw CTD and associated engineering data files are relayed from the underwater vehicle to the surface buoy at the completion of each one-way profile, which then transmits them to a logger computer at WHOI via satellite. Full-resolution CTD and engineering data are transmitted to shore. (WHOI 2016).

A schematic drawing of the instrument is given in Figure 22.

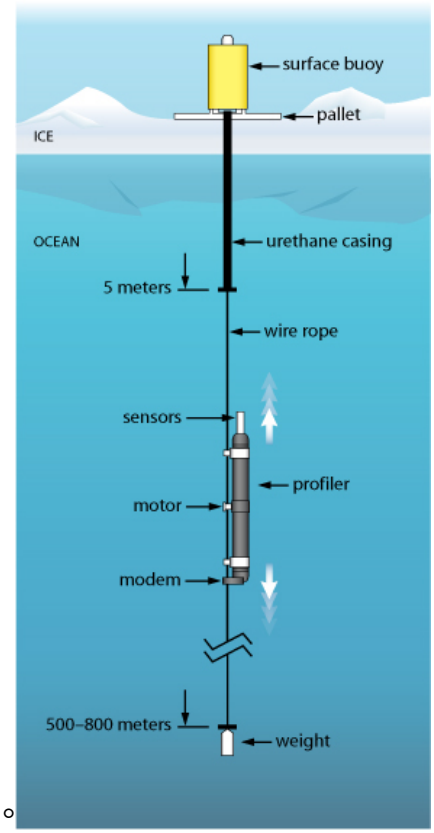

Figure 22. Ice-Tethered Profiler Schematic. Source: WHOI (2016).

The downloaded files were selected on a number of criteria. This criteria included: timeframe from July to August; location within the bounds of east to west, 135°W to 160°W, and south to north, 72°N and 77°N; and quality controlled to level 3 Archive Data. Level 3 Archive Data are the best estimates from WHOI derived from the ITP sensor observations, quality controlled and corrected. A full description of the ITP data processing procedure can be found at WHOI (http://www.whoi.edu/fileserver.do?id=35803&pt=2&p=41486). The file-formatted data used had been pressure-bin-averaged at 1-db vertical resolution (WHOI 2016).

Further scrutiny was involved in the selection of ITP data, and only a few were eventually used for the comparison with the CANAPE data sets. Two ITP data sets were chosen out of the downloaded files for ease of analysis and to determine eliminate conclusions. Criteria for the selection was that the ITPs were to be deployed in minimal ice thickness. The CTDs were deployed in the MIZ and open water and therefore, for realistic results minimal ice thickness was preferable for the ITPs as they were tethered to ice. The thickness ranged from 2–7m, with those chosen to be about 2.4m.

A few of the ITPs were deployed in thin sea ice thickness, however to provide variance in conditions, specifically sea ice extent, the final ITP data sets were chosen from years with ice extent being above or below that for 2015, the year of the CANAPE pilot study. The sea ice extent was determined using NSIDC Charctic Sea Ice Graph tool (Figure 23). The ideal years selected from the available years for the ITP dataset were 2009 and 2012. ITP30 and ITP64 were deployed in the year 2009 and 2012 respectively. Figure 15 displays their positions.

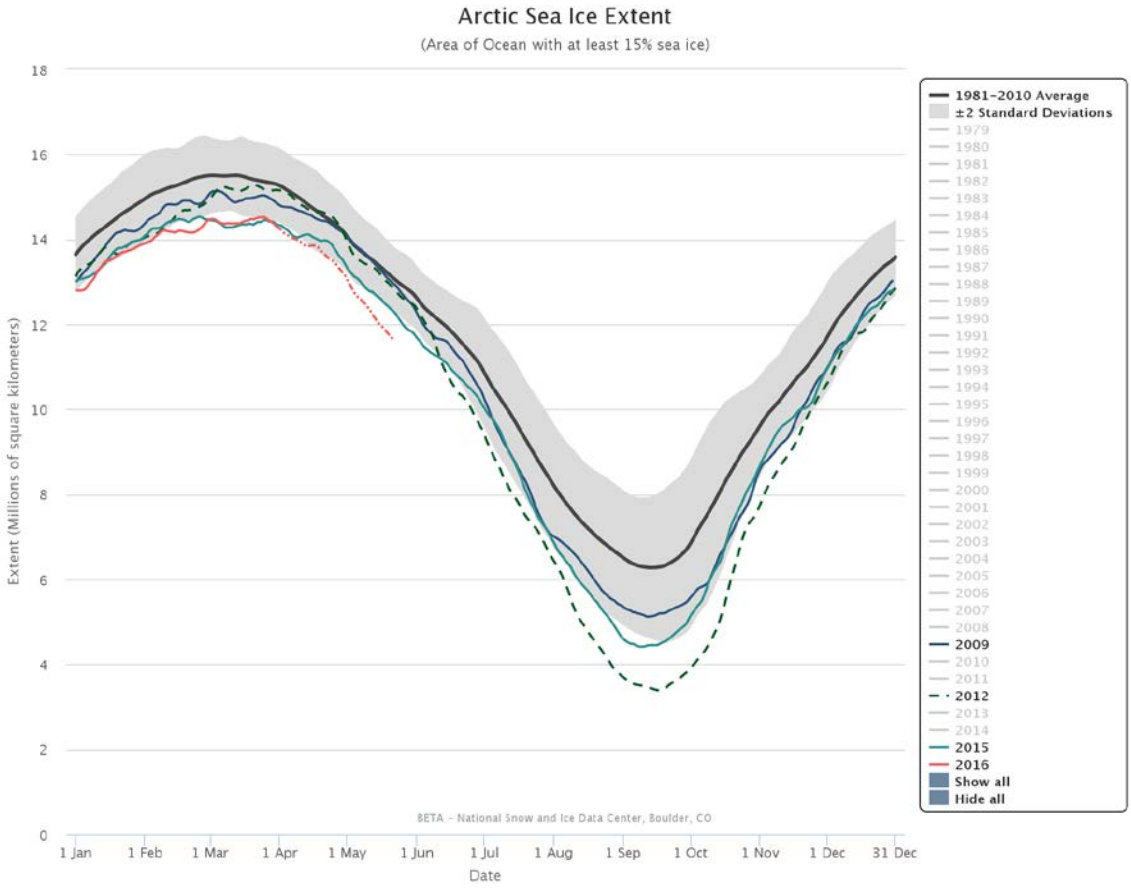

Sea ice extent for years 2009, 2012, 2015 and the beginning of 2016 were lower than the 1981–2010 average. 2015 sea ice extent lies in between years 2009 and 2012.

Figure 23. Charctic Interactive Sea Ice Graph displaying Arctic Sea Ice Extent for 2009, 2012, 2015 and 2016. Source: NSIDC (2016b).

Variables calculated from ITP data and analyzed were temperature, potential temperature, salinity, pressure, sound speed and depth. Four to six profiles were collected for ITP30 and ITP64. Their potential temperature, salinity and sound speed versus depth are shown in Figure 24 and Figure 25, which show small amounts of variability.

In Figure 24 the ITP30 data set shows a small amount of variability in the upper 200m of the potential temperature and sound speed profile with little to none below 200m. For the ITP64 set (Figure 25), an even less variability for the profiles selected were present in the upper 200m.

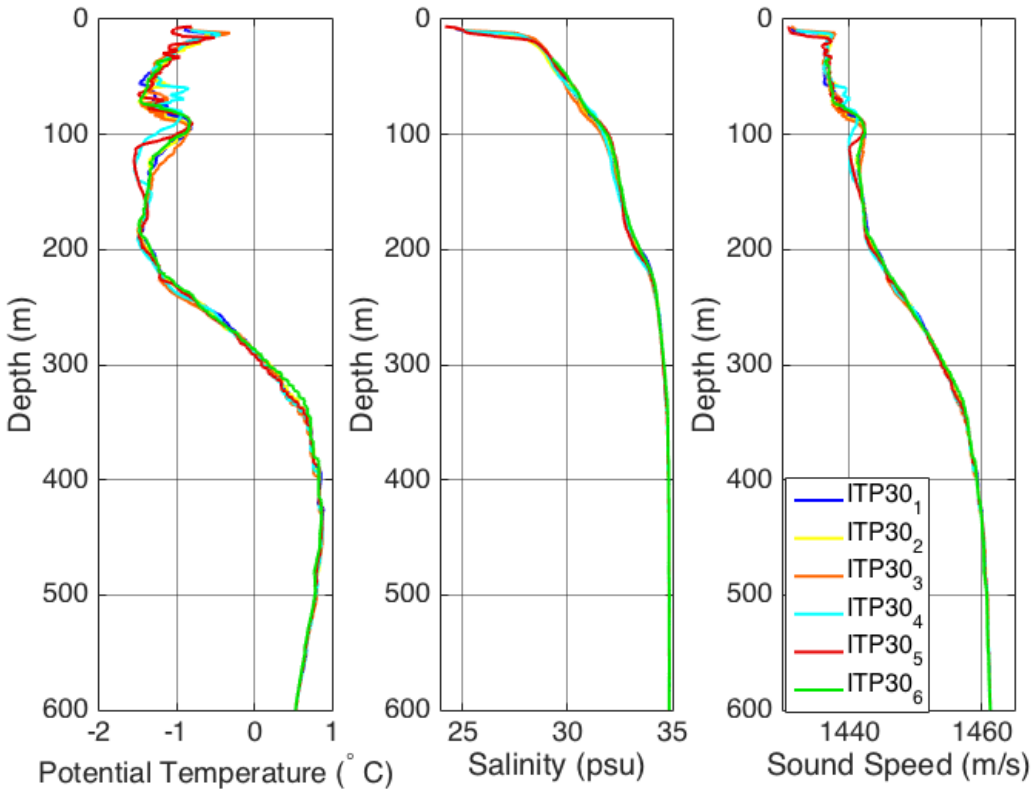

Figure 24. Potential Temperature, Salinity and Sound Speed Profiles of the ITP30 Data Set

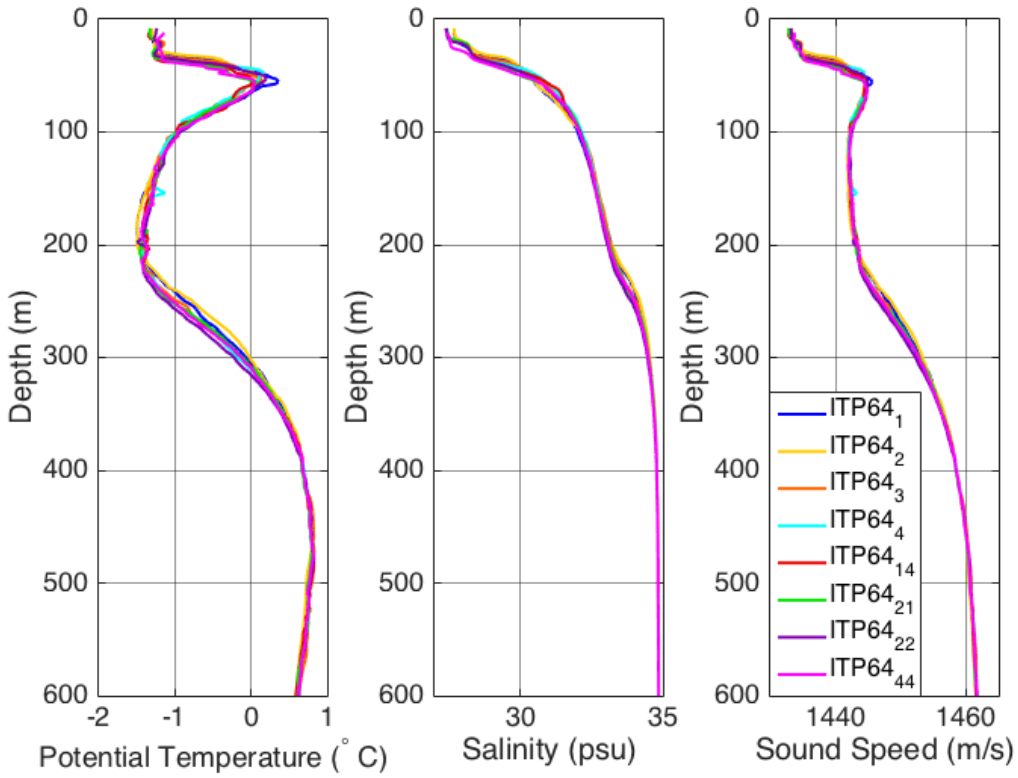

Figure 25. Potential Temperature, Salinity and Sound Speed Profiles of the ITP64 Data Set

B. DESCRIPTION OF THE CLIMATOLOGY

Climatology is often used in models to set a base standard. In ocean modeling the climatology database that is generally used is the World Ocean Atlas (WOA) from the National Oceanographic Data Center (NODC) (amalgamated into National Centers for Environmental Information (NCEI)), and operated by the National Oceanic and Atmospheric Administration (NOAA).

For the analysis in this thesis the Arctic Regional Climatology (https://www.nodc.noaa.gov/OC5/regional_climate/arctic/section) from WOA was selected. The area found in the Arctic Regional Climatology encompasses all longitudes from 60°N to 90°N latitudes (NCEI, Arctic Regional Climatology, 2015). Climatological profiles along the CTD track as well as in position near the ITPs were collected and

compared (Figure 26). ITP64 was close to the CTD climatology, and so it was stipulated to only have a separate climatology data set for the ITP30 data set.

The climatological mean format chosen was presented in a comma separated value (csv) format, which gives latitude/longitude of the center of a grid box and the value at each depth in that grid box (NCEI, Arctic Regional Climatology, 2015).

The horizontal resolution of temperature and salinity were on a 1°x1° latitude/longitude grid. The vertical resolution is available at 87 standard levels, with the depths extending from surface to 4000m (NCEI, Arctic Regional Climatology 2015). The times chosen for this analysis were for the months of July and August.

Also available from WOA were the climatological fields of statistical means (before objective analysis), standard deviation, standard error, data distribution, observed minus analyzed, and difference of time period from annual climatological. Further, descriptions of the data can be found at (NCEI, Arctic Regional Climatology 2015) (https://www.nodc.noaa.gov/OC5/regional_climate/arctic/about_arctic.html). The WOA profiles only reached 1500m depth, and were adapted with profiles collected from the U.S. Navy's Generalized Digital Environmental Model (GDEM) climatology database for the depths below 1500m to the sea bed. Sounds speed is predominately affected by only pressure changes below depth, and therefore, considered reasonable to use the GDEM to complete the profiles.

GDEM "is a four-dimensional (4-D) steady-state digital model of ocean temperature and salinity" (Allen and NAVOCEANO 2012). The model has a spatial resolution of 30 arc minutes and temporal resolution of 3, 6, or 12 months intervals. Vertical profiles of historical temperature and salinity from the surface to the sea floor are available for all locations where the water depth is at least 100 m.

The data base is continually being updated by the Naval Oceanography Office and dates back to 1920. There are over 4.5-million profiles of temperature/salinity.

Climatology profiles were selected for positions near the CTD profiles at 72.5N 154.5W and the ITP30 at 75.5 N 141.00W. Potential temperature, salinity and sound

speed profiles are shown in Figures 26 and 27 for climatology for CTDs and ITP respectively.

CTD climatology shows little change; in fact, less than 1°C of variability between the four profiles selected. Increased temperature corresponds to an increase in sound speed. For the ITP30 climatology, again little variability was present, and mainly occurred in the upper 200m.

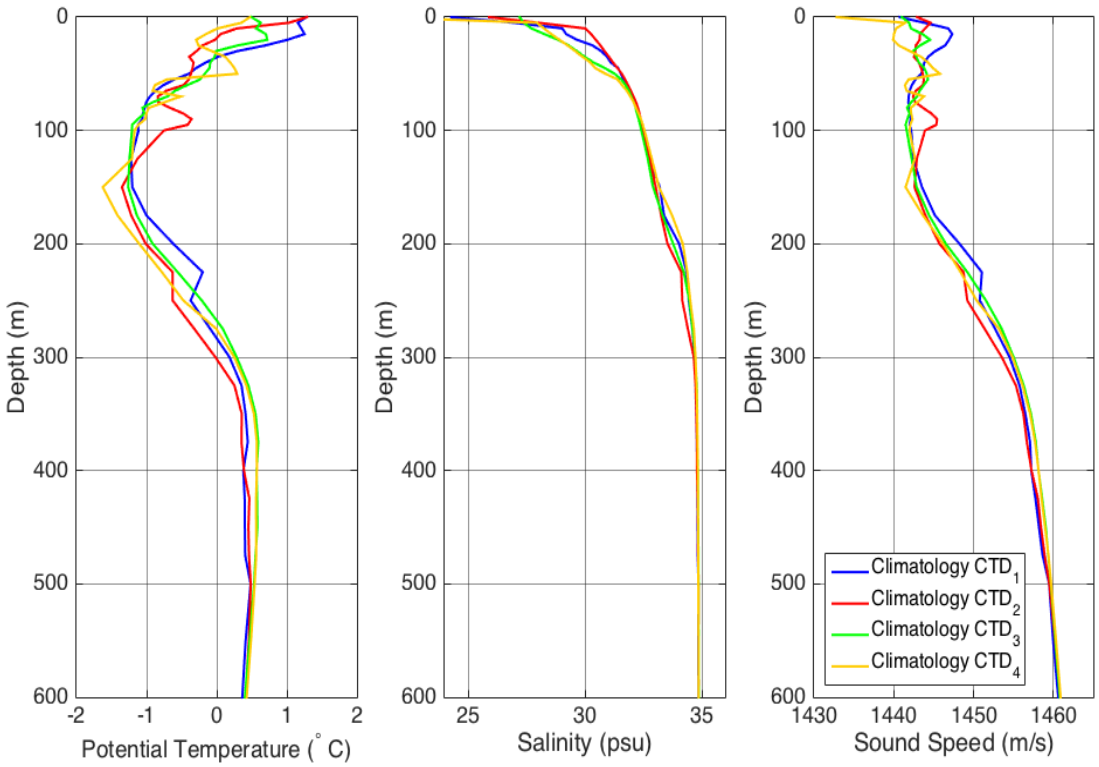

Figure 26. Climatology near CTD Track

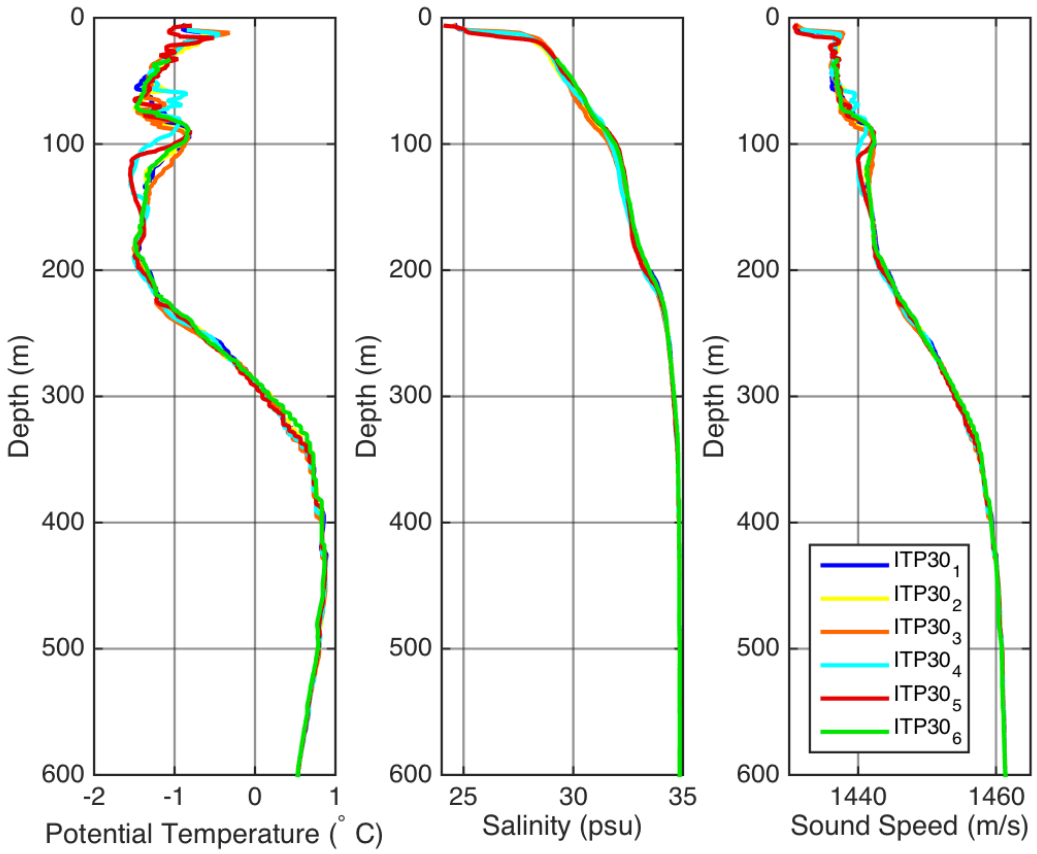

Figure 27. Climatology at ITP30

Figure 28 shows that there is a greater NSTM in the CTD002 than in the other profiles, which correspond to a greater sound speed. This difference could be due to the fact that the CTD profiles are collected in open water than in ice as opposed to the ITPs.

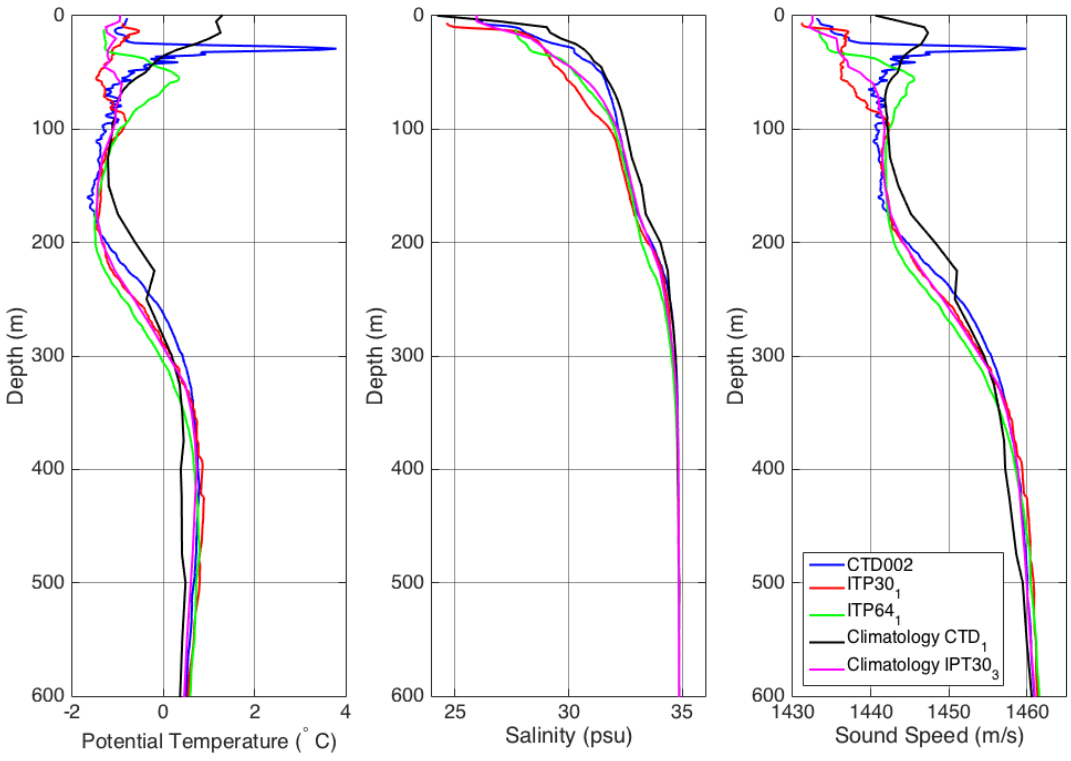

Figure 28. Potential Temperature, Salinity and Sound Speed versus Depth for Climatology for CTD and ITP30, and for CTD002, ITP30 and ITP64

IV. OCEANOGRAPHIC ANALYSIS AND RESULTS

This section of the thesis will detail the oceanographic analysis of the CANAPE data, and will be separated into the topics of internal waves and spice.

The data sets were processed in MATLAB using the Commonwealth Scientific and Industrial Research Organization (CSRIO) Sea Water Library package to obtain variables of interest that include potential temperature, salinity, sound speed, buoyancy frequency and potential sound speed gradient as a function of depth. These variables were then used for further analysis.

The displacement and spice analysis was conducted in collaboration with LCDR Dominic DiMaggio, USN. The techniques used to analyze isopycnal displacement and spicy sound-speed variability are similar to those used in Colosi et al. (2012) and Colosi et al. (2013). There is a further description in DiMaggio et al. (2016), which reports on the results of the CANAPE pilot study.

The DVLA dataset will be examined in relation to internal waves and spice, to determine the space/time scales of the sound speed structure. Spectral analysis will be utilized as a tool. The shipboard CTD data cannot be used for this task because of the limited temporal resolution.

A. INTERNAL WAVES

The internal wave analysis will be divided into two parts: depth statistics and spectral analysis.

1. Depth Statistics

Here we present the depth statistics of the observed vertical displacements, ζ, from the DVLA. The DVLA observations of T, S, and p were used to compute potential density as a function of time and depth. Contours of constant potential density (isopycnals) were then tracked giving depth as a function of potential density and time. The motion of the vertical displacement of isopycnal surfaces is caused by internal waves and eddies as discussed in Chapter II

Potential density (Talley et al. 2011) was computed for the depth range of the SBE instruments, 85–550m, referenced to the 300 decibar (db) level $\sigma_{300}(z(t),t)$. This reference is roughly halfway between the shallowest and deepest recordings on the DVLA. Depth linear-interpolation was then conducted to track 45 isopycnals, $z(t, \sigma_{300})$, between 1026.90 and 1029.36 kg/m^2 (Figure 29). Potential temperature, $\theta_{300}(t,\sigma_{300})$ and salinity $S_{300}(t,\sigma_{300})$ were calculated for each isopycnal. These parameters are used in these calculations, as it accounts for adiabatic temperature changes due to vertical displacements. A feature is evident at the end of the vertical displacement time series where the isopycnals are lifted, occurring for ~2 days imply the presence of an eddy. Data below 350m has slightly increased fluctuations and it is feasible that this data is distorted from use of the SBE non-pumped instruments. Smaller fluctuations are displayed in the time series above 350m, which appear to be in the inertial variability range. Spectral analysis discussed in the next subsection will determine the specific range. An unexplained pull-down event happened in the time series before year day 216. To eliminate contamination into our results analysis, data was taken from year day 216 onward.

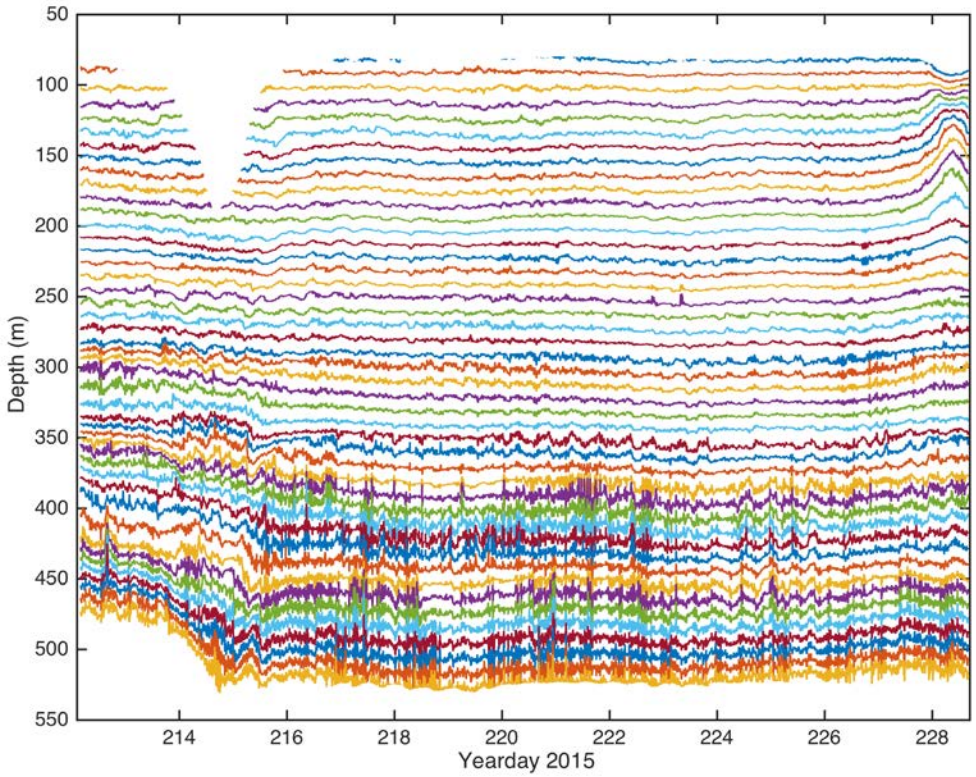

Figure 29. Depth of Tracked Isopycnals in the Upper 550 m at the DVLA Mooring. Source: DiMaggio et al. (2016).

To validate the linear interpolation, errors in isopycnal tracking were generated by recalculating the potential density from the computed $\theta_{300}(t,\sigma_{300})$ and $S_{300}(t,\sigma_{300})$. The RMS errors, which were the difference determined from both computed potential density were quiet small especially compared to other experiments conducted in more temperate regions such as the Philippine Sea (Colosi et al. 2013) and the New Jersey Continental Shelf (Colosi et al. 2012). This was expected due to the quiescent conditions in the Beaufort Sea. These RMS errors, plotted in Figure 30, are predominately small with the greatest variability in the depth between 200 and 300m. At this depth, thermohaline staircases on the order of 1m due to double diffusion are often found (Padman and Dillion 1987; Timmermans et al. 2008) which could account for this variability.

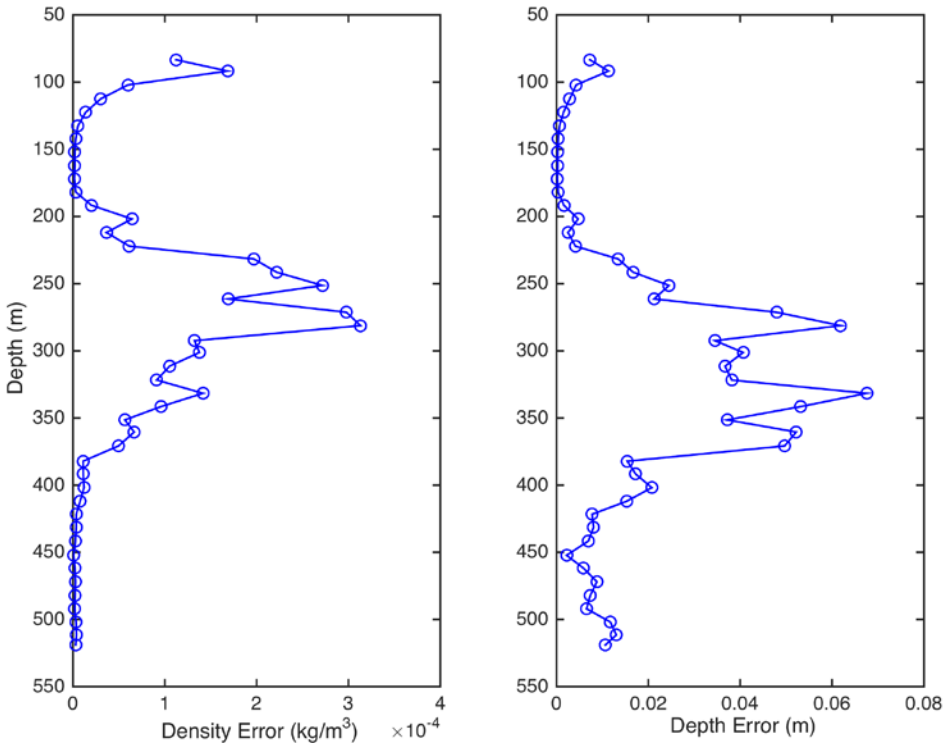

Figure 30. Root Mean Square Error in Tracking Isopycnal Density (Left) and Depth (Right). Source: DiMaggio et al. (2016).

Internal waves are an inhomogeneous phenomenon; therefore, the Wentzel-Kramers-Brillouin (WKB) depth scaling relation (Munk 1981) can be used as an approximate solution in the comparison of the RMS internal wave fluctuations. The WKB approximation is an approximate solution to cases where the waves propagating are gradually varying in the horizontal and time domain. The WKB depth scaling relation is represented by the equation

$$\langle \zeta^2 \rangle^{\frac{1}{2}} = \zeta_0 \sqrt{\frac{N_0}{N(z)}} \qquad (20)$$

where ζ_0 = 1.5 m (internal waves reference), N_0 = 3 cph, and where N(z) was calculated from the DVLA mooring data (see Figure 31). N(z) is the buoyancy frequency, it is discussed in Chapter II and plotted in Figure 16.

The WKB relation says that the rms displacement will be a function of depth. Moreover, this stipulates that N(z) is an important parameter in this study where (N^2 is shown in the next equation)

$$N^2(z) = g\rho^{-1}\frac{\partial \rho}{\partial z}. \qquad (21).$$

In Figure 31, the rms displacement is shown for the total isopycnal rms displacement (including internal waves and eddies) in green, isopycnal displacement for internal waves in the frequency band (f to N) in blue and the WKB approximation theory for internal waves in black. Here it can be seen that the observed internal waves RMS displacement fits well with the WKB approximation, however noting that the internal wave reference ζ_0 = 1.5 m is 20% of the standard Garret Munk (GM) value of ζ_0 = 7.3 m. This suggests that the internal wave energy observed is very low.

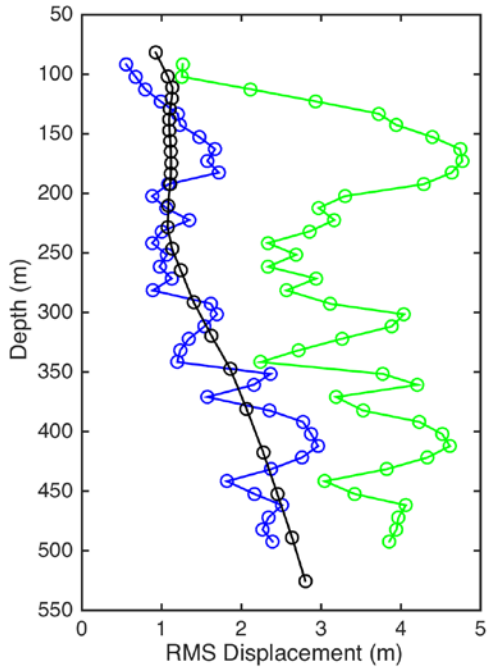

RMS displacement for all observed time scales including eddies is represented in green. Internal wave RMS displacements in the frequency band f to N are represented in blue, and the WBK approximation using a reference internal wave displacement ζ_0=1.5m represent in black.

Figure 31. Root Mean Square Displacement versus Depth.
Source: DiMaggio et al. (2016).

2. Spectral Analysis

Spectral analysis was performed to quantify the timescales of displacement variability, and to examine how this changes with depth. Examining the displacement frequency spectra is an effective way to study the space-time scales of sound speed variations (e.g., Equation (15)), and assists in determining dominant ocean processes affecting sound speed. Internal waves fall in the frequency band between N and f. Eddies are in the band greater than f. To remove high frequency noise which can be aliased into the spectra a low-pass 4-pole Butterworth digital filter was performed on the DVLA time series to eliminate signals with frequencies greater than 20cph (greater than N). Spectrograms for filtered isopycnals were then computed to provide power spectral density (PSD) estimates for each isopycnal as a function of depth (Figure 32).Three depth bands were considered for the depth-averaged PSD estimates. They were the shallow region (100-200m), mid region (200-400m) and deep region (400-500m). For all three bands, energy dissipates quickly for frequencies above the Brunt-Vaisala frequency. A significant spectral peak occurs at the inertial frequency where it overlaps with M2 tide. In the data between 3 to 40cpd (f and N), the power laws fit spectral slopes of p=-1.4±0.46 for 100–200m, p=-1.3±0.49 for 200–400m, and p= -1±0.59 for 400–500m. These slopes are flatter than the GM value of -2.0, inferring that the frequency spectra of displacement in the internal waves (super-inertial variability) frequency range is not consistent with GM. In the frequency range for eddies (sub-inertial variability), there is greater variability, however with lower energy than the peak at the inertial frequency. Furthermore, the deep region power law exhibits greater variability than the other two regions likely to be caused by instrument noise associated with the non-pumped sensors (DiMaggio et al. 2016).

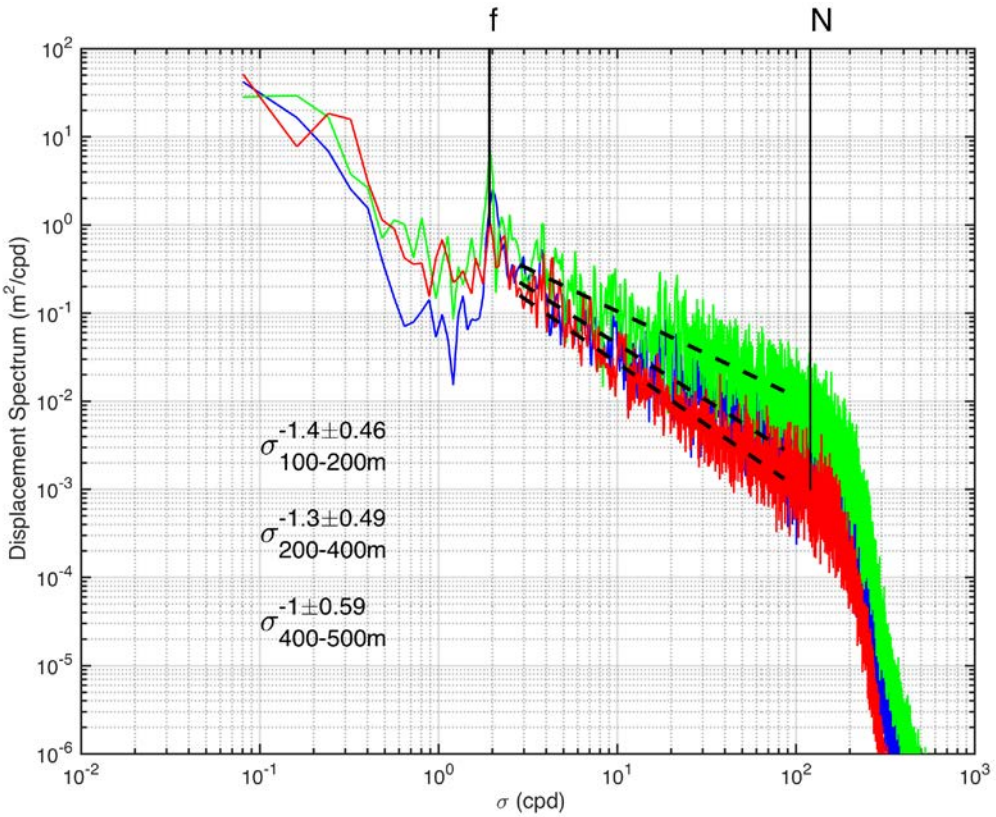

Frequency spectra of displacement. averaged in three depth bands: 100–200 m (red), 200–400 m (blue), and 400–500 m (green.) The Coriolis frequency, f, and typical buoyancy frequency, N, are indicated with solid vertical lines. A power-law fit to the random internal wave band of frequencies gives the exponents p=-1.4±0.46 for the depth band of 100–200m, p=-1.3±0.49 for 200–400m, and p=-1±0.59 for 400–500m

Figure 32. Frequency Spectra of Displacement. Source: DiMaggio et al. (2016).

B. SPICE

Fluctuations in sound-speed structure along isopycnals; specifically caused by density compensated temperature and salinity anomalies is called spice (Dzieciuch et al., 2004).

1. Depth Statistics.

Spicy sound speed structure was computed by tracking T and S variability along the isopycnals discussed in the previous section. This analysis then gives sound speed fluctuation as a function time and of the mean depth of the isopycnals (Figure 33).

Sections in the upper 250m, on the sound speed fluctuations time series observed to have sound speed variations of over 1 m/s. The strongest sound speed fluctuations existed in the middle of time series in the upper 150m which appeared to last for two to three days, slumping and weakening in depth. For oceans in lower latitudes, especially those that do not have ice cover, are expected in the upper ocean to have larger spice variations generated by precipitation, evaporation, and wind-forced mixing (Colosi et al. 2013). In the higher latitudes, we expect the spice to not be as large due to the dampening on the previously mentioned processes due to ice cover, it was surprising from this time series that there was considerable spice.

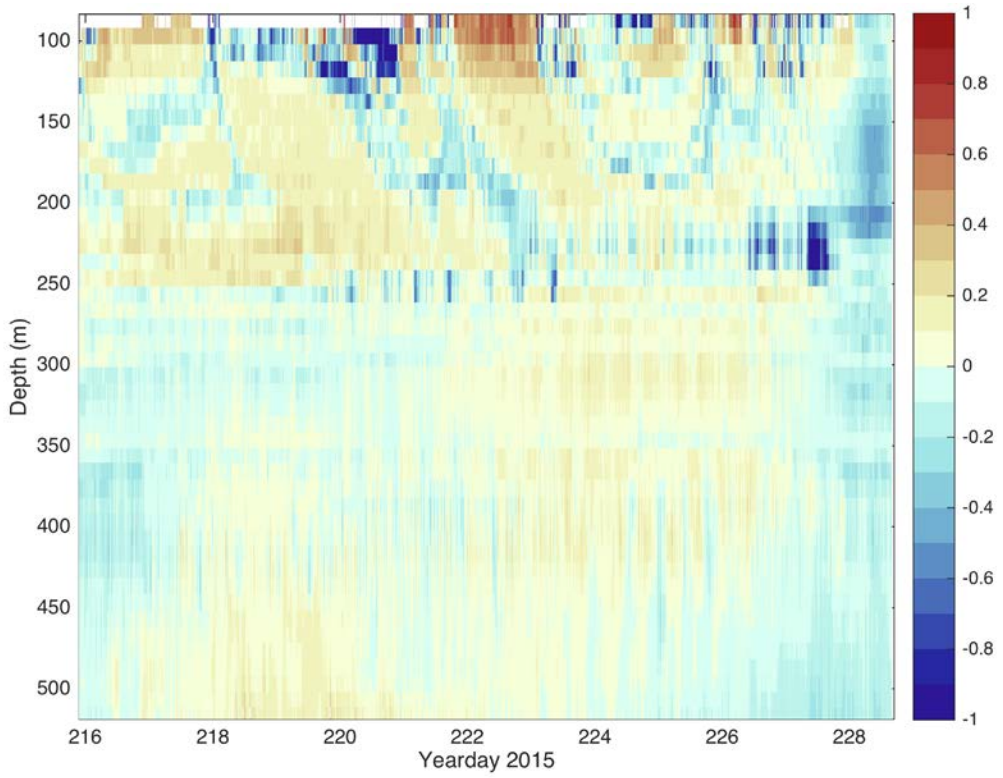

Figure 33. Depth-time Series of Isopycnal Sound Speed Anomalies Measured in m/s Measured at the DVLA Mooring.
Source: DiMaggio et al. (2016).

Sections in the upper 250m observed to have sound speed variations of over 1 m/s. The strongest sound speed fluctuation exist in the middle of the time series in the upper 150m and appears to last for three to four days with it weakening in depth.

From the spice observations sound speed variance was computed as a function of mean isopycnal depth. We have no model of spice so there is no WKB-like theory to compare to.

As was potential density calculated to track vertical displacement of isopycnals for internal waves, potential temperature, $\theta_{300}(t, \sigma_{300})$, and salinity, $S(t, \sigma_{300})$ were then calculated for each isopycnal, using linear interpolation, to track for variations along isopycnals for spice (DiMaggio et al. 2016).

Contributions to sound speed fluctuations due to spicy $\theta_{300}(t, \sigma_{300})$, $S(t, \sigma_{300})$ variations are computed by multiplying the RMS values of $\theta_{300}(t, \sigma_{300})$, $S(t, \sigma_{300})$ by the mean potential sound-speed gradient (Figure 34).

The total sound-speed fluctuations (green) in all frequencies have the greatest variation in the upper 150m with a second maximum between 200–250m. The spice in the internal wave band (f to N) (red) is dominant in the upper 200m and then has a similar shape and size to the spice contribution from the internal wave RMS displacement imposed by the potential sound speed gradient (blue) (Figure 34) in the 200 to 250m ranges. The larger values from the internal wave contribution (blue) between 250–450m may again be associated with the thermohaline staircases as mentioned in the internal wave displacement discussion.

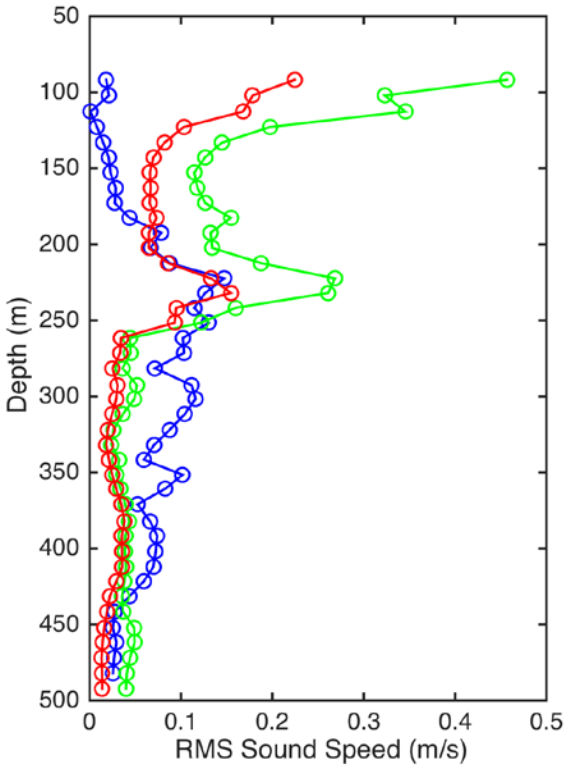

Total spice sound speed fluctuations from all frequencies are represented in green. Fluctuations due to spice in the internal wave band are represented in red, and fluctuations due to internal waves are in blue. The internal wave result is obtained by multiplying the RMS displacements in Figure 30 by the mean potential sound speed gradient in Figure ..

Figure 34. Root Mean Squared Sound Speed Fluctuations versus Depth. Source: DiMaggio et al. (2016).

2. Spectral Analysis

Spectrum analysis was performed to quantify the timescales of potential temperature and salinity variability and to examine how this changes with depth. Examining the frequency spectra of sound speed fluctuations with relation to density compensated temperature and salinity is another effective way to study the space-time scales of sound speed variations.

To quantify spicy $\theta_{300}(t, \sigma_{300})$, $S(t, \sigma_{300})$ and sound-speed variations along the isopycnals (spicy sound speed $c_s(t, \underline{z}, \sigma_{300})$, spectra of $\theta_{300}(t, \sigma_{300})$, $S(t, \sigma_{300})$ and sound

speed were integrated from f to N, to produce variances. Figure 35 shows sound speed spectrum over frequencies f and N.

As with isopycnal displacement, spectrograms for filtered spicy isopycnals were then computed to provide the average frequency spectrum of sound-speed fluctuation estimates for each spicy isopycnal as a function of depth, $\underline{z}(\sigma_{300})$.

Again, the spectrum was computed using depth average spectra with the same three bands where the power fit law was calculated for each region between the inertial and Brunt-Vaisala frequency (f and N). The power-law exponents were -1.4±0.46, -1.5±0.46 and -1.1±0.52 for 100–20m, 200–400m, and 400–550m respectively. The upper and mid region have slopes comparable to the GM slope of -2 for internal waves, ascertaining that spice time evolution is due to the passive advection of the structures by internal wave currents (Colosi 2013). The lower region is flatter and does not resemble the GM -2 slope, suggesting the lower frequencies are comparable to the higher frequencies. In the frequencies lower than f, there are traces that indicate phenomena such as eddies may contribute to spice as well.

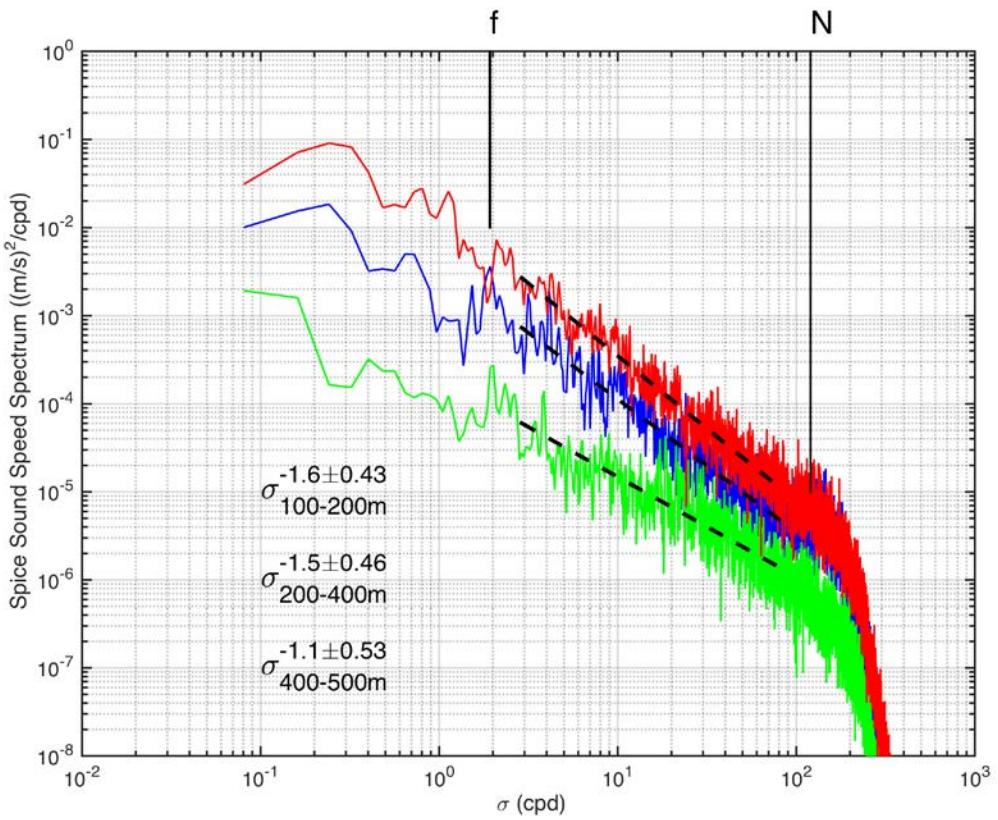

Averaged depth bands 100–200 m are represented in red, 200–400 m represented in blue, and 400–500 m represented in green. Power law fits to the spectra in the frequency range of 3 to 40 cpd are represented by dashed line. The Coriolis frequency, f, and a typical buoyancy frequency, N, are indicated for reference.

Figure 35. Frequency Spectra of Sound Speed Fluctuations Along Isopycnals (Spice) Averaged Over Depth Bands. Source: DiMaggio et al. (2016).

From this analysis for the period of July to August 2015, in the Beaufort Sea it can be determined that spice and the parameters associated with spice are large contributors to sound-speed. To identify the effects of the spicy sound speed fluctuations on acoustic propagation, acoustic modeling was performed and is discussed in the next chapter.

V. MODELING ANALYSIS AND RESULTS

This section of the thesis will detail the modeling analysis of the CANAPE CTD, ITP and climatology data sets.

A. ACOUSTIC PROPAGATION MODELING

The acoustic model used in this thesis is Bellhop. It is a Gaussian beam ray tracing program, and is part of the Acoustic Toolbox available on the Ocean Acoustic Library. The Gaussian beam method is an attempt to account for some diffraction. Bellhop is designed in order to perform two-dimensional acoustic ray tracing for a given sound-speed profile c(z) or a given sound-speed field c(r,z), in ocean waveguides with flat or variable absorbing boundaries (Rodríguez 2008). The output options include ray coordinates, travel time, amplitude, eigenrays, acoustic pressure and transmission loss. Transmission loss can be modeled using coherent, incoherent or semi-coherent parameters. The incoherent option was selected as it removes interference pattern evident due to phase and provides large-scale intensity structure. In Bellhop, the default approximation to calculate acoustic pressure is the geometric beams method; however, other approximations are available, namely beams with ray-centered coordinates, beams with Cartesian coordinates, and Gaussian beam bundles.

CANAPE CTD, ITP, and climatological sound-speed profiles will be used with Bellhop, for different acoustic frequencies and propagation ranges. Variability in transmission loss for the different profiles will be estimated from the Bellhop outputs.

This thesis will use the low to mid sonar frequency range (50Hz and 1kHz). Previous scientific experiments investigating under-ice acoustics used frequencies in this range; including CANAPE Pilot study, which used 250Hz; and the Marginal Ice Zone (MIZ) program conducted by Operational Naval Research (ONR) in 2014, which transmitted navigation signals with a center frequency of 900 Hz (Worcester, et al. 2014). In addition, the U.S. Navy operates sonar for their ship and submarines at low and mid-frequency. The “mid-frequency active sonar (1kHz-10kHz) is the Navy’s primary tactical sonar” (U.S. Department of Justice, 2015) carried aboard its cruisers, destroyers, frigates,

submarines, helicopters, and aircraft. The low-frequency sonar is utilized to “improve its ability to detect ultra-quiet, potentially hostile submarines at longer ranges” (U.S. Department of Justice, 2015). For ease of analysis, three frequencies were selected: 50Hz, 250Hz, and 1kHz.

Etter (2001) states that there are five main technique to model underwater acoustic propagation including: Ray theory, Normal Mode, Multipath Expansion, Wavenumber Integration (WI) or fast field, and Parabolic Equation (PE). For low frequency, deep-water, range dependent acoustic modeling. Etter 2001 (Figure 36) suggests that Parabolic Equations are a better fit, as their modeling approach is more applicable (physically) than Ray Theory, which has limitations in its accuracy.

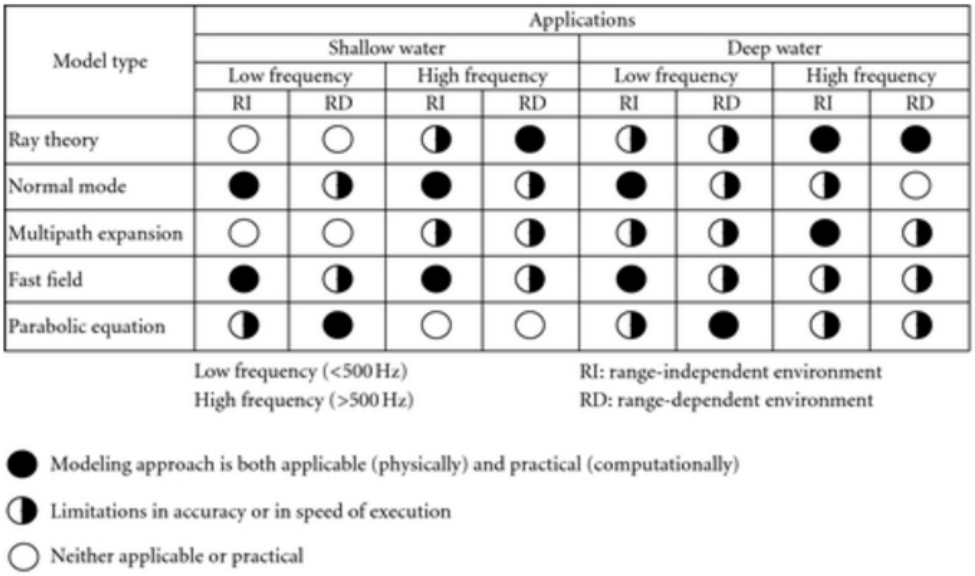

Figure 36. Domains of Applicability of Underwater Acoustic Propagation Models. Source: Etter (2001).

In this study, Ray Theory was considered adequate due to beam and ray methods being computationally fast propagation codes (Alexander et al., 2013) as well as the accessibility to a ray theory model such as Bellhop as it is open sourced. In this study, a large number of runs were expected with a transmission loss calculation executed for each CTD, ITP and climatology profile in the frequencies 50Hz, 250Hz, and 1kHz.

The major factor that influences attenuation of acoustic signals propagated in the Arctic Ocean is ice scattering, the interaction of sound waves with the rough sea ice cover. “The signal transmission loss increases rapidly with frequency” (Gavrilov et al. 2006).

For modeling acoustic propagation in a sea ice environment, two critical steps must be considered. These are modeling the ice as an elastic acoustic medium, and modeling the roughness of the ridging characteristics of the ice (Alexander et al., 2013). When using Bellhop the option of representing elastic properties is limited and only includes reduction in the coherent field on reflection (Alexander et al., 2013). The options for representing ridging include a statistically based method and a method using direct input of measured ice canopy data. Ice canopy measurements were not collected due to available resources for this study and therefore it was determined that the ice canopy was flat, and had a thickness of 2m as the measured temperature in the CTD dataset commenced at 2m.

In the Acoustic Toolbox used in this study, there is a statistically based method that uses Twersky’s boss scattering theory primarily for modeling under-ice scatter effects (Porter, 1997). For a detailed description on Twersky boss scattering, see Diachok (1976) and Porter (1997). Twersky boss scattering is used in the Bounce program of the Kraken part of the Acoustic Toolbox, which uses normal modes, and calculates a scattering coefficient. The Gaussian beam tracing method then uses this scattering coefficient to estimate ray trace and coherent transmission loss estimates of this environment (Alexander et al. 2013). In the data set, there were no altimetry data collected to determine scattering effects and therefore the ice canopy will be considered uniform. The ice acoustic properties used for Bellhop will include those approximated by Jensen et al., 2011 and described by Alexander et al. 2013. These parameters are: compressional speed 3500 m/s; shear speed 1800 m/s; density 890 kg/m^3; compressional attenuation 0.4 dB/λ_p; and sheer attenuation 1.0 dB/λ_S and a thickness of 2.0 m. Alexander et al., 2013 and Jensen et al. 2011 used a thickness of 2.7m.

1. Modeling Results CANAPE CTDs

To conduct a statistical analysis on the data set, the transmission loss pressure field was extracted from Bellhop for each CTD, ITP and climatology profile. The mean, standard deviation and anomaly were then computed for comparison so as not to lose the variability from each sound speed profile. Mean and standard deviation plots for each observational data set are shown in Figures 37–45.

The sound-speed variability spans up to 65m/s (Figure 20, 37a, 38a, and 39a, in the upper 100m for all frequencies investigated. A corresponding feature of increased transmission loss appears in the mean TL and standard deviation of TL of these plots for the higher frequencies 250Hz and 1kHz. This does not appear in the lower frequency due to the fact that higher frequencies have greater transmission loss due to propagation. Between depths 100m to 200m in the mid frequency (250Hz), there is a decrease in the mean TL and standard deviation compared to the other depth ranges There is little to no variation in this depth range, possibly contribution to the presence of the minimum sub-surface temperature (and sound speed) and the sub-surface duct associated with this minimum temperature. As mentioned in Chapter III, the sound-speed minimum is associated with the upper boundary of the PWW, and here it delineates the axis of the sound speed channel at ~120m where sound energy travels at greater distances.

For the 50Hz frequency in the mean TL plot and at the previously mentioned depth range, the influence of the sub-surface sound speed duct is also visible with lowered mean TL levels. Little variability in TL in the upper 300m is displayed again, indicating that at this low frequency, TL is less of a concern, especially in the sub-surface duct. As depth and range increase, TL also increases, suggesting rays may begin to scatter.

Below depths of 200m and for the higher frequencies (250H and 1kHz), TL increases in mean and variation. For deviation, the TL then decreases below depths of 500m. This mainly occurs in the lower PWW layer and upper Atlantic layer, below the sub-surface duct. At 250Hz, the greatest variability appears at the depths between 300m and 500m. The 300m depth defines the lower limit of the sub-surface duct, and at 500m,

sound speed becomes almost constant with depth. Moreover, there is an area of increased variability of 10m/s between the depths of 200m and 300m. Here at the lower region of the sub-surface duct in the 250Hz standard deviation TL plot there is slight variability in TL. Subsequently, the region close to the sub-surface duct is where the signal is focused, increasing signal strength.

In the highest frequency (1kHz), two distinct lines of increased deviation (up to 6dB) occur, one at 100m at the source depth, and one at 200m where the sound speed begins increasing with depth. A fainter line also exists where the maximum sound-speed occurs associated with the upper boundary of the PSW. At all depths and ranges greater than 200km, the mean TL increases considerably, possibly attributing to the effects of scattering.

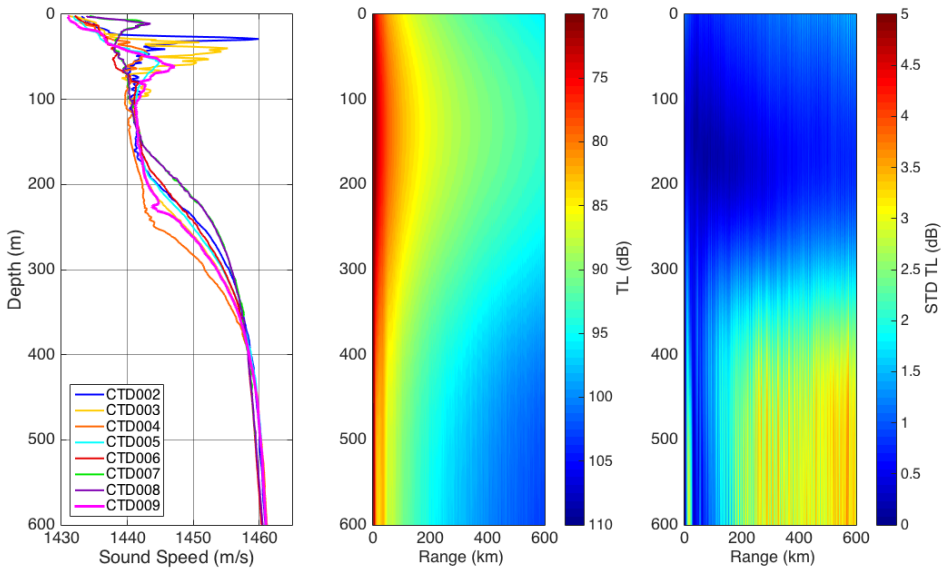

Figure 37. CTD Sound Speed Profile, Mean TL and Standard Deviation of TL for 50Hz

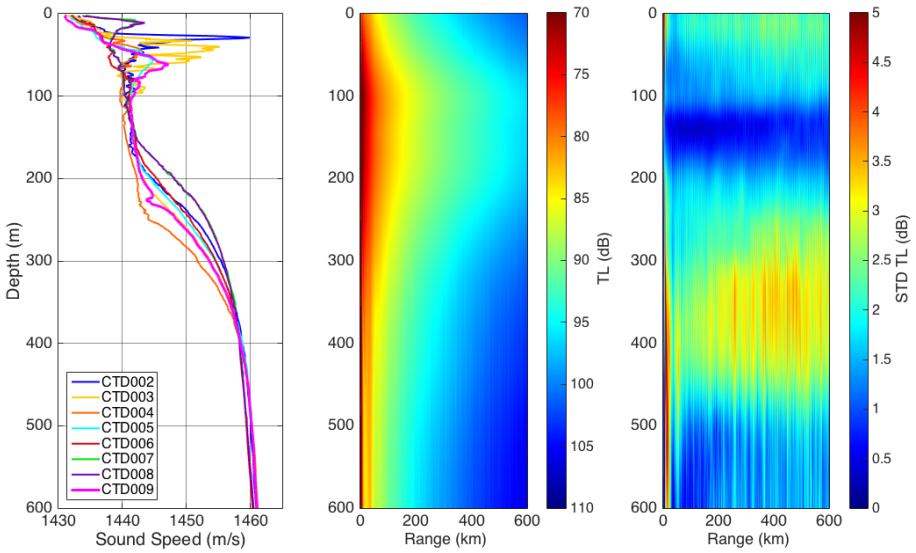

Figure 38. CTD Sound Speed Profile, Mean TL and Standard Deviation of TL for 250Hz

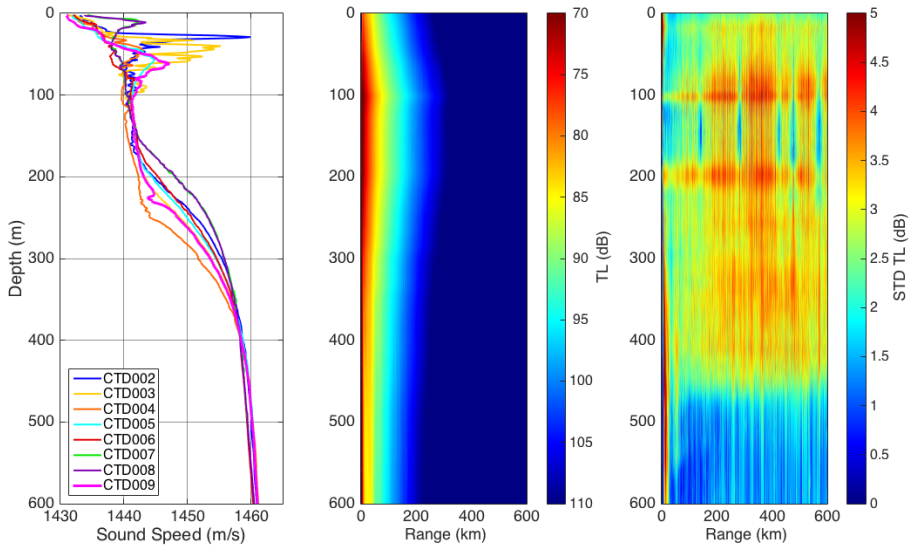

Figure 39. CTD Sound Speed Profile, Mean TL and Standard Deviation of TL for 1kHz

2. Modeling Results ITP30 and IPT64

For the ITP series, both ITP30 (Figures 40–42) and ITP64 (Figures 43–45) have smaller values of deviation, with ITP30 having the smallest. ITP64 has a similar shape to CTD data for all frequencies, which would be expected since they are in nearby locations. ITP64 again has the least amount of transmission loss near the source and in the range of the sub-surface duct, especially at the 50Hz frequency. Furthermore, the highest frequency has the greatest TL attributing to the TL and frequency relationship. For 50Hz in the standard deviation plot there is no more than a 1.5dB difference whereas for the difference increases to 2.5dB in the higher frequencies. A line of deviation appears in all frequencies measured with 1kHz sharper. Sound speed shows greater variability as well as an increase in amplitude at this depth. Furthermore, the sound source lies at this depth. In addition, a few faint lines are visible in the 1kHz frequency plot between 100m and 200m. A region of increased variability is also present between 200m and 400m at range greater than 400km as a result of TL in higher frequencies. The influence of the sub-surface duct decreases TL deviation in the 250Hz. The results show that mean TL increases as frequency increase. Moreover, in the two lower frequencies the influence of the sub-surface duct is evident due to the decrease in mean TL between depths 100m and 250m.

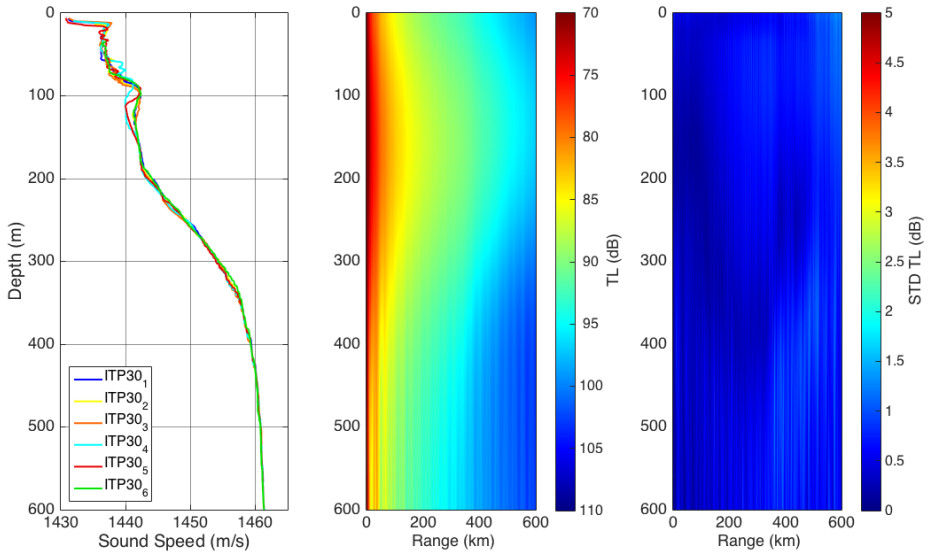

Figure 40. ITP30 Sound Speed Profile, Mean TL and Standard Deviation of TL for 50Hz

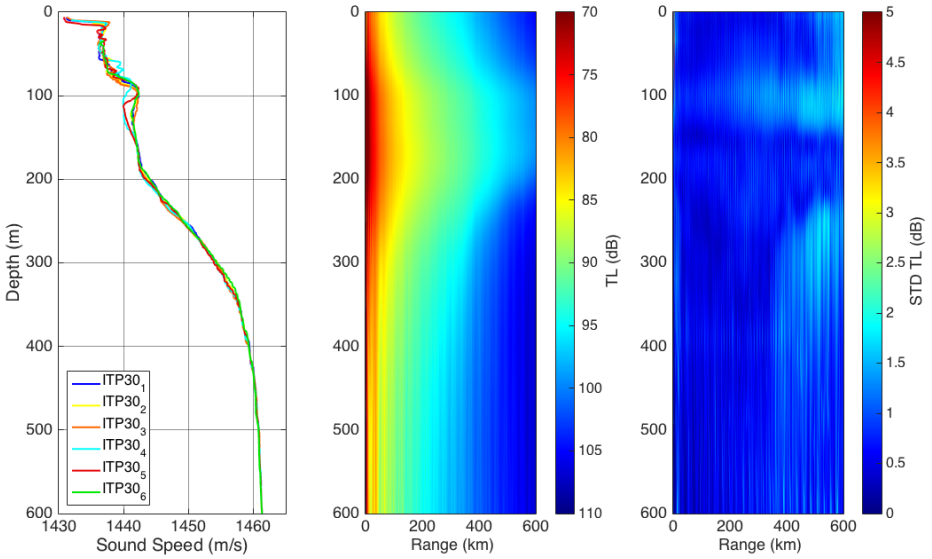

Figure 41. ITP30 Sound Speed Profile, Mean TL and Standard Deviation of TL for 250Hz

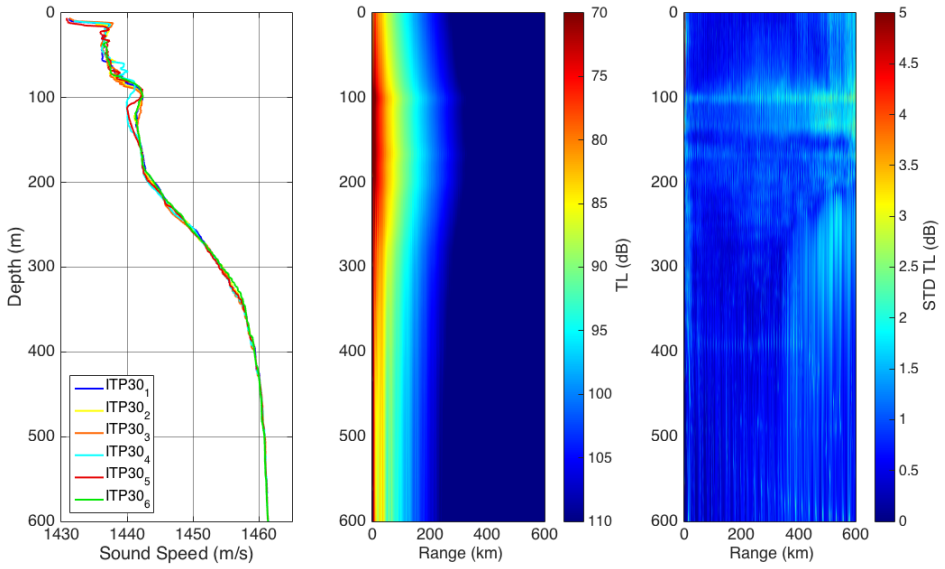

Figure 42. ITP30 Sound Speed Profile, Mean TL and Standard Deviation of TL for 1kHz

For the ITP30 plots (Figures 39–41) there is little to no variability at most ~2dB. A faint line of deviation appears at 100m at frequencies 250Hz and 1kHz. This faint line corresponds with the sound source depth and a local maximum in sound speed.

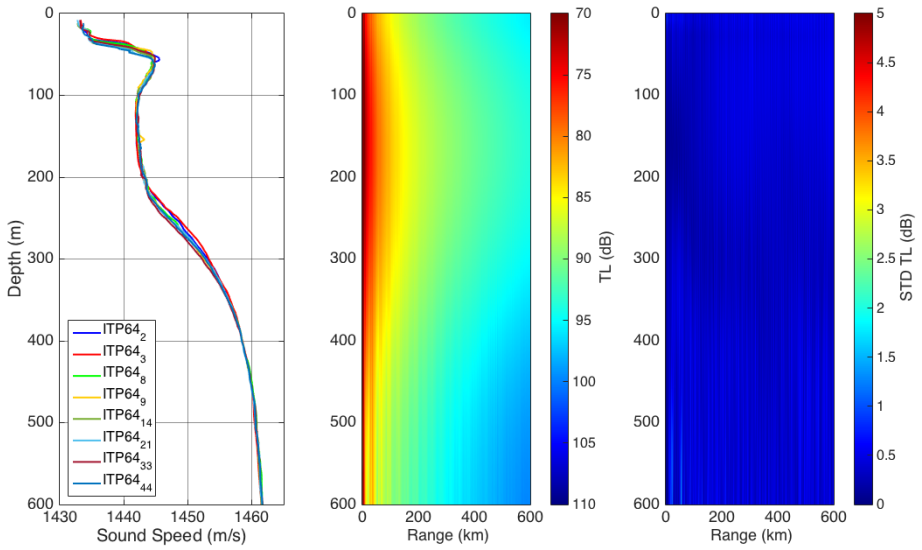

Figure 43. ITP64 Sound Speed Profile, Mean TL and Standard Deviation of TL for 50Hz

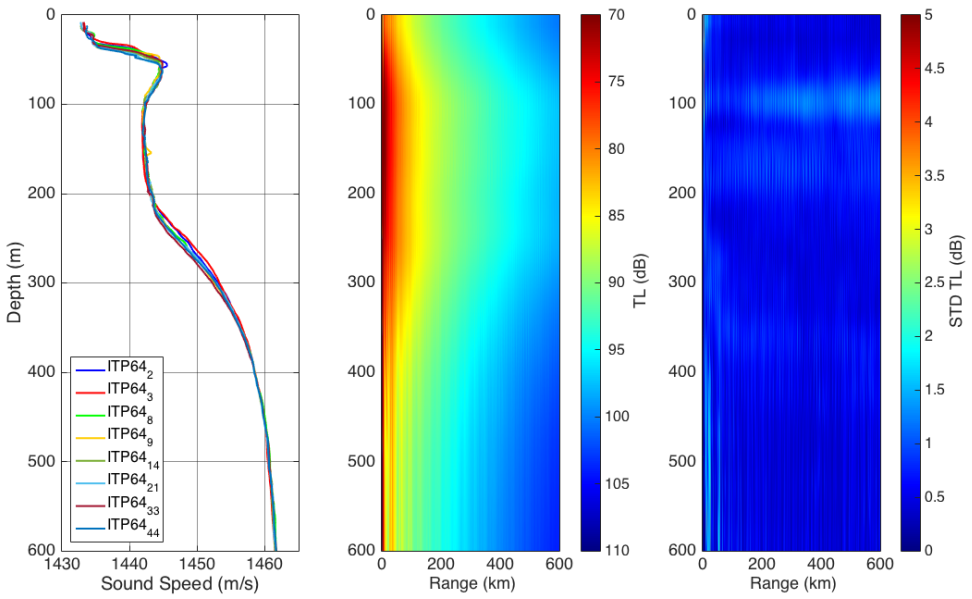

Figure 44. ITP64 Sound Speed Profile, Mean TL and Standard Deviation of TL for 250Hz

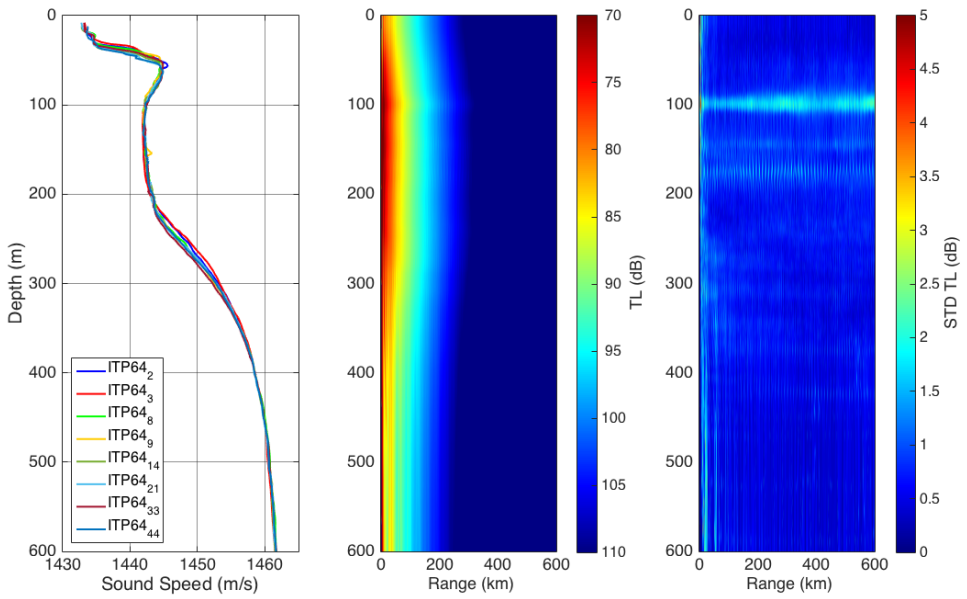

Figure 45. ITP64 Sound Speed Profile, Mean TL and Standard Deviation of TL for 1kHz

3. Comparisons to Climatology

In this section 'anomaly' is classified as the difference between the observational data sets (CTD, ITP30 and ITP64) and climatology, or the difference between observational data sets. To understand the extent to which the observational data sets have changed or varied from climatology an anomaly analysis was conducted. For this anomaly analysis climatology points near the CTDs and the ITPs were selected (as mentioned previously in Chapter III). The anomaly was calculated by subtracting the climatology data set from the climatology data set.

The anomalies at the higher frequencies (250Hz, 1kHz) for the CTD data set versus climatology (Figure 46) display a slight difference of 2dB with climatology having the greater transmission loss. As the frequency increases, the anomaly increases, particularly in the upper 100m, this possibility attributing to the TL and frequency relationship. Furthermore, a line of no change from climatology was present at the 100m depth (sound source depth) The anomalies for ITP64 data set and climatology above depths of 300m followed a similar shape to that of the anomalies between CTD data set

and climatology, but only smaller (~1dB less). Depths below 300m however, showed a slight increase in transmission loss for the CTD data set and a decrease in transmission loss for the ITP64 data set, when compared to climatology

In the 50Hz plot, very little difference from the climatology was apparent for the CTD with only small amounts of variability in the lower 300m (~2.5dB). For the ITP64 data set versus climatology, there was no variability in the lower 300m, where instead it appeared in the upper 300m (~2dB). All in all, the CTD data set had a greater transmission loss compared to climatology than the IPT64 data set.

The ITP30 data set anomalies when compared to climatology (Figure 48), had some interesting results. A large positive difference of up to ~8dB was present in ranges greater than 400km, likely attributing to higher TL in higher frequencies. The surprising result was that this feature was also prominent in the 50Hz plot. It is apparent that the ITP30 data had greater transmission loss than climatology. This data set could have had a very dynamical atmospheric or oceanographic system pass through the area during the recording of observations. Moreover, the climatology for this area could be different contributing to this significant variation.

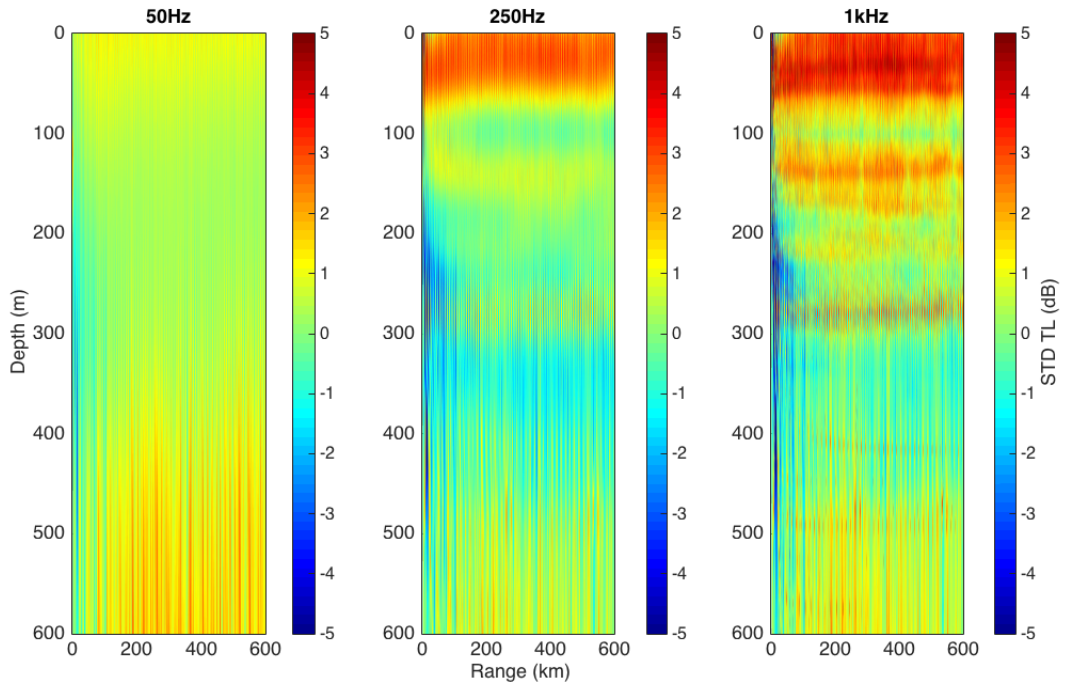

Figure 46. Anomaly of TL between Mean CTD and Climatology near CTD Points

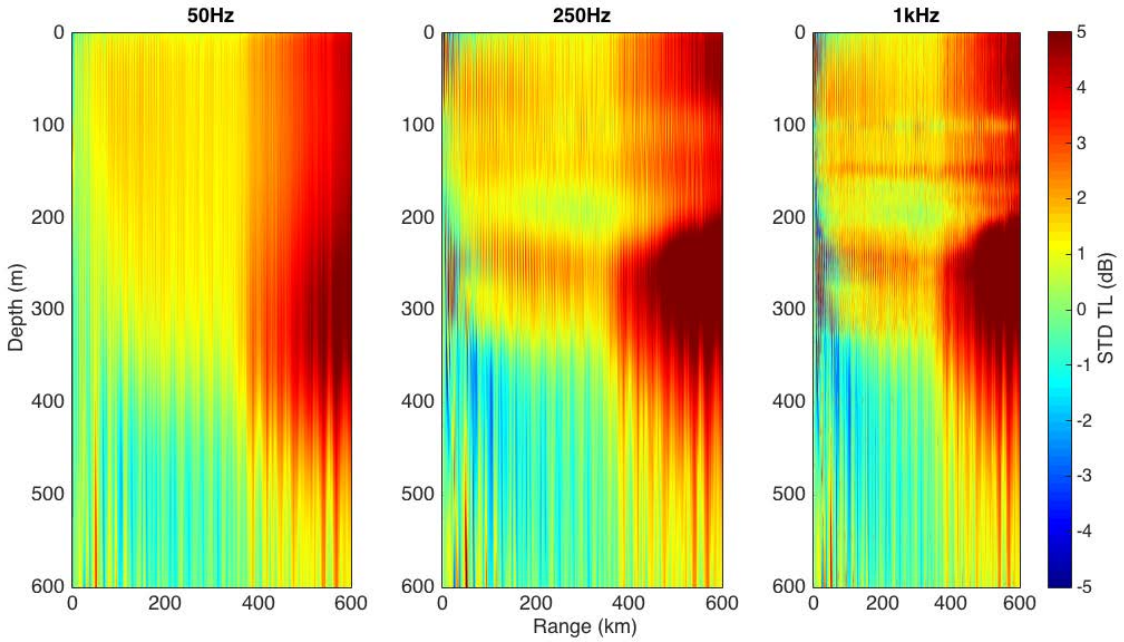

Figure 47. Anomaly of TL between Mean ITP30 and Climatology near ITP30 Points

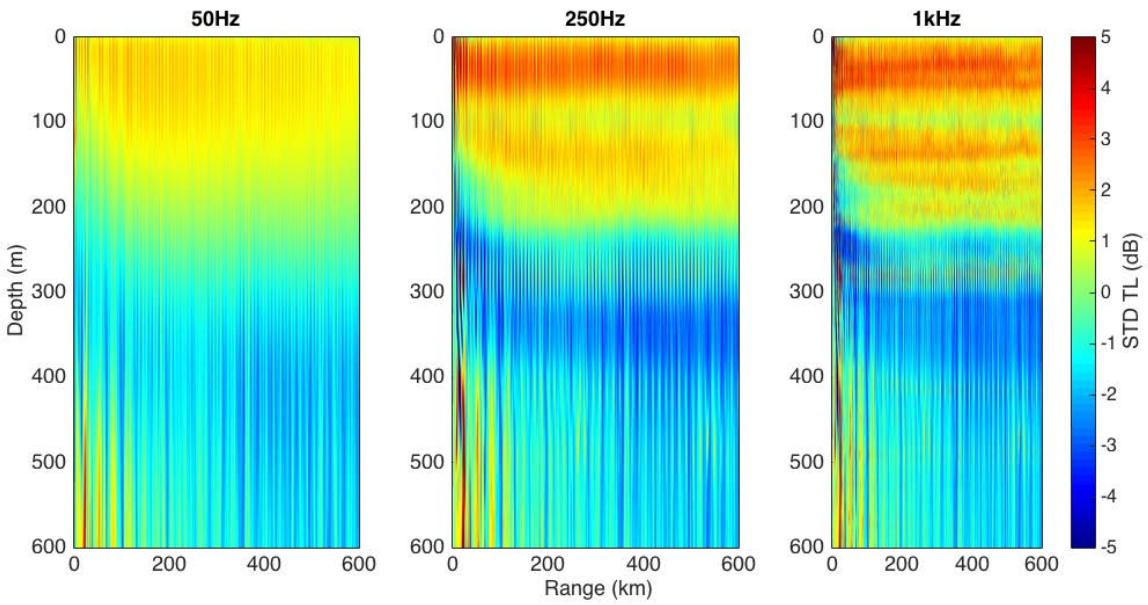

Figure 48. Anomaly of TL Between Mean ITP64 and Climatology Data near CTD and ITP64

To investigate any changes over the last few years, from 2012 when the ITP64 data set was recorded, and CTD data set in 2015, an anomaly plot was computed for the difference between the mean of the CTD and mean of the ITP64 observations (Figure 49).

The variability between the two data sets is mainly in the lower 300m. This variability ranges between 2-4dB, with the CTD data set being the greater of two. As frequency increases, a slight increase in the CTD TL is seen likely due to the TL and frequency relationship. No significant difference in the upper 300m is exhibited. This may be contributed to the fact that both sound speed profiles have a similar shape. The only obvious difference is that the CTD data set has a greater variation in the NSTM of up to 4°C and is located 10–20m closer to the surface.

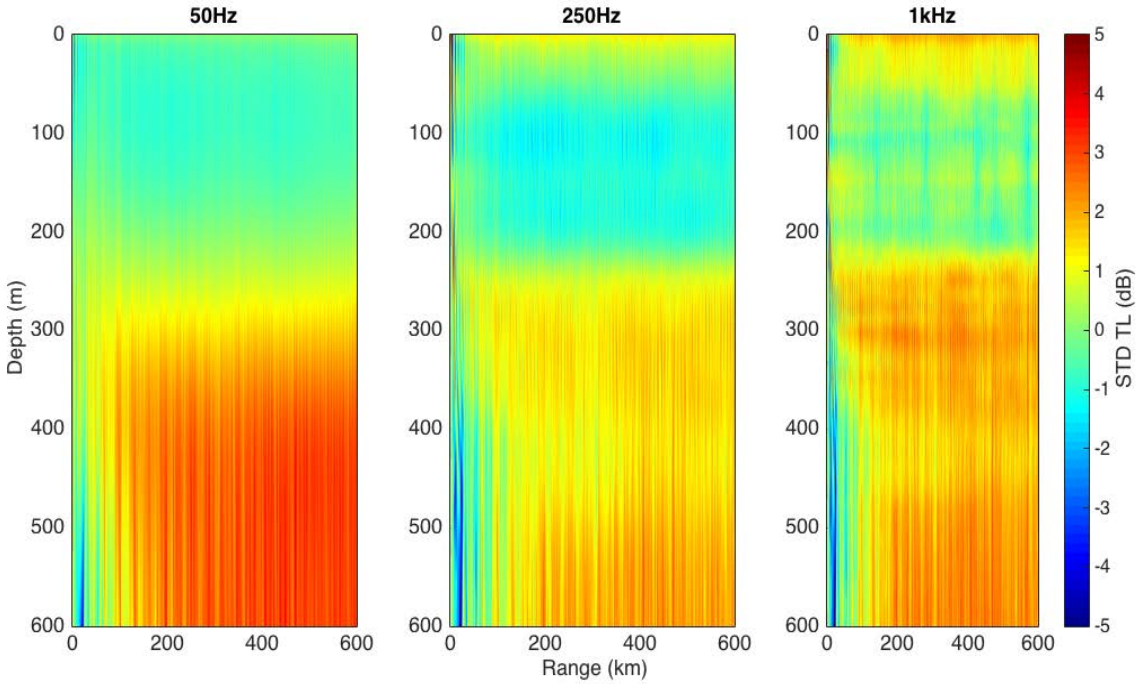

Figure 49. Anomaly of TL between Mean CTD and Mean ITP64.

To determine if it is the location of the ITP30 data that could the cause of the large differences, a comparison was made with the CTD data set (Figure 50) as well as between the two climatology data sets (Figure 51). It is apparent that the two observational data sets are quite different. Here it is shown that shape is similar to that in the comparison between ITP30 data set and climatology. The difference though is that ITP30 data set has a greater TL. This stipulates that it is in fact the ITP30 data set that is considerably different, not the climatology taken near ITP30. The assumption that can be made is that it was likely that the water column has changed compared to climatology or that a significant dynamic system was in the area during the time. Another possibility, is that climatology has been updated since this data set was taken in 2009.

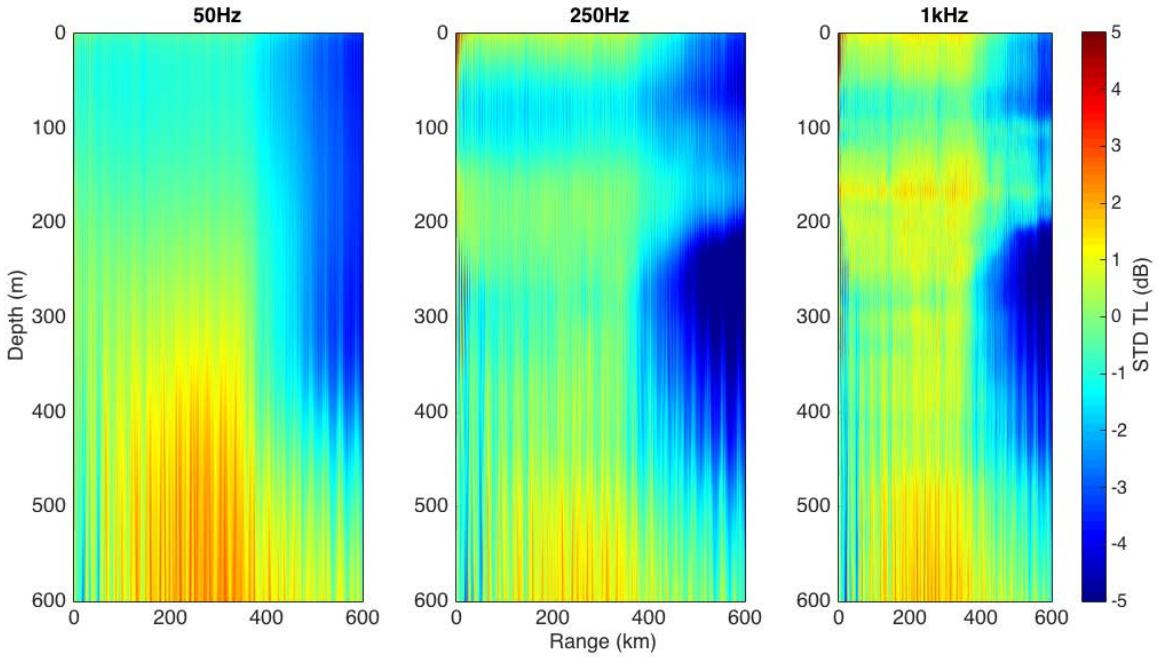

Figure 50. Anomaly of TL between Mean CTD and Mean ITP30 Data Sets

A comparison between the observational data sets and the climatology showed how present conditions have changed. To show the horizontal spatial change for the Beaufort Sea a standard deviation plot was performed for the two climatology data sets (Figure 50). Here it shows that most of the variability in the TL was in the lower 400m in the 50Hz plot. Also present are lines of variability in the 250Hz and 1kHz plot around 50m, 150m and 300m.The line in the 1kHz is sharper. At most the deviation was around 2dB, demonstrating small amplitudes of variation between the two climatological data sets. Form this plot and plots in Figures 47 and 49 it is deemed that the ITP30 data set is considerably different to the climatology and the other data sets. Due to this large difference, the analysis will continue with CTD, ITP64 and climatology only.

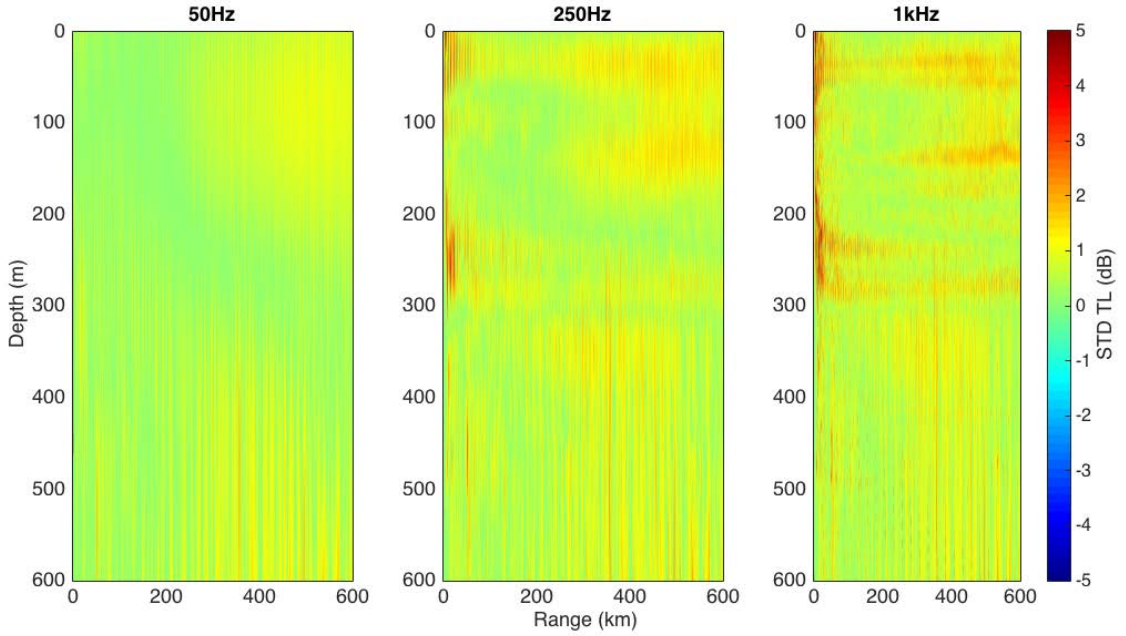

Figure 51. Standard Deviation of TL between Climatology Data near CTD and Climatology Data Near ITP30

The mean TL plots for each data set and each range, 50km, 100km, 200km and 600km (Figure 52–55) showed that for increasing frequency, variability increased. Furthermore, with increasing range TL increased. A feature present in all plots was that there was a decrease in TL in the depths that corresponded to the source depth and the sound channel. In addition, TL increases with increasing depth below the minimum sound-speed associated with the lower boundary of the PWW. In all plots, 1kHz frequency had the greater variability in the mean curve than all the other frequencies. ITP64 appeared to follow the same shape and amplitude to the climatology. CTD data in the 200km and 600km range had greater TL, while in the 50km and 100km range it was comparable climatology.

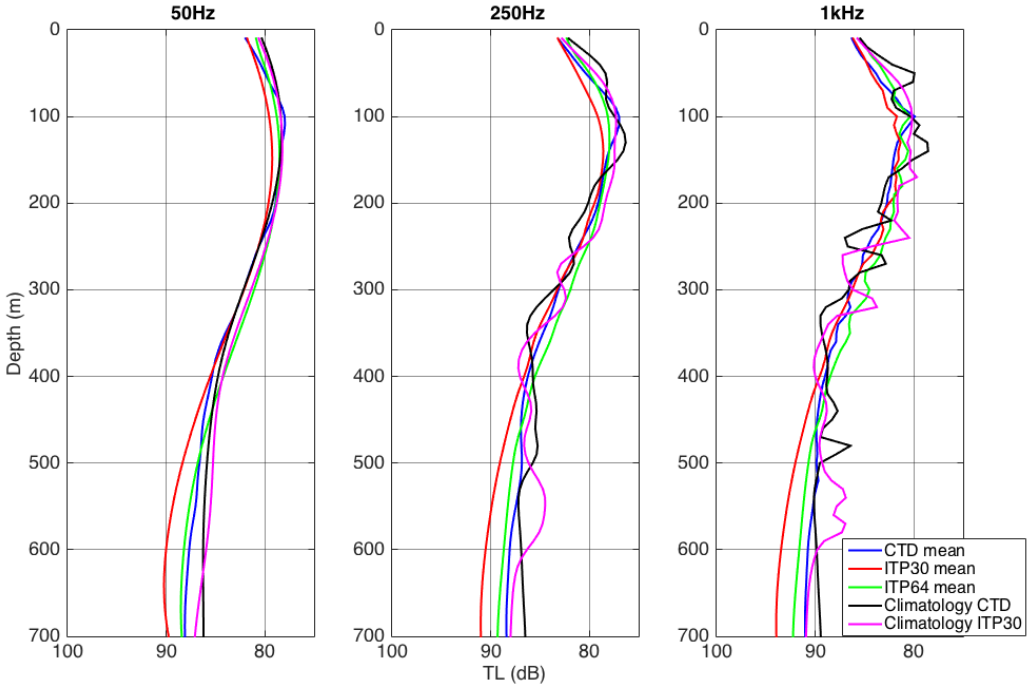

Mean TL of CTD profiles are represented in blue; mean TL of ITP30 profiles are represented in red; mean TL of ITP64 profiles are represented in green; TL of climatology near CTD points is represented in black; and TL of ITP30 climatology is represented in magenta.

Figure 52. Transmission Loss Mean of Data Sets at Range 50km from Source

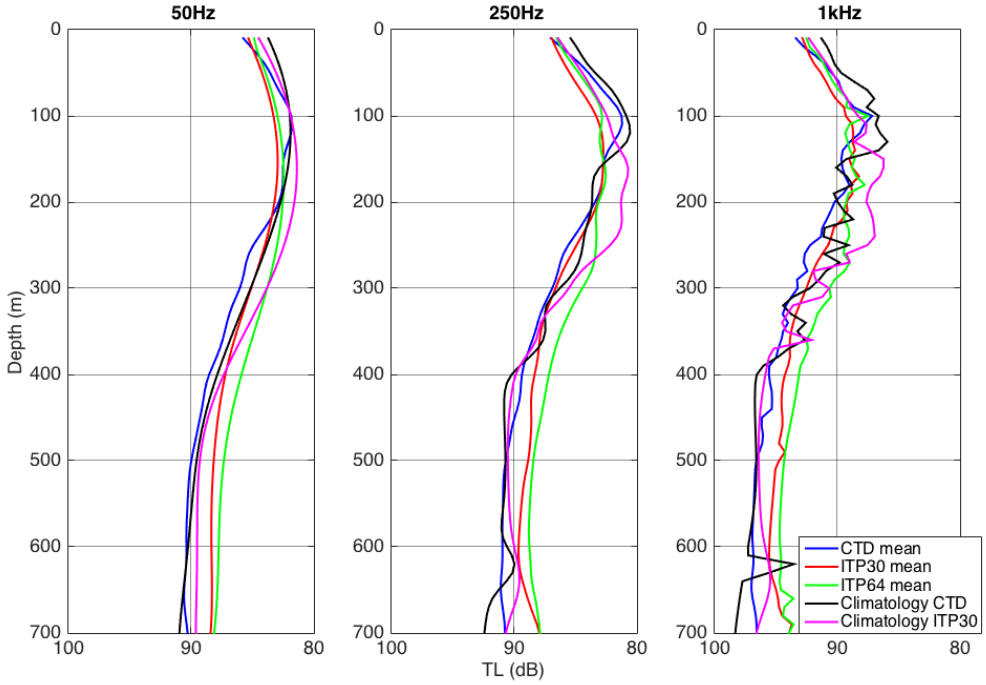

Mean TL of CTD profiles are represented in blue; mean TL of ITP30 profiles are represented in red; mean TL of ITP64 profiles are represented in green; TL of climatology near CTD points is represented in black; and TL of ITP30 climatology is represented in magenta.

Figure 53. Transmission Loss Mean of Data Sets at Range 100km from Source

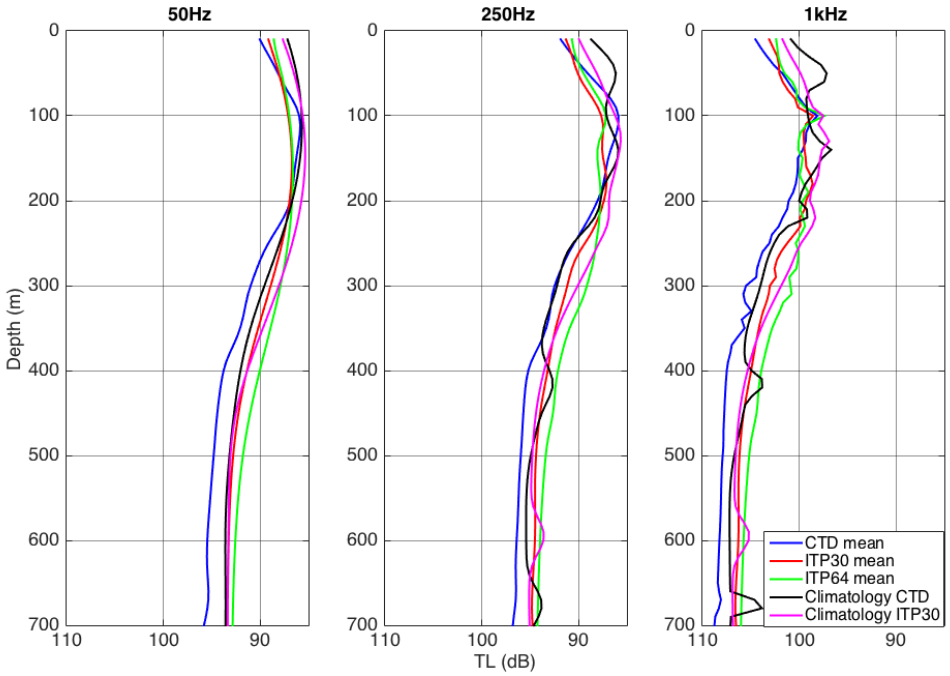

Mean TL of CTD profiles is represented in blue; mean TL of ITP30 profiles is represented in red; mean TL of ITP64 profiles is represented in green. TL of climatology near CTD points is represented in black, and TL of ITP30 climatology is represented in magenta.

Figure 54. Transmission Loss Mean of Data Sets at Range 200km from Source

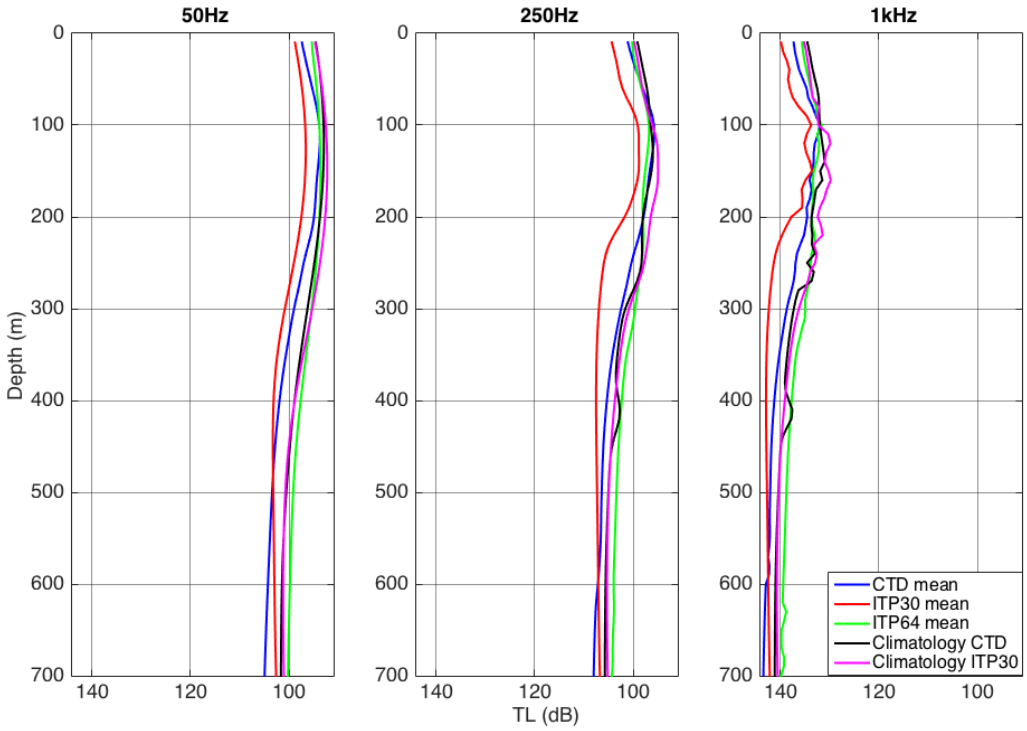

Mean TL of CTD profiles is represented in blue; mean TL of ITP30 profiles is represented in red; mean TL of ITP64 profiles is represented in green; TL of climatology near CTD points is represented in black; and TL of ITP30 climatology is represented in magenta.

Figure 55. Transmission Loss Mean of Data Sets at Range 600km from Source

THIS PAGE INTENTIONALLY LEFT BLANK

VI. DISCUSSION AND CONCLUSION

This thesis provided an analysis of the spatial and temporal variations of the thermohaline structure of the Canada Basin in the Western Arctic, and described how some of these features can affect acoustic propagation. It is clear that in recent decades, changes in the Arctic have reduced sea ice in the water column and transports between the Arctic, Pacific and Atlantic oceans. Using observational data collected from the CANAPE pilot study conducted in summer of 2015, the thermohaline sound speed structure was examined and an acoustic analysis was conducted.

The temporal variations of the thermohaline sound speed structure, observed by a mooring were examined by computing isopycnal displacements. Temporal structure of these processes was estimated using spectral analysis, separating internal waves and eddies from intrusive thermohaline structure, or spice. Vertical structure of these processes was examined by computing the rms variation of the various processes as a function of depth. Observations were compared to climatology. Acoustic propagation simulations used the ray-based model Bellhop to estimate the acoustic sensitivity to the observed the ocean structure, focusing on transmission loss as the parameter of interest.

It was found that in the temporal and vertical domain sound speed variations were influenced by the ocean processes of internal waves, eddies, and spicy thermohaline structure. The oceanography analysis showed that there was high variability in the upper 100m between the eight CTD sites and the 16-day time series of the DVLA. It was seen that variations of potential temperature and salinity influenced changes in the sound speed.

The vertical structure from the CTD data set showed that four distinct water masses were present, the surface layer, Pacific Summer Water, Pacific Winter Water and the Atlantic layer, with other distinct features being the NSTM, the summer halocline, winter halocline and the lower halocline.

In the DVLA analysis, internal waves were observed at a very low energy. This is seen in the displacement depth statistics indicating that the internal waves followed the

WKB approximation theory for internal waves, but with a lower energy. Internal wave energy was observed to be 20% of that typical for lower latitudes. Furthermore, in the displacement spectrum density analysis it was discovered that the observed spectral shape was not the same as the Garret Munk shape for internal waves. The displacement spectrum in the internal wave band from the inertial frequency (f) to buoyancy frequency (N), showed a more even distribution of energy between lower frequencies and higher frequencies.

It was discovered that spice dominated sound speed variability in the upper 150m and was surprisingly large in the experiment region. The spicy sound speed fluctuations also accounted for considerable sound speed variations in the upper 250m with sound speed anomalies over 1m/s. Below 300m the dominant contribution shifts to the internal wave RMS displacement imposed by the potential sound speed gradient. It is suggested that this may be an artifact of thermohaline staircases, which are a familiar feature in this depth region.

In the upper 400m, the spice spectrum was comparable to GM theory, supporting the idea that spice time evolution is due to the advection of passive spice structure by internal wave currents (Colosi 2013). It is also apparent in the spectrum analysis for both displacement and sound speed that internal waves were influencing phenomena. In addition, there were traces of energy in the eddy frequency range (less than f) suggesting their presence can impact both vertical displacement and sound speed. Of note, with predicted levels of sea ice expected to continue to reduce, and with the possible event of sea ice-free summers, the variability and the effects of spice and internal waves may increase, as the lack of ice cover will permit increased turbulence and mixing.

It was discovered that the CTD CANAPE data was more variable in temperature, salinity and sound speed when compared with climatology and recent ITP observations at locations near the CANAPE experiment. Climatology is a mean average and therefore variability is lost during the production of this data set. Furthermore, mesoscale features, such as those shown in the DVLA time series, are missing from climatology. Moreover, atmospheric data was not considered in this thesis, and therefore, dominant synoptic features were not taken into account. This may have provided for unexpected or more

than usual turbulence and mixing associated with wind forcing events, adding to the variability.

The acoustic analysis revealed that a greater variability in transmission loss in the CTD CANAPE data was evident compared to climatology and previous observations, particularly at greater frequencies and range. The presence of a sub-surface sound speed duct accommodated an environment with increased travel distance for acoustic energy and lower transmission loss for depths between 100–200m. The minimum temperature and associated minimum sound speed delineated the position of the sound duct axis (~120m), whereas the lower region of the PWW delineated the lower bound of the sound speed duct (250m). It was discovered that conditions within the sub-surface sound speed duct were stable, thus decreasing TL and increasing travel distance in sound signals in this region. Furthermore, investigations determined that the sub-surface sound speed duct decreased in effectiveness as the frequency increased. This demonstrated that high frequency is affected by propagation and therefore, low frequency is still the best option for acoustic applications.

The sound source at 100m could have also attributed to the results in the acoustic propagation being trapped in the sub-surface sound speed duct. There was little evidence to show that the upper refracting surface duct interacted with this sound energy originating from 100m. In the upper 100m as frequency increased, variability in transmission loss increased. In addition, transmission loss increased with increasing frequency below the sub-surface duct.

In the acoustic analysis, this greater variability was present when compared with the ITP64 data set recorded in 2012. In this comparison, the ITP64 data was 1–2db less in TL from the CTD. This difference in variability could be likely on the account that the ITPs are deployed in sea ice and not MIZ or open water, therefore reducing mixing and turbulence. This acoustical analysis suggests that the water column in the Beaufort Sea is changing and becoming more variable which is impacting on the sound speed and thus affecting the acoustic propagation.

These acoustic results are not exhaustive, and many assumptions need further analysis. There are limitations in using ray theory for acoustic modeling. It is computationally fast and simple; however, more complex theory such as normal mode theory and Parabolic Equation theory can provide a more accurate prediction. Transmission loss was the parameter being analyzed, and such ray theory was acceptable for this thesis. If more acoustic observables were to be explored, such as coherence, scintillation index, and phase/intensity spectra, then models that are more complex need to be utilized.

In conclusion, the comparison between observational data and climatology provided evidence that variability in the upper water column layers have increased. Monitoring and collection of observational data are crucial to understanding the changing effects of the variable thermohaline in the Canada Basin and how it affects acoustics. The current thin layer of sea ice in the Canada Basin will provide the preferable environment for increased signal travel. However, when will this limit be reached? Is it when the ice will be too thin to dampen the effects of wind on the ocean and render the Arctic Sound Channel ineffective?

VII. RECOMMENDATIONS FOR ONGOING RESEARCH

(1) Longer Data Series

The analysis in this thesis of the CANAPE pilot study was conducted over a short period, in July and August of 2015. A longer study, for example, that will be undertaken in summer 2016–2017 will provide further spatial and temporal results. It will enable for precise conclusions on phenomena investigated in this thesis as well as eddies, which are a longer-term feature. In addition, findings will be seasonal, and therefore, not be limited to a summer only analysis.

(2) Other Source Depths

The source depth of 100m was the only depth explored in this thesis. Other depths, especially those closer to the surface, will allow for further investigation into the environment resulting from the reduction in ice and changing transport of the Pacific and Atlantic waters. Placing a source in the upper 50m will provide the opportunity to understand the impacts of the changing water column on the Arctic surface half sound channel. With a source in the sub-surface sound duct, large amounts of acoustic energy are trapped and therefore do not reach the surface. Locating sound energy in the duct will support studies into sound energy interactions with the surface boundary. Furthermore, placing a sound source below the sub-surface sound duct will assist in investigating the behavior of sound energy at greater depths.

(3) More Sophisticated Modeling

This thesis used a ray theory acoustic model for transmission loss focusing only on incoherent profiles. For further analysis and realistic results, models that are more sophisticated should be considered. These models should attempt to include parameters such as ice roughness, ridging and scattering to provide an authentic solution for acoustic energy interacting with the surface boundary, it either being open water or sea ice. This can be accomplished by taking altimetry data for the sea-ice canopy and calculating a scattering coefficient to include in the programs code. Other parameters such as

attenuation, shear speeds, density of the medium could also be considered. Different scenarios such as range dependent examples can also be included.

(4) Compare with Observational Acoustic Data

Compare the observational acoustic data collected during the pilot study with modeled acoustic data. This would be of great interest to determine if the theory is representational of current acoustic conditions. Furthermore, it will provide data on process that the modeled data may have included and displayed.

(5) Compare with Regions in the Antarctic

The Arctic sea ice is still expected to reduce and is presently looking at becoming seasonal. Moreover, Antarctic sea ice is currently seasonal and a comparison of observational data to Antarctic and the Arctic may provide an indication how the Arctic may behave acoustically in the future. Similar procedures could be adopted as those used for comparing climatology in this thesis. Atmospheric and oceanography dynamics are different in these two polar regions, however, there are areas such as the Ross Sea that have similar circulation (Beaufort Gyre and Ross Gyre) as well as fresh water input from river runoff and glaciers that may provide similar water column samples, particularly if the study is only in the first 1000m.

(6) Temporal Acoustic Modeling

Investigate the ocean process that affects sound speed variations in an acoustic model. In this thesis, the acoustic analysis was conducted on all processes (and frequency bands) that affected sound speed. It would be of interest to conduct an analysis that separated components, particularly internal wave and spice. This can be done by inputting these processes into a scattering model and then inputting the results back into an acoustic model to study the transmission loss as well as any other parameters of interest.

LIST OF REFERENCES

ACIA, 2004: Impacts of a warming Arctic, Arctic Climate Impact Assessment. Cambridge University Press. Accessed 10 April 2016 [Available online at http://www.acia.uaf.edu/pages/scientific.html]

Alexander, P., A. Duncan, and N. Bose, 2012: Modelling sound propagation under ice using the Ocean Acoustics Library's Acoustic Toolbox. *Proceedings of Acoustics 2012*. Fremantle, Australia. Australian Acoustical Soc., 1–7. [Available online at https://www.acoustics.asn.au/conference_proceedings/AAS2012/papers/p5.pdf.]

Alexander, P., A. Duncan, N. Bose, and D. Smith, 2013: Modelling acoustic transmission loss due to sea ice cover, *Acoustics Australia*, **41**, 79–87.

Allen, R. L. Jr., and U.S. Navy; Naval Oceanographic Office. 2012: Global gridded physical profile data from the U.S. Navy's Generalized Digital Environmental Model (GDEM) product database (NODC Accession 9600094). Version 1.1. National Oceanographic Data Center, NOAA. Dataset. Accessed 24 May 2016 [Available online at http://nsidc.org/arcticseaicenews/charctic-interactive-sea-ice-graph/.]

Anthroff, D., R.J. Nicholls, R.S.J. Tol, and A.T. Vafeidis, 2006: Global and regional exposure to large rises in seal-level: A sensitivity analysis. Accessed 10 April 2016 [Available online at http://www.tyndall.ac.uk/sites/default/files/wp96_0.pdf.]

Barker, P.F, G.M. Filippelli, F. Florindo, E.E. Martin, H.D. Scher, 2007: Onset and role of the Antarctic Circumpolar Current. *Deep Sea Res., Part II*, **54**, 2388–2398, doi: 10.1016/J.DSR2.2007.07.028

Belkin, I.M., and A.L. Gordon, 1996: Southern Ocean fronts from the Greenwich Meridian to Tasmania. J. Geophys. Res., 101. doi: 10.1029/95JC02750

Boyer, T.P., O.K. Baranova, M. Biddle, D.R. Johnson, A.V. Mishonov, C. Paver, D. Seidov and M. Zweng 2012: Arctic regional climatology. Regional Climatology Team, NOAA/NODC Accessed 10 November 2015 [Available online at http://www.nodc.noaa.gov/OC5/regional_climate/arctic/]

Brix, H., and R. Gerdes, 2003: North Atlantic Deep Water and Antarctic Bottom Water: Their interaction and influence on the variability of the global ocean circulation. *J. Geophys. Res.*, **108**, 3022, doi: 10.1029/2002JC001335.

Colosi, J. A., T.F. Duda, T.T. Lin, J. Lynch, A. Newhall, and B.C. Cornuelle, 2012: Observations of sound speed fluctuations on the New Jersey continental shelf in the summer of 2006, *J. Acoust. Soc. Am.* 131(2), 1733–1748, doi: 10.1121/1.3666014.

Colosi, J.A., L.J. Van Uffelen, B.D Cornuelle, M.A. Dzieciuch, P.F. Worcester, B.D. Dushaw, and S.R. Ramp, 2013: Observations of sound-speed fluctuations in the western Philippine Sea in the spring of 2009. *J. Acoust. Soc. Am*, **134,** 3185–3200, doi: 10.1121/1.4818784.

Colosi, J.A, 2016: *Sound Propagation through the Stochastic Ocean*. Cambridge University Press, 424pp.

Department of the Navy and U.S. Coast Guard, 2007: A cooperative strategy for 21st century seapower, 20 pp, Accessed 10 February 2016. [Available online at https://www.ise.gov/sites/default/files/Maritime_Strategy.pdf.]

Diachok, O.I., Effects of sea-ice ridges on sound propagation in the Arctic Ocean. *J. Acoust. Soc.* **59**, 1110–1120, doi: 10.1121/1.380965.

DiMaggio, D., J.A. Colosi, A.N. Pearson, J.E. Joseph, M.A. Dzieciuch, and P. F. Worcester, 2016: Observations of thermohaline sound-speed structure in the Canada Basin marginal ice zone in the summer of 2015. In preparation.

Dzieciuch, M., W. Munk, and D.L. Rudnick, 2004: Propagation of sound through a spicy ocean, the SOFAR overture. *J. Acoust. Soc. Am*, **116,** 1447–1462, doi: 10.1121/1.1772397 .

Edwards, E.H., 2004: The SCICEX Program, Arctic Ocean investigations from U.S. Navy nuclear-powered submarine. Accessed on 10 February 2016 [Available http://www.nsf.gov/pubs/2005/nsf0521/nsf0521_5.pdf.]

Eger, K.M, Analyse and Strategic AS, 2011: Marine Traffic in the Arctic. Norwegian Mapping Authority. Accessed 15 December 2015. [Available online at http://www.iho.int/mtg_docs/rhc/ArHC/ArHC2/ARHC2-04C_Marine_Traffic_in_the_Arctic_2011.pdf.]

Encyclopedia Britannica, 2016: Arctic Ocean: Topography of the ocean floor. Accessed 28 April 2016. [Available online at http://www.britannica.com/place/Arctic-Ocean/Topography-of-the-ocean-floor#ref518833.]

Garret, C., and W. Munk, 1979: Internal waves in the ocean. *Annual Review of Fluid Mechanics*, 11, 339–369. doi: 10.1146/annurev.fl.11.010179.00201.

Gavrilov, A.N., and P.N. Mikhalevsky, 2006: Low-frequency acoustic propagation loss in the Arctic Ocean: results of the Arctic climate observations using underwater sound experiment. *J. Acoust. Soc. Am*, **119**, 3694–3706, doi: 10.1121/1.2195255.

Geology.com, 2016: Arctic Ocean seafloor features map, Geoscience New and Information. Accessed 28 April 2016. [Available online at http://geology.com/articles/arctic-ocean-features/.]

Hansen, O., P. Gronsedt, C.L. Graversen, C. Hendriksen, 2016: Arctic shipping – Commercial opportunities and challenges. CBS Maritime, 94 pp, [Available online at http://climateobserver.org/wp-content/uploads/2016/02/Arctic-Shipping-Commercial-Opportunities-and-Challenges.pdf.]

Holland, M., 2016: Variability in Arctic Sea ice: Causes and effects. Accessed 12 May 2016 [Available online at http://www.asp.ucar.edu/colloquium/2000/Lectures/holland.html.]

IBCAO, 2012: IBCAO Version 3.0, created June 8, 2012. Accessed 28 April 2016. [Available online at http://www.ngdc.noaa.gov/mgg/bathymetry/arctic/maps/version3_0/Ver3_Map_LetterSize_round.pdf]

IPCC, 2014: Climate change 2014: Synthesis Report. Contribution of working groups I, II and III to the fifth assessment report of the Intergovernmental Panel on Climate Change [Core Writing Team, R.K. Pachauri and L.A. Meyer (eds.)]. IPCC, Geneva, Switzerland, 151 pp.

Jackett, D.R., T.J. McDougall, 1997: A neutral density variable for the world's oceans. *J. Phys. Oceanogr.*, **27**, 237–26, doi:10.1175/1520-0485.

Jackson, J. M., E. C. Carmack, F. A. McLaughlin, S. E. Allen, and R. G. Ingram, 2010: Identification, characterization, and change of the near‐surface temperature maximum in the Canada Basin, 1993–2008, *J. Geophys. Res.*, **115**, C05021, doi:10.1029/2009JC005265.

Jensen, F.B., W.A. Kuperman, M.B. Porter and H. Schmidt,2011: *Computational Ocean Acoustics*. Springer, London, 794 pp.

Krishfield, R., J. Toole, A. Proshutinsky, and M. -L. Timmermans, 2008: Automated ice-tethered profilers for seawater observations under pack ice in all seasons, *J. Atmos. Ocean. Technol.*, **25**, 2091–2095, doi:10.1175/2008JTECHO587.1.

Lurton, X., 2010: *An Introduction to Underwater Acoustics: Principles and Applications*. Springer-Verlag Berlin Heidelberg, pp724.

Maslowki, W., J.C. Kinney, M. Higgins, and A. Roberts, 2012: The Future Arctic Sea Ice. *Annu. Rev. Earth Planet. Sci,*. **40,** 625–54 . doi: 10.1146/annurev-earth-042711-105345.

Massonnet, F., T. Fichefet, H. Goosse, C.M Bitz, G. Philippon-Berthier, M. M. Holland, and P.-Y. Barriat, 2012: Constraining projections of summer Arctic sea ice. *The Cryophere*, **6**, 1383–1394, doi:10.5194/tc-6-1383/2012.

Medwin, H. 1975: Speed of Sound In Water: A Simple Equation for Realistic Parameters. *J. Acoust. Soc. Am.*, **58(6)**, 1318–1319, doi:10.1121/1.380790 .

McLaughlin, F., E. Carmack, A. Proshutinsky, R.A. Krishfield, C. Guay, M. Yamamoto-Kawai, J.M. Jackson, and B. Williams. 2011. The rapid response of the Canada Basin to climate forcing: From bellwether to alarm bells. *Oceanography* **24(3)**, 146–159, doi:10.5670/ oceanog.2011.66.

Mikhalevsky, P.N. and A.N. Gavrilow, 2001: Acoustic thermometry in the Arctic Ocean. *Polar Res*., 20(2), 185–192, doi: 10.1111/j.1751-8369.2001.tb00055.x

Mikhalevsky, P.N., A.N. Gavrilow, and A.B. Baggeroer, 1999: The Transarctic acoustic propagation experiment and climate monitoring in the Arctic. *IEEE J. Oceanic Eng.*, **24**, 183–201, doi: 10.1109/48.757270

Morozov E.G., A.N. Demidov, R.Y. Tarakanov, W. Zenk, 2010: *Abyssal Channels in the Atlantic Ocean*, Springer Science Business Media B.V. DOI 10.1007/978-90-481-9358-5_2, pp25–50

Muench, R. D., L. Padman, A. L. Gordon, and A. Orsi, 2009: A dense shelf outflow from the Ross Sea, Antarctica: Mixing and the contribution of tides, *J. Mar. Syst*., **77**, 369–387, doi:10.1016/j.jmarsys.2008.11.003.

Munk, W., 1981: Internal waves and small scale processes, *The Evolution of Physical Oceanography*, B. Warren and C. Wunsch, MIT, Cambridge Press, 264–291.

National Instruments, 2015: Introduction to RF & wireless communications systems. Accessed 30 Apr 2016. [Available online at http://www.ni.com/tutorial/3541/en./]

NESTA, 2011: Melting sea ice and ocean circulation. UCAR. Accessed 12 Apr 2016. [Available online at http://scied.ucar.edu/longcontent/melting-arctic-sea-ice-and-ocean-circulation.]

NOAA, 2016: April 2016 El Niño/La Niña update: What goes up… Accessed 26 Apr 2016 [Available online at https://www.climate.gov/news-features/blogs/enso/april-2016-el-niñola-niña-update-what-goes-…]

NOAA, 2016b: Global gridded physical profile data from the U.S. Navy's Generalized Digital Environmental Model (GDEM) product database (NODC Accession 9600094). Accessed 24 May 2016. [Available online at http://data.nodc.noaa.gov/cgi-bin/iso?id=gov.noaa.nodc:9600094.]

NSIDC, 2013: Arctic sea ice news and analysis: Annual maximum extent reached. Accessed 15 December 2015. [Available online at http://nsidc.org/arcticseaicenews/tag/arctic-sea-ice/.]

NSIDC, 2015: Arctic sea ice news and analysis: 2015 melt season in review. Accessed 16 Dec 2015. [Available online at http://nsidc.org/arcticseaicenews/2015/10/2015-melt-season-in-review/]

NSIDC, 2016: Arctic sea ice news and analysis: March ends a most interesting winter. Accessed 26 Apr 2016. [Available online at https://nsidc.org/arcticseaicenews/2016/04/march-ends-a-most-interesting-winter/.]

NSIDC, 2016b: All about sea ice: Arctic vs Antarctic. Accessed 26 Apr 2016. [Available online at https://nsidc.org/cryosphere/seaice/characteristics/difference.html]

Oris, A.H., T. Whitworth III, W. Nowlin W, 1995: On the meridional extent and fronts of the Antarctic Circumpolar Current. *Deep-Sea Res.*, **42**, 641–673, doi:10.1016/0967-0637(95)00021-W.

Oris, A.H., G.C. Johnson, and J.L. Bullister, 1999: Circulation, mixing, and production of Antarctic Bottom Water, *Prog. Oceanogr.*, **43,** 55–109, doi: 10.1016/S0079-6611(99)00004-X.

Orsi, A.H., Jacobs, S.S., Gordon, A.L., Visbeck, M., 2001: Cooling and ventilating the abyssal ocean. *Geophys. Res. Lett.,* **28**, 2923–2926. doi: 10.1029/2001GL012830.

Orsi, A. H., W. M. Smethie, and J. B. Bullister, 2002: On the total input of Antarctic waters to the deep ocean: A preliminary estimate from chloro- fluorocarbon measurements, *J. Geophys. Res.,* **107,** 3122, doi:10.1029/2001JC000976.

Overland, J.E. and M. Wang, 2013: When will the summer Arctic be nearly sea ice free? *Geophys. Res. Lett.*, **40**, 2097–2101, doi:10.1002/grl.50316.

Padman, L., and T. M. Dillon, 1987: Vertical heat fluxes through the Beaufort Sea thermohaline staircase. *J. Geophys. Res.*, **92**, 10799–10806, doi:10.1029/JC092iC10p10799.

Peralta-Ferriz, C., R.A. Woodgate, 2015: Seasonal and interannual variability of pan-Arctic surface mixed layer properties from 1979 to 2012 from hydrographic data, and the dominance of stratification for multiyear mixed layer depth shoaling. *Prog. Oceanogr.*, **134(2015)**, 19–53, doi:10.1016/j.pocean.2014.12.005.

Pierce, A.D., 1989: Acoustics: *An Introduction to Its Physical Principles and Applications*, Acoustical Society of America, 678 pp.

Pisareva, .N., R.S. Pickart, M.A. Spall, C. Nobre, D. J. Torres, G.W.K. Moore, and T.E. Whitledge, 2015: Flow of pacific water in the western Chukchi Sea: Results from the 2009 RUSALCA expedition. Deep-Sea Res., Part I, 105, 53–73, doi: 10.1016/j.dsr.2015.08.011.

Porter, M.B., 1997: Twersky Scatter Theory. Accessed 10 February 2016. [Available online at http://oalib.hlsresearch.com/Modes/AcousticsToolbox/manual_html/node23.html.]

Porter, M.B., Heat, Light and Sound Research, Inc, 2011: The Bellhop Manual and User's Guide: Preliminary Draft. Accessed 15 December 2015 [Available online at http://oalib.hlsresearch.com/Rays/HLS-2010-1.pdf.]

Rudels, B., E.P. Jones, U. Schauer, and P. Eriksson, 2004: Atlantic sources of the Arctic Ocean surface and halocline waters, *Polar Res.*, 23(2), 181–208, doi: 10.1111/j.1751-8369.2004.tb00007.x.

Rudels, B., 2012: Arctic Ocean circulation and variability – advection and external forcing encounter constraints and local processes. *Ocean Sci.*, **8,** 261–286, doi: doi:10.5194/os-8-261-2012.

SCICEX Science Advisory Committee, 2010: SCICEX Phase II Science Plan, Part I: Technical Guidance for Planning Science Accommodation Missions. U.S. Arctic Research Commission, Arlington, VA, [Available online at https://nsidc.org/scicex/pdf/scicex_plan_phaseII.pdf.]

Schanze, J.J., 2012: The production of temperature and salinity variance and covariance: implications for mixing, WHOI. Accessed 30 April 2016 [Available online at https://dspace.mit.edu/handle/1721.1/79294.]

Seidov, D., J. I. Antonov, K. M. Arzayus, O. K. Baranova, M. Biddle, T. P. Boyer, D. R. Johnson, A. V. Mishonov, C. Paver and M. M. Zweng, 2014, Oceanography north of 60°N from World Ocean Database, *Prog. Oceanogr.,* **132,** 153–173, doi: 10.1016/j.pocean.2014.02.003.

Shimada, K., M. Itoh, S. Nishino, and A. Proshutinksky, 2005: Halocline structure in the Canada Basin of the Arctic Ocean. *Geophys. Res. Lett*., **32**, 1–5, doi:10.1029/2004GL021358.

Shimada, K., T. Kamoshida, M. Itoh, S. Nishino, E. Carmack, F. McLaughlin, S. Simmermann, and A. Proshutinsky, 2006: Pacific Ocean inflow: Influence on catastrophic reduction of sea ice cover in the Arctic Ocean, *Geophys. Res. Lett*., **33**, 1–4, doi:10.1029/2005GL025624.

Stroeve, J.C., V. Kattsov, A. Barrett, M. Serreze, T. Pavlova, M. Holland, and W.N. Meier, 2012: Trends in Arctic sea ice extent from CIMP5, CIMP3 and observations, *Geophys. Res. Lett*., **39**, 1–7, doi:10.1029/2012GL052676.

SUBFOR, 2016: Arctic Submarine Laboratory, Accessed 26 Apr 2016. [Available online at http://www.public.navy.mil/subfor/uwdc/asl/Pages/Timeline.aspx.]

Talley, L.D., G.L. Pickard, W.J. Emery, J.H. Swift, 2011: *Descriptive Physical Oceanography: An introduction.* Elsevier Ltd, 555pp.

Timmermans, M. L., j. Toole, R. Krishfield, and P. Winsor, 2008: Ice-Tethered Profiler observations of the double-diffusive staircase in the Canada Basin thermocline, *J. Geophys. Res. Oceans*, **113**, 1–10, doi: 0148–0227/08/2008JC004829.

Toole, J. M., R. A. Krishfield, M.-L. Timmermans and A. Proshutinsky, 2011: The ice-tethered profiler: Argo of the Arctic, *Oceanography*, **24**(3), 126–135, doi:10.5670/oceanog.2011.64.

Turner, J. and S. Pendlebury, 2004: *The International Antarctic Weather Forecasting Handbook.* British Antarctic Survey, 663pp

U.S. Department of Justice, 2015: Mid- and low-frequency sonar. Accessed 01 May 2016. [Available online https://www.justice.gov/enrd/mid-and-low-frequency-sonar.]

UIUC, Polar Research Group, 2016: The Cryosphere Today. Accessed 26 Apr 2016 [Available online http://igloo.atmos.uiuc.edu/cgi-bin/test/print.sh].

Wadhams, P., N. Toberg, 2012: Changing characteristics of arctic pressure ridges. *Polar Sci.*, **6,** 71–77, doi:10.1016/j.polar.212.03.002.

Walsh, J.E., 2013: Melting ice: What is happening to Arctic sea ice, and what does it mean for us? *Oceanography* **26(2),** 171–181, doi.:10.5670/oceanog.2013.19.

Whitworth, T., III, and A. H. Orsi (2006), Antarctic Bottom Water production and export by tides in the Ross Sea, *Geophys. Res. Lett.*, **33,** L12609, doi:10.1029/2006GL026357.

Worcester, P.F., B.D. Cornuelle, M.A. Dzieciuch, 2015: Canada Basin Acoustic Propagation Experiment (CANAPE). Scripps Institution of Oceanography. [Available online at https://scripps.ucsd.edu/research/proposals/canada-basin-acoustic-propagation-experiment-canape.]

Worcester, P.F., 2015b: Canada Basin Acoustic Propagation Experiment (CANAPE). Scripps Institution of Oceanography. Award Number: N00014-15-1-2068 [Available online at http://www.onr.navy.mil/reports/FY15/oaworche.pdf.]

WHOI, 2007: Submarines under Ice (1950s-1960s). Accessed 10 February 2016. [Available online at http://www.whoi.edu/page.do?pid=66624.]

WHOI, 2016: Ice-Tethered Profiler: An autonomous instrument for sustained observation of the Arctic Ocean. Accessed on 10 February 2016. [Available online at http://www.whoi.edu/page.do?pid=23096.]

INITIAL DISTRIBUTION LIST

1. Defense Technical Information Center
   Ft. Belvoir, Virginia

2. Dudley Knox Library
   Naval Postgraduate School
   Monterey, California